



Andrea Morbioli

**Analysis and development of
nonlinear Finite Elements for
modelling steel structures at
ambient and elevated temperature**

UNIVERSITY OF TRENTO - Italy
Department of Civil, Environmental
and Mechanical Engineering



Doctoral School in Civil, Environmental and Mechanical Engineering
Topic 1. Civil and Environmental Engineering - XXIX cycle 2014/2016

Doctoral Thesis - June 2017

Andrea Morbioli

**Analysis and development of nonlinear Finite Elements
for modelling steel structures at ambient
and elevated temperature**

Supervisors

Dr. Nicola Tondini, University of Trento, Italy
Prof. Jean-Marc Battini, KTH - Royal Institute of
Technology, Stockholm, Sweden



Except where otherwise noted, contents on this book are licensed under a Creative
Common Attribution - Non Commercial - No Derivatives
4.0 International License

University of Trento
Doctoral School in Civil, Environmental and Mechanical Engineering
<http://web.unitn.it/en/dricam>
Via Mesiano 77, I-38123 Trento
Tel. +39 0461 282670 / 2611 - *dicamphd@unitn.it*

University of Trento
Department of Civil, Environmental and Mechanical Engineering

Cycle: XXIX

Final Examination 29/06/2017

Board of Examiners:

Prof. Oreste Salvatore Bursi (University of Trento)

Prof. Massimiliano Fraldi (University of Naples Federico II)

Prof. Emidio Nigro (University of Naples Federico II)

Dedication

To my family

Acknowledgements

My deepest gratitude goes first and foremost to my supervisor Nicola Tondini for his constant encouragement and guidance. He has walked me through this experience assuring the maximum support and availability.

I would like to express my gratitude to Prof. Jean-Marc Battini, who helped me during my study at KTH (Royal Institute of Technology of Stockholm). He provided, without parsimony, his time, knowledges and suggestions to support me in the implementation of the thermomechanical finite element.

I also want to thank the University of Trento and the research group of Prof. Oreste S. Bursi for the Ph.D fellowship.

Finally a special thanks to all my colleagues along the way (Giuseppe Abbiati, Angela Beltempo, Enrico Cazzador, Rocco Di Filippo, Manuel Fassin, Vincenzo La Salandra, Luca Possidente and many others).

Contents

Summary: motivations and aims of the thesis work	p.1
TOPIC 1: Numerical analysis of flexural capacity of cold formed steel profiles subjected to monotonic bending moment	
1. Introduction	p.5
1.1 Relevance of experimental-numerical studies on cold formed steel profile: state of the art	p.5
2 Case study: experimental programme	p.6
3 Numerical modelling of cold formed profiles	p.10
3.1 Material characterization of the specimen: effect of cold forming process	p.10
3.2 Evaluation of residual stresses, related impact in cold formed steel structural behaviour and their inclusion into the numerical model	p.13
3.3 Introduction of geometrical imperfections and their influence in the numerical model	p.14
3.4 Description of the numerical model	p.16
4 Numerical outputs	p.18
4.1 Parametric analyses	p.21
References	p.23

Enclosure: PAPER 1 Cross-sectional flexural capacity of cold-formed laterally-restrained steel rectangular hollow flange beams. pp.25-54

TOPIC 2: Coupling methodologies between a CFD and an FE software for the analysis of structures at high temperatures.

1 Introduction	p.55
2 CFD and FE software	p.56
2.1 Fire Dynamics Simulator (Mc Grattan et al., NIST)	p.57
2.2 SAFIR (J-M. Franssen, University of Liege)	p.57

3. Definition of different levels of coupling	p.58
3.1. Weak coupling approach	p.59
4. Weak coupling CFD-FE approach: practical description of the procedure	p.60
5 Behaviour of real steel-concrete open car park subjected to localized fires	p.63
6. Case study: a steel-concrete open car park, CFD-FE weak coupling	p.65
References	p.71

Enclosure: PAPER 2 An integrated modelling strategy between a CFD and an FE software: methodology and application. pp. 73-96

TOPIC 3: Development of a co-rotational beam element for the study of steel structures subjected to fire loadings.

1 Introduction	p.97
2 Co-rotational beam element	p.98
3 Finite element model implementation of co-rotational beam theory	p.100
4 Thermomechanical behavior of carbon steel at high temperature	p.103
5 Integration of material constitutive law	p.106
6 Optimization of convergence procedure based on different displacement predictor	p.111
7 Path following techniques, branch-switching procedure applied to instability problems of steel structures subjected to fire	p.112
References	p.115

Enclosure: PAPER 3 A co-rotational two dimensional beam element for the analysis of elastic-plastic instability of steel structures subjected to fire. pp.117-160

Conclusions	p.161
Future research	p.163

List of Figures

Topic 1:

- Fig. 1** Cold formed profiles for structural applications; a) Building frame realized with cold formed profiles, b) Z cold formed elements used as purlins elements in roof system p.6
- Fig. 2** Geometry of the cross-section; a) RHFB 300, b) RHFB 240 p.7
- Fig. 3** Lateral and side view of the experimental set-up p.8
- Fig. 4** Instrumentation set-up of RHFB beams; a) RHFB 300, b) RHFB 240 p.9
- Fig. 5** Experimental test; a) Side view of the set up, b) Detail of web stiffener with end plate support p.9
- Fig.6** Example of a tensile test stress-strain relationship; a) RHFB 300 material data for tube flat and tube corner zone, b) RHFB 240 material data for tube flat and tube corner zone p.11
- Fig.7** Von Mises criterion; a) Von Mises yield surface in principal stress space ,b) Isotropic hardening (with reference to a uniaxial tensile test for the Von Mises yield surface in the deviatoric plane p.12
- Fig.8** Beam tested specimens; a) View of the specimen cross section, b) Bending caused by flexural residual stresses released after coupon extraction p.14
- Fig.9** Buckling shape referred to the lowest eigenmode p.15
- Fig.10** Introduction of geometry imperfections in the 3D model p.16
- Fig.11** Finite element model of the beam, RHFB 240 specimen p.17
- Fig.12** Shell 181 Ansys element p.17
- Fig.13** Detail of mesh discretization, local refinement, and end support constraint p.18
- Fig.14** Bending moment – displacement curves; a) RHFB 300, b) RHFB 240 p.19
- Fig.15** Plastic mechanism for the superior compressed flange, first evidence; a) Experimental test, b) Numerical output p.20
- Fig.16** Plastic mechanism for the superior compressed flange, second evidence; a) Experimental test, b) Numerical output p.20
- Fig.17** Web buckling RHFB300; a) Experimental test, b) Numerical output p.21
- Fig.18** Plasticization on the superior flange for RHFB240 profiles; a) Experimental test, b) Numerical output p.21
- Fig.19** Parametric analysis a) RHFB300 b) RHFB240 p.23

Topic 2:

- Fig.1** Full coupling approach between the three steps involved in the fire analysis p.58
- Fig.2** Weak coupling approach between the three steps involved in the fire analysis p.60
- Fig.3** Integration of the radiant intensities necessary to compute the impinging flux on structural elements; a) Radiant intensities incoming on a hemisphere (The number of radiant intensities is purely representative), b) Necessity of a spherical interpolation due to different surfaces orientation p.61
- Fig.4** Determination of the angle of visibility for an IPE profile p.63
- Fig.5** Experimental fire test on a real scale steel-concrete composite car park realized in France; a) View of the overall geometry, b) Plan view p.63
- Fig.6** Experimental outputs a) Measured temperature of gases b) Temperature

registered in the secondary steel beams	p.64
Fig.7 Experimental outputs; a) Position of the detection points for the measure of displacement, b) Vertical displacement of selected beam points	p.65
Fig.8 Analysed fire scenario; a) Position of cars for the reference fire scenario involving three cars, b) Rate of heat release as a function of time by three cars in the reference fire scenario	p.66
Fig.9 Numerical modelling; a) FE element model of the car park in SAFIR, b) FDS model of the compartment without the inclusion of superior beams c) FDS model of the compartment with the inclusion of superior beams.	p.67
Fig.10 Cross section temperature distribution under a localized fire Hasemi model, measured at collapse (27 min.); a) HEB220 column steel profile b) IPE400 secondary beam steel profile	p.68
Fig.11 Structural numerical response of the structure under a Hasemi localized fire model; a) Position of structural points in which the displacement is detected b) Vertical displacements of reference points (top column and secondary beam midspan)	p.68
Fig.12 Cross section temperature distribution measured at collapse (27 min.); a) HEB220 column steel profile, b) IPE400 secondary beam steel profile	p.69
Fig.13 Structural numerical response of the structure under CFD-FE weak coupling approach; a) Position of structural point in which the displacement is detected, b) Vertical displacement of reference point by assuming the FDS model with or without superior beams and comparison with correspondent Hasemi model	p.70

Topic 3:

Fig.1 Beam Kinematic	p.100
Fig.2 Steel properties under the effect of temperature as predicted by models and experimental tests;	
a) Thermal conductivity, b) Specific heat	p.103
Fig.3 Steel properties under the effect of temperature as predicted by models and experimental tests;	
a) Yield strength, b) Elastic modulus	p.104
Fig.4 Eurocode 3 stress-strain constitutive law for carbon steel at high temperature	p.105
Fig.5 Thermal strain: comparison between available models and experimental data outcomes	p.106
Fig. 6 Integration of material uniaxial constitutive law at high temperature	p.108
Fig. 7 Finite element validation against experimental test: steel portal frame subjected to an ISO 834 fire curve; a) Geometry and data of the case study, b) Comparison of displacements as function of element temperature	p.109
Fig. 8 Example of finite element validation against numerical predictions of SAFIR software; a) Geometry and data of the case study, b) Comparison between the two models on the vertical displacement of loaded node	p.110
Fig. 9 Scheme of the proposed displacement predictor	p.111
Fig. 10 Difference between the finite element model of a compressed column to be introduced in a commercial finite element code and via branch-switching procedure	p.112

List of Tables

Topic 1:

Table 1	Nominal section dimensions of the specimens. Dimensions in mm	p.7
Table 2	Measured section dimensions of the specimens. Dimensions in mm	p.7
Table 3	Flexural behaviour comparison between numerical and experimental results	p.18

Topic 2:

Not present

Topic 3:

Table 1	Solution scheme, co-rotational finite element	p.102
Table 2	Modifications introduced in the solution scheme by branch-switching procedure	p.114

**Summary:
Motivations and aims of the thesis work**

This thesis work aims to successively analyze and develop "ex novo" problems concerning the use of finite elements for the analysis of issues characterized by high plasticity, geometrical and material nonlinearity, large displacements and rotations; all combined with the effect of temperature on the material mechanical properties. The ultimate objective of the work is the analysis and development of nonlinear Finite Elements devoted to the modelling of steel structures at ambient and elevated temperature.

Three different experiences will be analyzed in this elaborate; each of them characterised by specific issues that may be involved in the analysis via finite element method of steel structures at ambient and elevated temperature. At the same time innovative aspects that are related, for example, to the particular typology of the analyzed case study (first case) or in the methodology used in the treatment of the problem (second and third case) are investigated. The thesis structure chronologically retraces this path and the results and the experience gained from each of them were exploited to ultimately implement a thermomechanical finite element that is expression of all the tackled problems. The thesis consists of a collection of three papers that have been published or submitted on each of the investigated topics.

In detail:

- In the first paper, a commercial finite-element code, of the type "multipurpose", such as ANSYS has been used for the analysis of innovative cold-formed, laterally-restrained steel rectangular hollow flange beams subjected to monotonic bending test. The numerical analysis has been carried out by means of the direct comparison with experimental tests on real scale specimens; that has allowed the detection of some phenomenological problems that have been included in the model calibration. From a numerical point of view, this work has at first allowed to deeply investigate the plastic problem by means, for example, the appropriate identification of the constitutive laws for the material, the correct choice of hardening law and yield surface, and their impact on the model. The local buckling problem typical of these profiles has been evaluated, through the use of shell elements. Furthermore, the effect of the global and local imperfections, which have been introduced in the model with different amplitudes, has been deeply investigated by evaluating their effect on the ultimate load. The calibration of the model finally allowed to perform a series of parametric analyses in order to extend the results to an extended range of profiles, characterized by different slenderness.

- In the second paper, the thermal problem has been introduced with the support of a finite element software, designed specifically for thermomechanical analysis (SAFIR). The case study is, in this case, based on a multi-storey steel-concrete composite open car park subjected to localized fire of vehicles. With this study, not only the plastic problem has been analyzed but also phenomena such as the effect of high geometrical

nonlinearity and large displacements on the structure in addition to the temperature effect on materials mechanical properties. The case study has been used to evaluate the assumptions and the issues that arise when developing an innovative integrated modelling methodology between a computational fluid dynamics (CFD) software applied to compartment fires and a finite element (FE) software applied to structural systems. Particular emphasis has been given to the weak coupling approach developed between the CFD code fire dynamics simulator (FDS) and the FE software SAFIR.

- In the third and last paper all the experiences obtained from the previous works have been focused on the implementation, inside the MATLAB environment, of a thermomechanical beam finite element based on the co-rotational beam theory for the analysis of two-dimensional frames heated under high temperature and subjected to plastic deformation and to the effect of geometrical nonlinearity. The finite element is mainly aimed at the study of steel structures, with double-symmetrical profiles such as IPE or HE cross sections, and could then be used as a modelling tool for typical frames subjected to thermal actions. The element implements both Euler-Bernoulli and Timoshenko beam theories and can analyse slender to moderately stocky structures. A co-rotational formulation was used for describing the beam kinematic. The degradation of the steel mechanical properties at high temperature according to the Eurocode 1993-1-2 was considered by integrating the material constitutive law based on a predetermined temperature field in the cross section. An improved displacement predictor for estimating the displacement field at the beginning of each time step was successfully implemented and allowed to significantly decrease the computational time. Furthermore, advanced path-following methods that detect secondary equilibrium paths owing to instability occurrence were implemented in order to analyse the elastic-plastic post-buckling behaviour of compressed steel elements at high temperature without the need of introducing geometrical imperfections. In order to show the potential of the developed finite element by highlighting the practical implications, a parametric analysis was performed to show whether the element could reproduce the EN1993-1-2 buckling curve. Validation against experimental and numerical data obtained with commercial software like ABAQUS and SAFIR is thoroughly shown in the paper.

TOPIC 1: Numerical analysis of cold formed steel profiles subjected to monotonic bending moment

1 Introduction

This section focuses on the development of a numerical work aimed at predicting the section bending moment capacity of cold-formed steel rectangular hollow flange beams (RHFBs). The geometry of RHFB comprises two torsionally stiff rectangular tube flanges connected by a slender web through welding. The numerical model is based on the results obtained from an experimental test programme reported in [1].

The following paragraphs describe the issues and assumptions that were considered to numerically capture the behavior of these specimens by introducing the fundamental phenomena that are involved in the modeling process of thin-walled steel beams.

The focus is the achievement of a calibrated finite element numerical model, able to predict the behavior of RHFB beams also characterized by different slenderness or plate thickness compared to those tested during the experimental campaign.

This is therefore recommended to preliminarily evaluate the effective resistance, under the particular load configuration, of such beams and consequently assess their convenience in term of performance and costs.

1.1 Relevance of experimental-numerical studies on cold formed steel profile: state of the art

In last decades, cold formed profiles for the realization of small houses frame used as secondary elements for roof systems have widen their market in Europe. However this typology of structural elements were already largely diffused and employed in North America and Australia. This impulse, registered also in Europe area is in part connected to the recent construction sector crisis that have consequently moved the attention towards the choice of alternative elements that are characterized by reduced weight and cost, in particularly if compared to common hot rolled steel profiles. This fact has attracted the interest of researchers towards the analysis of the structural behavior of such profiles both under static [2,3] and cyclic loadings [4,5] by taking into account the fundamental problem of instability that mainly derives by employing cross sections which generally fall into the Eurocode 3 Class 4.



(a)

(b)

Fig. 1 Cold formed profiles for structural applications; a) Building frame realized with cold formed profiles [6], b) Z cold formed elements used as purlins elements in roof system [7]

Moreover, thin walled cold formed profiles subjected to flexure may be sensitive to local, distortional and lateral torsional buckling that can reduce the bending capacities below the elastic moment M_y . This prevents the possibility to develop the inelastic reserve of the cross section. As a consequence sudden failure mechanisms may be observed even though the material has not even reached the elastic limit.

Several experimental tests were performed in last years by researchers in order to analyse these issues. Test results are compared with the outcomes deriving from finite element models that are used to numerically simulate the real physical behaviour.

On these premises, the present work aims to investigate the performance of a new I-shape cold formed profile, realized by means of two rectangular hollow flange cross sections connected by a slender web. A numerical model was then calibrated on the basis of the experimental evidences. The study analyses in particular the inelastic flexural behaviour of cold formed beams by avoiding lateral or torsional buckling. The tested beams were in fact conceived for the use as secondary beam elements in roof systems or slab of small steel-framed buildings where lateral displacements are generally prevented by the steel sheeting.

2 Case study: experimental programme

The research has involved six, I - shape, beam specimens fabricated with cold-formed rectangular hollow flange sections (see Fig. 2). The tested specimens can be divided into two typologies (RHFB-240 and RHFB-300) that differ in terms of global section size and plate thickness (see Table1). The actual measures carried out on tested specimens are instead used in the numerical model (see Table 2).

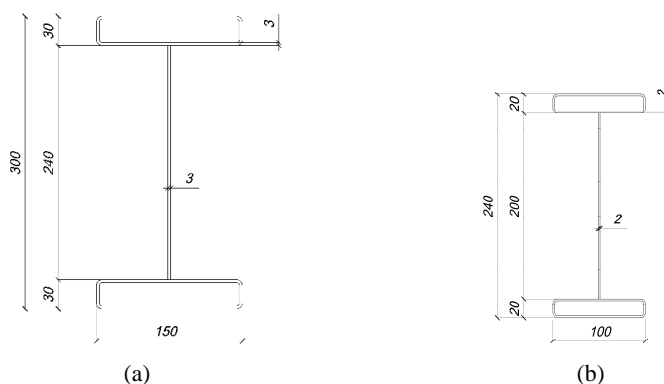


Fig. 2 Geometry of the cross-section; a) RHF300, b) RHF240.

The specimens were provided by *Gruppo Manni* an Italian steelwork company. Steel profiles were built by welding two structural tubes - produced by cold rolling - to a cut flat plate that constitutes the web. This fact prevented to introduce an intermediate stiffener on the outermost flat elements that are part of the tubes. This sort of detailing would be beneficial in order to reduce local buckling and crushing due to local effects of the flange in compression. Moreover, the way of producing the specimens was cause of higher imperfections with respect to those presumably expected if an appropriate cut machine had been used.

Table 1 Nominal section dimensions of the specimens. Dimensions in mm.

	h_{nom}	b_{nom}	$c_{t,nom}$	t_{nom}	L
RHF300	300	150	30	3.0	4500
RHF240	240	100	20	2.0	4500

Table 2 Measured section dimensions of the specimens. Dimensions in mm.

	h	b	c_t	t	r_i	L
T01 RHF240	235.2	100.0	19.8	1.92	1.75	4495
T02 RHF240	235.6	99.4	19.8	2.01	1.75	4495
T03 RHF240	235.6	100.0	20.0	2.00	2.25	4495
T04 RHF240	235.3	99.9	19.7	2.01	2.50	4495
T05 RHF300	298.3	150.0	30.4	2.87	3.00	4498
T06 RHF300	296.8	150.1	30.0	2.86	3.50	4496
T07 RHF300	297.5	150.1	30.2	2.93	3.50	4498

The experimental set-up for static tests – Fig. 3 - was conceived in order to force a failure mode caused by the attainment of the maximum bending moment capacity. Thus, each specimen was loaded according to a four-point bending scheme and was fully laterally restrained by two HE300B profiles that assured restraint against lateral torsional buckling, as illustrated in Fig. 3. Low-friction sheets were inserted between the specimen and the HE300B and they were arranged in such a way that they were not

in contact with the specimen. Moreover, transverse stiffeners were welded at supports and at load points to avoid either web buckling or web crushing or web crippling owing to concentrated transverse loads, as depicted in Fig. 3.

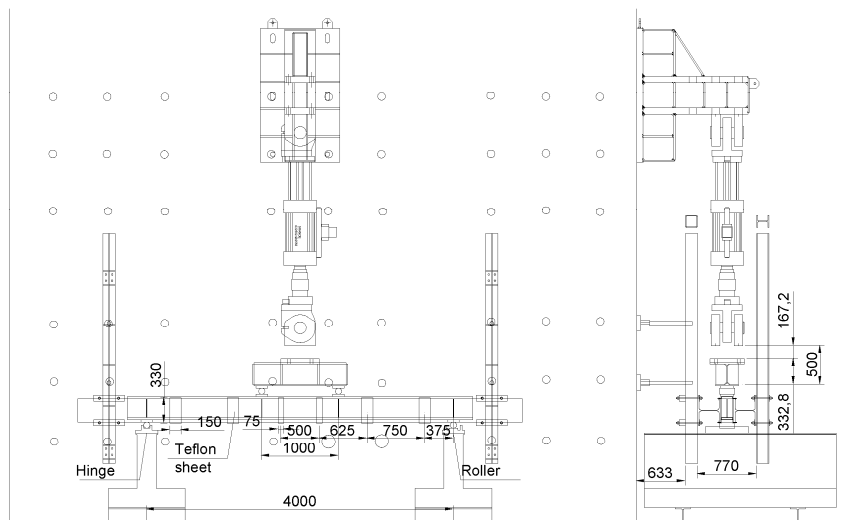
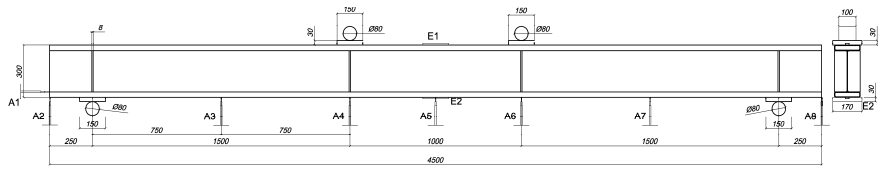


Fig. 3 Lateral and side view of the experimental set-up

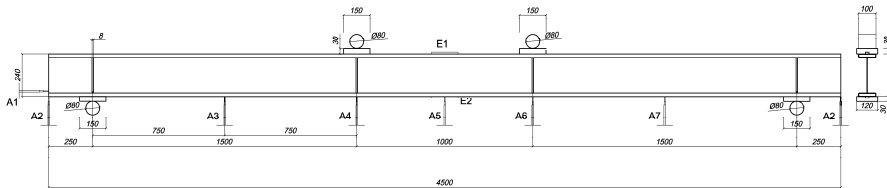
As previously mentioned, the load was applied by means of a four-point bending scheme in order to induce in the central span, i.e. the length between the two load application points, constant bending moment and zero shear force. In this way, the midspan load condition of a simply supported beam could be well reproduced. The load was introduced by means of a hydraulic actuator that was displacement-controlled at a speed of 0.5 mm/min.

The total length of the specimens and the distance between the two point loads were selected on the basis of the recommendations provided in Appendix A.3.4 of EN1993-1-3 (2006). As a result, the total length was 4.5 m, the span between supports 4 m and the distance between point loads 1 m. The end supports consisted of a hinge and a roller, respectively.

The instrumentation (Fig. 4) comprised vertical displacement transducers (A2-A8) installed along the specimen in order to measure the deflection; an horizontal transducer (A1) at the roller support in order to measure the horizontal movement and of strain gauges (E1 and E2) glued on the top and on the bottom flange of the midspan section in order to record strains.



(a)



(b)

Fig. 4 Instrumentation set-up of RHFB beams; a) RHFB 300, b) RHFB 240



(a)



(b)

Fig. 5 Experimental test; a) Side view of the set-up, b) Detail of web stiffener with end plate support

3 Numerical modelling of cold formed profiles

In next paragraphs the main issues and assumptions that were involved in the study of cold formed profiles will be introduced and analysed. The aim is to develop a numerical model able to predict experimental outcomes and consequently take into account the main physical phenomena that are involved in the examination of flexural resistance of rectangular hollow flange beams. The numerical calibrated finite element model could then be used in order to perform parametric analyses.

Numerical studies on cold formed profiles are already available in literature. Anapayan and Mahendran [2] analysed for example the lateral buckling behaviour of C shape hollow flange beams, Shifferaw and Schafer [3] introduced numerical models for predicting the inelastic bending capacity of back to back C or Z sections subjected to 4 point bending tests; Avery et al. [8] numerically studied the flexural capacity of hollow triangular flange beam developed and designed in Australia for use as a flexural member. Other studies could be reported for different profiles shape or load conditions [9, 10], however not redundant analyses are until now available for similar designed rectangular hollow flange beams. This work aimed to expand the knowledge of flexural resistance also to this innovative cold formed steel profile.

3.1 Material characterization of the specimen: effect of cold forming process

Carbon steel presents a stress-strain curve that is usually characterized by a linear elastic range followed by a yield plateau. In many cases the material is modelled by means of a bi-linear curve.

Other metals, such titanium, aluminium and stainless steel have nonlinear stress-strain curves featuring relative low proportionality stresses and extensive strain-hardening ranges [11]. In these cases a particular criterion for defining the yield limit must be specified. For stainless steel, for example, the equivalent yield stress is determined on the base of the permanent strain of the 0.2% proof stress.

Moreover in the case of cold formed profiles, realized with carbon steel or stainless steel, the working process due to cold rolling modifies the classical stress-strain relation by introducing a significant strength enhancements in the corner regions due to hardening. Indeed for flat regions in particular near corners area the elastic-plastic transition is smoother.

The definition of the representative stress-strain curve, also with reference to the specific position of the material in the cross section, is therefore of particular importance to define with a sufficient order of accuracy the structural behaviour in particular when buckling phenomena are involved.

Some authors as Engesser [12,13] or Shanley [14] analysed the effect of yielding on the buckling resistance in particular of compressed columns by underlying substantial differences when a load deflection curve is plotted with reference to a bilinear or a non-linear stress-strain curve. In the case of cold formed beams, such as the ones analysed in this study, a correct characterization of the material properties is fundamental in order

to correctly capture the generation of local buckling effects in the compressed elements of the specimen. A campaign of tensile tests on different material specimens were then carried out in order to obtain sufficient data to successively numerically reproduce the experimental evidences. The study involved 25 specimens extracted from different region of the flange tubes (corner, lateral border and superior flat zone) and web. The obtained stress-strain relations are then reported in Fig.6.

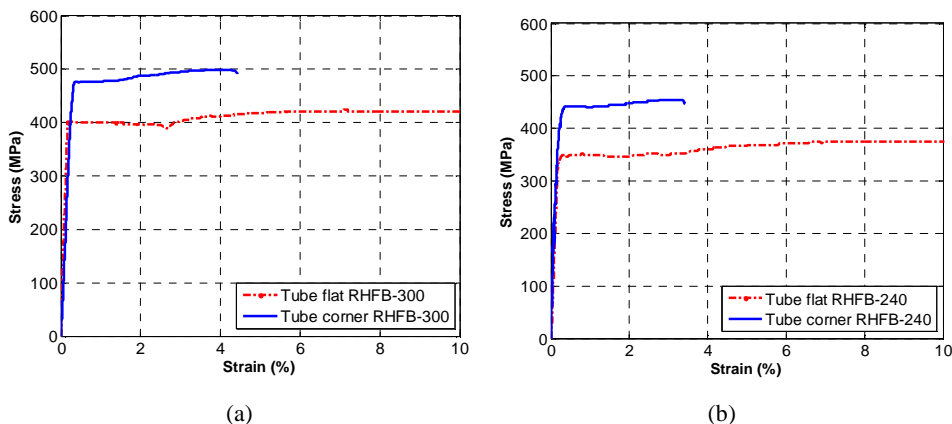


Fig.6 Example of a tensile test stress-strain relationship; a) RHF300 material data for tube flat and tube corner zone, b) RHF240 material data for tube flat and tube corner zone

The tensile tests revealed that a significant increase in yield strength, due to cold forming process, was actually observed in the corner zone respect to the flat part of the tube flange. The percentage of increase, obtained from an average measure performed on all tested specimens, was around +28% for RHF240 beams and +30% for RHF300 profiles.

The results of the investigation on material characterization were then employed in the numerical finite element model.

True stress – strain relationships were employed for material properties because more representative of the state of material in large strain analyses.

$$\sigma_t = \sigma_e (1 + \varepsilon_e) \quad (1)$$

$$\varepsilon_t = \ln(1 + \varepsilon_e) \quad (2)$$

The Poisson's ratio was taken equal to 0.30. The Multilinear Isotropic Hardening (MISO) material law, available in ANSYS [15], was instead used for implementing the true stress – strain data. It allows including a user-defined stress-strain relationship by means of several linear segments. The material model relies on the Von Mises criterion, a classical yield criteria introduced in 1913 based on the second deviatoric stress invariant J_2 . The physical idea of the criterion is that: “*the plastic yielding begins when the J_2 stress deviator invariant reaches a critical value*”. The critical value mainly

depends on a hardening internal variable that is intrinsically connected with the density of dislocations in the crystallographic microstructure that causes an isotropic increase in resistance to plastic flow [16]. In some cases (i.e. isotropic hardening), the internal variable could be easily expressed by means of a singular scalar value whose amplitude determines the size of the yield surface. In the case of the Von Mises criterion the yield surface could be defined as:

$$f_{\sigma} = \sqrt{3J_2} - \sigma_y \quad (3)$$

where σ_y is the uniaxial yield stress.

In the space of principal stresses the yield surface associated with the Von Mises criterion is represented by the surface of an infinite cylinder (see Fig.7a); whose axis coincides with the hydrostatic axis. In the biaxial stress space it is an ellipse symmetric with respect to the origin of the principal stress plane (Fig.7b).

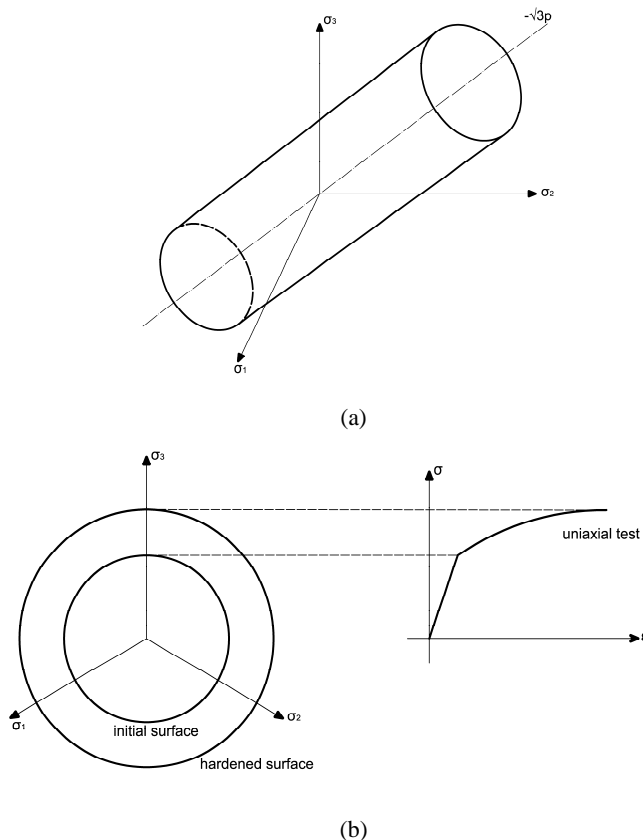


Fig.7 Von Mises criterion; a) Von Mises yield surface in principal stress space, b) Isotropic hardening (with reference to a uniaxial tensile test for the Von Mises yield surface in the deviatoric plane)

It is important to note that the pressure component of the stress tensor is not included in the definition on the Von Mises criterion, as a consequence the yielding is influenced only by J_2 .

For that reason the criterion could be used to describe the elastic-plastic behavior of material in which the failure is due to slip between dislocation planes (ductile metals), however is not suitable for describing concrete-based material, for which the effect of hydrostatic component should be taken into account.

In the MISO model, based on isotropic hardening, the yield function exhibits a uniform expansion of the initial yield surface without translation; this choice was deemed adequate for the purpose because of the monotonic nature of the experimental tests.

3.2 Evaluation of residual stresses, related impact in cold formed steel structural behaviour and their inclusion into the numerical model

Cold formed profiles undergoes forming and fabrication processes that could produce high values of residual stresses with a consequent impact on the structural behaviour of steel elements. Residual stresses are caused by plastic deformation or temperature gradients induced in the metal and due to rolling, welding, grinding, heat treating etc. In relation with their magnitude and position they could produce negative effects on fracture, fatigue, brittle fracture and buckling phenomena [17]. The knowledge of residual stresses, and their introduction in the numerical model, is necessary in order to correctly model the flexural behaviour of the beams and to take into account the buckling phenomena that could affect the compressed parts.

However, due to practical difficulties, the measurement of residual stresses in cold-formed sections is not easy, in particular for rounded parts of the cross section where their impact is greater. For flat parts of the cross section, their derivation is easier but the relative amplitude is in this case negligible. In addition, there is an almost lack of data or analytical models able to predict the residual stresses distribution in conventional cold-formed profile. Some studies were performed by Rondal [18] however the developed model was for example not able to describe the variation of the stresses through the thickness, this conduces to essential simplifications. As a consequence, a reasonable and justifiable introduction of these quantities, performed for example at the level of shell thickness integration points, is not so expected. A possible way consists in their implicit inclusion in the stress-strain diagram obtained through tensile tests that characterize the material properties. Before going into the details, we have to point out that for cold-formed members the residual stresses could be computed as the sum of two terms: membrane residual stresses and a flexural component.

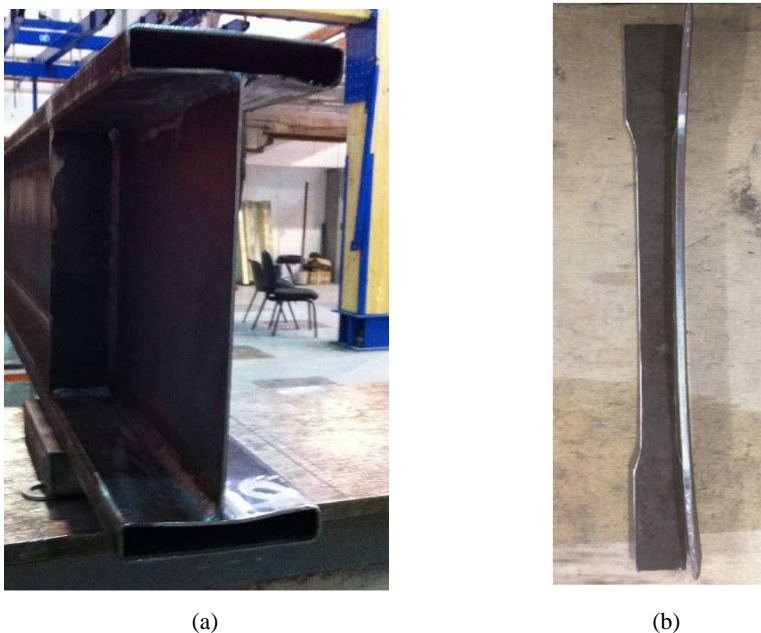


Fig.8 Beam tested specimens; a) View of the specimen cross section, b) Bending caused by flexural residual stresses released after coupon extraction

The stress-strain relationship obtained from tensile tests includes flexural residual stresses whose magnitude is not negligible for cold-formed sections [19]. The proof of residual stresses presence was also observed after coupon extraction by observing the bending of material specimens due to the release of flexural residual stresses (Fig. 8b). Conversely, membrane residual stresses were not measured because small with respect to flexural residual stresses, apart from corner regions. These zones are also affected by the increase in yield stress due to cold forming work process.

The cold working enhancement was not included in the corner zones because the membrane residual stresses were not modelled: in fact, they tend to counteract one another.

On the other hand if the increase in yield strength has been included in the model, residual stresses have to be explicitly introduced. The followed methodology applied to the specific case study has effectively demonstrated a dependence of the ultimate bending moment M_u on residual stresses. Generally the introduction of residual stresses, both flexural and membrane, reduces the value of M_u by causing premature buckling phenomena of the compressed part.

3.3 Introduction of geometrical imperfections and their influence in the numerical model

Geometrical imperfections were introduced into the numerical model in order to take into account the lack of correspondence between the ideal geometry (defined by the

nominal values reported in Table 2) and the real configuration of the profile. Their introduction was indeed of fundamental importance in particular for this case study, where a high level of imperfections were observed on all tested beams. As previously mentioned the presence of high imperfections on specimens was mainly connected to the working process employed for their fabrication and the absence of a specific cut machine.

Two problems should be taken into account when a geometrical imperfection has to be introduced into a numerical model. The first relies on the determination of the imperfection shape, the second regards the correspondence amplitude. With reference to the second point, the present study follows the methodology introduced by Schafer and Pekoz [19] that quantify the maximum amplitude imperfection d as a function of the element width w :

$$d = 0.006w \quad (4)$$

The shape of the imperfection was instead determined by means of a linear buckling analysis referred to the eigenvector associated to the lowest eigenvalue Fig.9.

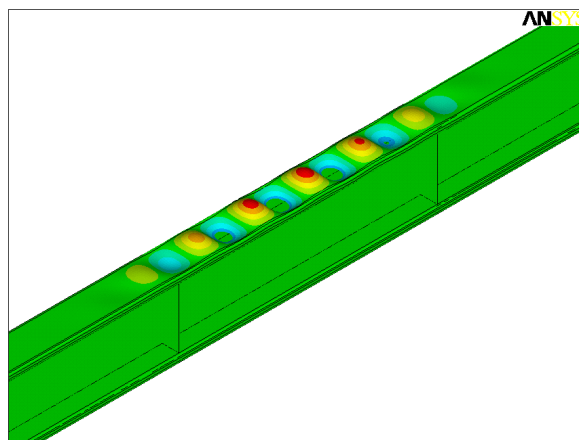


Fig.9 Buckling shape referred to the lowest eigenmode

In the present model specific imperfections, obtained by following the reported procedure, were introduced for the web and top compressed flange.

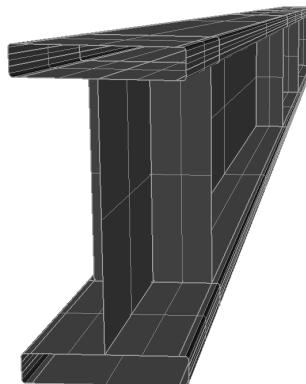


Fig.10 Introduction of geometry imperfections in the 3D model

Different value of amplitude were tested; finally the maximum value proposed by Schafer and Pekoz [19] was maintained in order to calibrate experimental data. Performed finite element simulations demonstrates a direct connection between the imperfection amplitude and the ultimate bending moment M_u (an increment of amplitude progressively reduces the value of M_u and vice versa). The introduction of geometrical imperfections also modify the failure mechanism that instead would be observed in the presence of an ideal structure.

3.4 Description of the numerical model

Numerical nonlinear models provide a comprehensive means to investigate cross-section slenderness, plastic material reserve, activation of local buckling phenomena and other effects that influence the bending strength of beams.

All the beams tested during the experimental campaign T01, T02, T03 – (RHFB240), and T04 T05, T06 - (RHFB300) were modelled through finite element analysis. Shell elements were introduced for the study of the specimens.

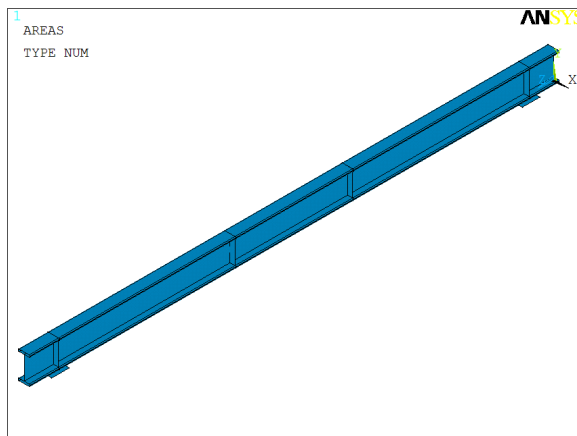


Fig.11 Finite element model of the beam. RHFB 240

More in detail, the SHELL 181 element (Fig.12), available in the ANSYS elements library [15], was used in order to model all the part of the beam. The element is suitable for analyzing thin to moderately-thick shell structures. It is a four-node element with six degrees of freedom at each node: translations in the x, y, and z directions, and rotations about the x, y, and z-axes [15]. SHELL 181 includes the linear effects of transverse shear deformation.

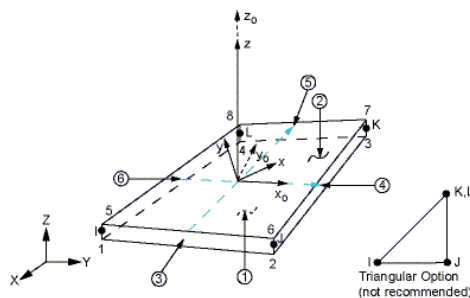


Fig.12 Shell 181, Ansys element [15]

A mesh sensitivity investigation was initially performed in order to introduce an adequate model refinement able to accurately predict the spread of plasticity and arise of local buckling effects. Finally a uniform mesh, constituted by means of square shape elements, 5mm wide, was introduced for all the simulations. All the parts of the beam, included the intermediate web stiffeners and the end plates supports, were modelled into ANSYS. Restraints were applied, accordingly to the static scheme, to the end plates along an ideal line (Fig. 13) in order to distribute the reaction forces.

The plate and the bottom tube flange were connected together by means of rigid

constraint equations CERIG command [15]. Load was applied by introducing an increasing displacement ramp to all nodes belonging to the intermediate web stiffeners, located at half meter from the midspan. Lateral constraints were then introduced in order to prevent the lateral torsional buckling and simulate the constraint effect of the lateral HE300B profiles.

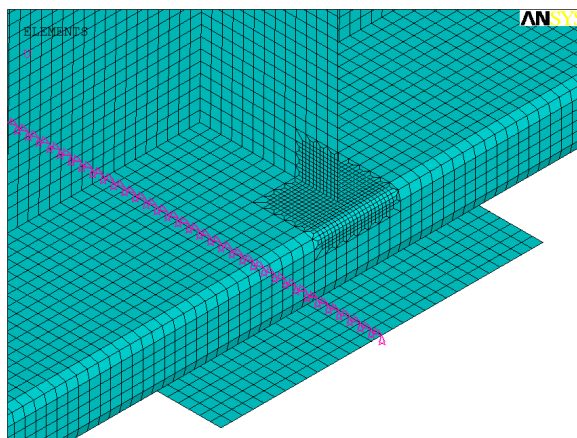


Fig.13 Detail of mesh discretization, local refinement, and end support constraint

4 Numerical outputs

The accuracy of the final element model was checked by comparing the ultimate moment capacity M_u and the vertical displacement δ_u at midspan in correspondence of M_u .

Results are reported in Table 3.

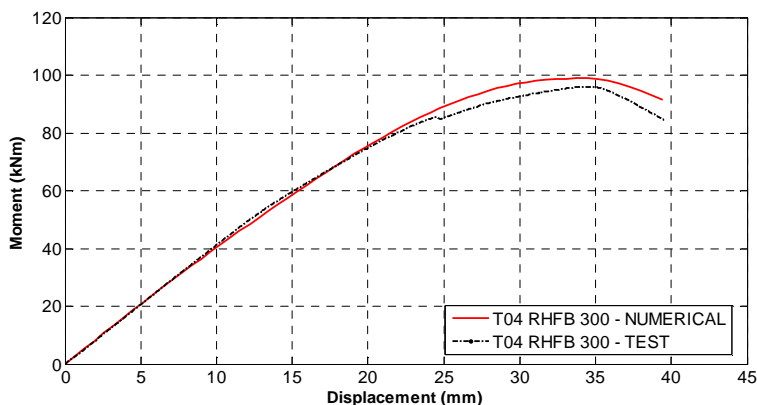
Table 3 Flexural behaviour comparison between numerical and experimental results.

	$M_{u,FE} / M_{u,TEST}$	$\delta_{u,FE} / \delta_{u,TEST}$
T01 RHFB-240	1.02	0.90
T02 RHFB-240	1.05	0.93
T03 RHFB-240	1.04	0.93
T04 RHFB-300	1.03	0.98
T05 RHFB-300	0.98	0.81
T06 RHFB-300	1.04	0.95
Average	1.03	0.92
COV	0.02	0.06

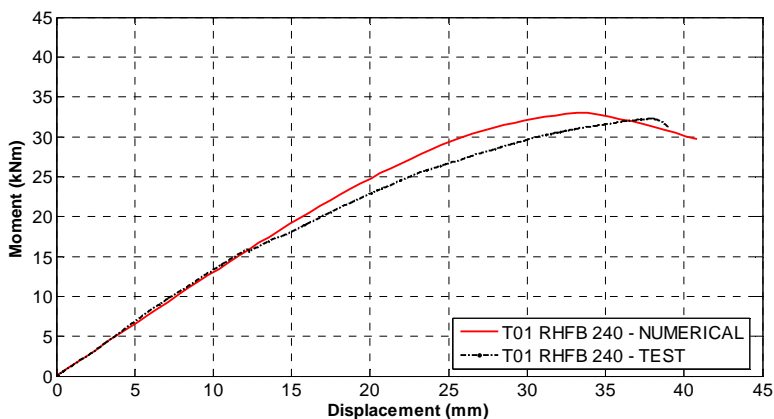
The finite element model generally tends to overestimate the ultimate moment capacity M_u of the tested beams that demonstrate to be more deformable (mainly for the effect of high imperfections). Nevertheless the difference, as shown in Table 3 is limited (average ratio $M_{u,FE} / M_{u,TEST} = 1.03$); the developed model is a good predictor of

the ultimate moment capacity of the profiles.

The bending-moment displacement curves for two specimens (T01 RHFB 240) and (T04 RHFB 300) are showed in Fig. 14. In the figures the results of the numerical simulation are superimposed to the experimental evidences.



(a)



(b)

Fig.14 Bending moment – displacement curves; a) RHFB 300, b) RHFB 240

The validation of the numerical model takes into account also the comparison of the failure mode that was observed experimentally with the equivalent mechanism detected by means of the finite element simulation.

The plastic mechanism that involved the top compression flange of the tested specimen

is depicted in Fig. 15a and Fig. 16a, while Fig. 15b and Fig.16b show the correspondence numerical output. The finite element model demonstrates to well capture the arise of buckling phenomena that affects the superior flange. The web buckling observed for RHFB 300 specimens was also well represented in the numerical model Fig. 17. The finite element model of the RHFB 240 specimens was although not able to detect some minor plasticisation occurred early in the tests as depicted in Fig. 18. These profiles (RHFB 240 series) were in fact more affected by imperfections and local effects that increase their deformability with a deviation in the elastic branch as illustrated in Fig. 14b.

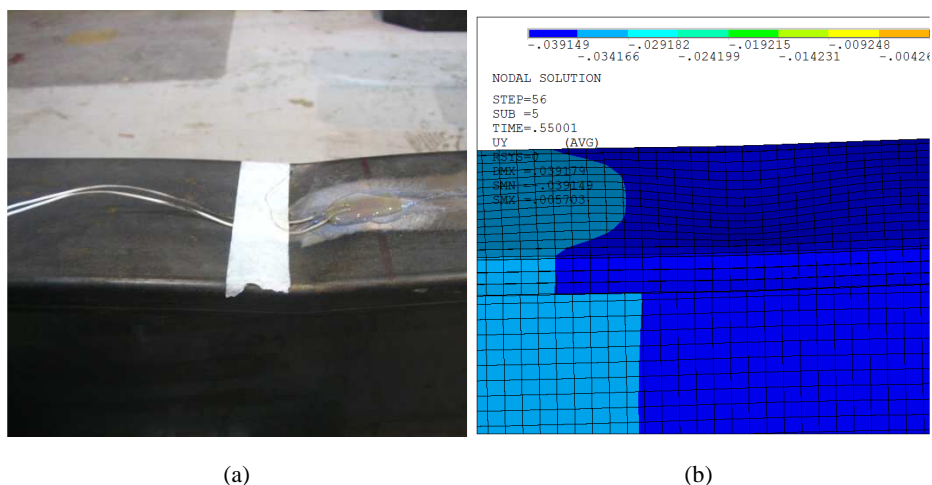


Fig.15 Plastic mechanism for the superior compressed flange, first evidence; a) Experimental test, b) Numerical output

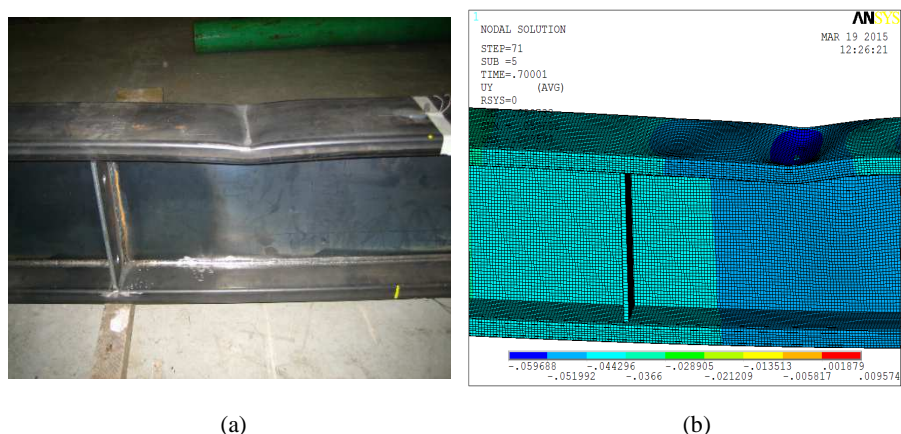


Fig.16 Plastic mechanism for the superior compressed flange, second evidence; a) Experimental test, b) Numerical output

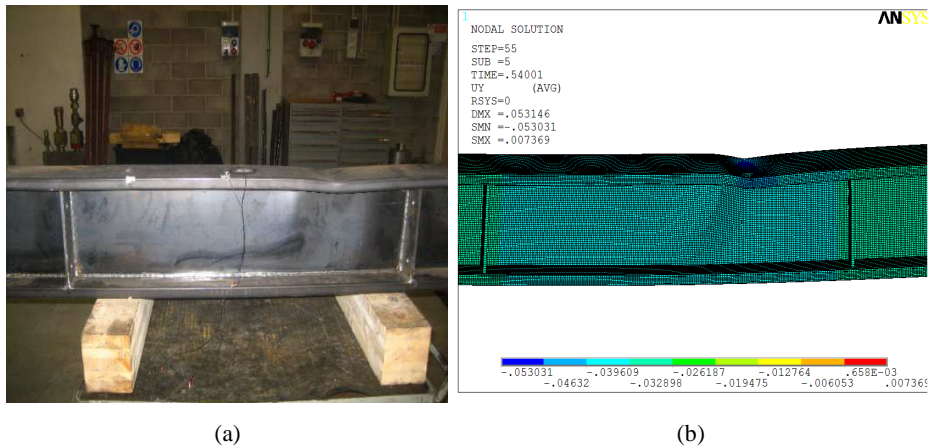


Fig.17 Web buckling RHF300; a) Experimental test, b) Numerical output

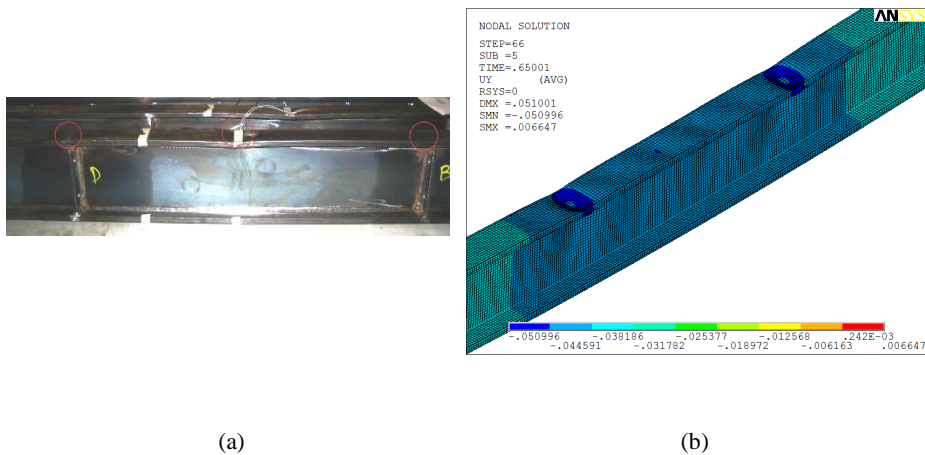


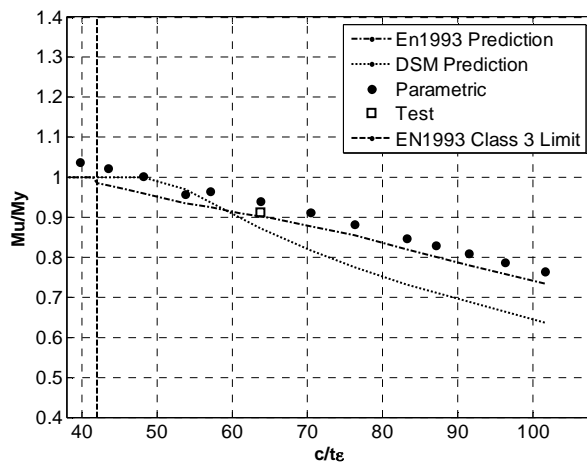
Fig.18 Plasticization on the superior flange for RHF240 profiles; a) Experimental test, b) Numerical output

4.1 Parametric analyses

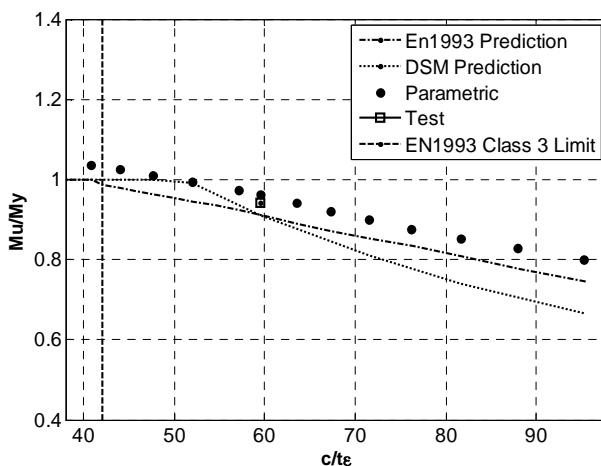
A series of parametric studies were performed in order to expand the available findings to a wider range of beam slenderness.

Material properties representative of material coupon tests that include flexural residual stresses were used in the parametric analyses. Local geometric imperfections were modelled by means of the lowest buckling mode shape. A 4-point bending scheme was used with span of the beams set to 4 m and a distance of 1 m between the point loads.

The dimensions of the cross section were the ones of the T01 RHFB-240 profile and the T04 RHFB-300 profile but the thickness that was varied between 1.2 mm and 4 mm for the RHFB-240 profile and between 1.8 mm and 5 mm for the RHFB-300 cross section, respectively. The limit of a Class 3 section according to the EN1993-1-1 [20] was assessed by plotting the normalised ultimate moment M_u over the elastic bending moment M_y with respect to the most limiting $c/t\epsilon$ slenderness value that was the tube flange in compression, where c is the flat width of the plate element, t its thickness and $\epsilon = \sqrt{(235/f_y)}$. As expected, the parametric study showed no considerable difference between the two cross sections owing to geometry similarity normalised with respect to the material strength. In fact, from Fig. 14a and Fig 14b it is possible to observe that trend line obtained through linear regression has same slope and intercept values. From the same Figures it is possible to note that EN1993 tends to be conservative by underestimating the flexural capacity of RHFB cross-sections. The Class 3 limit is also conservative: from the parametric analyses the onset of local buckling of the tube flange in compression, i.e. when $M_u/M_y < 1$, is observed for $c/t\epsilon$ equal to about 48 instead of 42. Furthermore, the capability of the DSM [21] of predicting the flexural behaviour of RHFBs was investigated. The main idea behind this method is the determination of all elastic instabilities, i.e. local M_{crf} , distortional M_{crd} , global buckling M_{cre} and the bending moment that causes yield, i.e. M_y . The smallest moment among M_{crf} , M_{crd} , M_{cre} and M_y identifies the bending resistance of the section. Since lateral-torsional buckling and lateral-distortional buckling do not apply to the case study, only local buckling is considered. It is worth to point out that for comparison purposes input data of finite strip analyses in terms of geometry of the cross section and mechanical properties, i.e. yield strength, elastic modulus and Poisson's coefficient, were chosen consistently with the FE analyses. The stress distribution was assumed according to the $M_{y,f}$. No imperfections were included and bending resistance beyond the elastic bending moment is not estimated. Thus, it is interesting to observe when local buckling becomes significant and affects the flexural strength of the beam by preventing the attainment of the elastic bending moment. Fig. 14a and Fig. 14b show that the DSM provides a good prediction for $c/t\epsilon$ slenderness value up to 55, then it tends to significantly underestimate the flexural strength ($c/t\epsilon > 60$).



(a)



(b)

Fig.19 Parametric analysis a) RHF300 b) RHF240

References

- [1] Tondini N., Morbioli A., *Cross-sectional flexural capacity of cold-formed laterally-restrained steel rectangular hollow flange beams*, *Thin-Walled Structures* (2015); 95: 196-207.
- [2] Anapayan T., Mahendran M., *Numerical modelling and design of LiteSteel Beams subject to lateral buckling*, *Thin-Walled Struct.* 50(2012):128–140.
- [3] Shifferaw Y., Schafer B.W., *Inelastic Bending Capacity of Cold-Formed Steel Members*, *Journal of Structural Engineering* (2012), 138(4):468-480.

-
- [4] Ono T., Suzuki T., *Inelastic behaviour and earthquake-resistance design method for thin-walled metal structures*, Proceedings of the IABSE Coll. on Thin-Walled metal structures in Building (1986), Stockholm, 115-122.
- [5] Della Corte G., Fiorino L., Landolfo R., *Seismic behaviour of sheathed cold formed structures: Numerical study*, J. Struct. Eng. (2006), 132(4): 558-569
- [6] <https://sfia.memberclicks.net/how-cold-formed-steel-is-made>
- [7] http://www.steel-rollformingmachine.com/china-cold_formed_steel_profile_cz_purlin_roll_forming_machine_ce_standard_380v_15kw-9297116.html
- [8] Avery P., Mahendran M., Nasir A., *Flexural capacity of hollow flange beams*, Journal of Constructional Steel Research (2000), 53: 201-223.
- [9] Xu L., Sultana P., Zhou X., *Flexural strength of cold-formed steel built-up box sections*, Thin-Walled Structures (2009); 47: 807-815.
- [10] Keerthan P., Hughes D., Mahendran M., *Experimental studies of hollow flange channel beams subject to combined bending and shear actions*, Thin-Walled Structures (2014), 77: 129-140.
- [11] Rasmussen K. J. R., *Coupled instabilities in thin-walled metal structures*, Notes for Phd Postgraduate course, 2014
- [12] Engesser F., *Zeitschrift fur Architektur und Ingenieurwesen*, 1889. 35: p. 455.
- [13] Engesser F., *Schweizerische Bauzeitung* 1895; 26: p. 24.
- [14] Shanley F., *Inelastic Column Theory*. Journal of the Aeronautical Sciences (1947); 14(5): 261-267.
- [15] ANSYS, Documentation for ANSYS-release 14.0, Copyright SAS IP, Inc., 2011.
- [16] De Souza Neto EA, Peric D., Owen DRJ, *Computational Methods for plasticity, Theory and applications*, Wiley 2008
- [17] Rondal J., *Peculiar Problems in Cold-formed Steel Design Part 1 and Part 2, Light gauge metal structures recent advances*, Cism Courses and Lectures no.455-(2005), Springer.
- [18] Rondal J., *Residual Stresses in Cold rolled Profiles*, Construction and Building Materials (1987); 1(3): 150-164
- [19] Schafer B.W., Peköz T., *Computational modelling of cold-formed steel: characterizing geometric imperfections and residual stresses*, J.Construct.Steel Res. (1998); 47: 193–210.
- [20] European Committee for Standardisation, *Eurocode 3 Design of steel structures - Part 1-1. General rules and rules for buildings*
- [21] Schafer B.W, *Review: the direct strength method of cold-formed steel member design*, J. Construc. Steel. Res (2008); 64: 766-778

PAPER 1: Cross-sectional flexural capacity of cold-formed laterally-restrained steel rectangular hollow flange beams

The following paper was published in:

Thin-Walled Structures (ELSEVIER)

“Cross-sectional flexural capacity of cold-formed laterally-restrained steel rectangular hollow flange beams” Vol. 95 pp.196–207 (2015)

<http://dx.doi.org/10.1016/j.tws.2015.06.018>

Cross-sectional flexural capacity of cold-formed laterally-restrained steel rectangular hollow flange beams

Nicola Tondini^a and Andrea Morbioli^a

^aDepartment of Civil, Environmental and Mechanical Engineering, University of Trento, Via Mesiano 77, 38123, Italy

Corresponding author: *nicola.tondini@unitn.it; ph: +39 0461 281976

Keywords: cold-formed steel profiles; rectangular hollow flange beams; flexural capacity; experimental tests; numerical modelling.

Abstract

This paper presents the results of a comprehensive experimental-numerical study aimed at determining the flexural performance of cold-formed laterally-restrained steel rectangular hollow flange beams (RHFBS). Two RHFBS of different dimensions were considered as representative of typical secondary beams in small steel-framed houses. Results of the experimental study that consisted of i) material characterisation and ii) tests on full-scale specimens are thoroughly presented. Moreover, a numerical work was performed in order to develop a model able to reproduce the experimental outcomes and used to expand the available findings over a wider slenderness range through parametric studies.

1 INTRODUCTION

The use of cold-formed steel sections in small houses is well established in North America and Australia but in Europe their exploitation is mainly limited to secondary elements of steel roof systems. Nowadays, even in Europe the use of such profiles is growing fast. Cold-formed steel sections are very sensitive to buckling phenomena - both local and global - because they are generally thin-walled profiles so that they can easily undergo cold working processing. Therefore, a lot of research has been addressed to understand their behaviour under compressive stresses owing to axial and/or flexural loads, see for instance review articles on numerical and experimental findings [1-4]. Nevertheless, their use as secondary beams often entails fully laterally-restrained conditions of the flange in compression owing to a steel sheeting that prevents lateral torsional buckling (LTB). Hence, the knowledge of the bending moment capacity of the section represents a key information [5]. In order to enhance bending moment performance, the use of hollow flange sections is tempting because most of the mass is

located away from the strong section axis. Moreover, hollow flange sections also provide torsional stiffness. Thus, RHFBS can be a potential alternative to C- and Z-sections as well as to small hot-rolled sections thanks to: i) enhanced flexural behaviour associated with reduced weight; ii) ease of producing doubly symmetric geometry and iii) fast production times. Related research works were mainly devoted to the analysis of rectangular hollow flanges of channel sections [6-10] and to triangular hollow flanges of doubly symmetric I sections [11-13]. Numerical studies on symmetric rectangular hollow flange sections have been recently performed [14-18]. However, there is a lack of experimental testing on such profiles. On these premises, an experimental test programme on cold-formed steel RHFBS was planned in order to investigate their flexural performance by determining the section bending moment capacity. Furthermore, the experimental part is enriched by a numerical study with the following objectives: i) to calibrate a finite element model capable of reproducing the experimental evidences; ii) to perform a parametric analysis with the aim to broaden the results in terms of bending capacity to a wider range of slenderness ratios of the tube flanges; iii) to assess whether the prediction of the Eurocode EN1993 is adequate for such a cross section; iv) to evaluate how the Direct Strength Method (DSM) [2] estimates the flexural behaviour of RHFBS cross sections.

The paper is articulated as follows: Section 2 describes in detail the experimental programme and the geometry of the specimens; Section 3 provides insight into the characterisation of the material properties; Section 4 presents and discusses the outcomes of the tests on the full-scale specimens; Section 5 introduces the numerical modelling and analyses the results of the model calibration; Section 6 describes the parametric studies, whereas Section 7 draws the conclusions and future perspectives.

2 EXPERIMENTAL PROGRAMME

The whole experimental programme was performed at the Laboratory of Structures and Materials Testing of the University of Trento. In detail, it was characterised by:

- 25 tensile tests on flat strips and on round corners of material coupons extracted from the specimens. The objective was to measure the actual tensile properties and to estimate the hardening induced by the cold working processing;
- 6 static monotonic tests on RHFBS.

2.1 Specimen properties

The section dimensions of the specimens were selected to be of common use in structural applications such as either purlins or secondary beams in small steel-framed houses. In detail, the section geometry is depicted in Fig. 1. The nominal dimensions of the specimen sections are reported in Table 1. Both sections were overall classified as Class 4 according to EN1993-1-1 [19] considering an S235 steel grade: tube plates of Class 4 and web plate of Class 3.

Gruppo Manni, an Italian steelwork company, was a stakeholder of this experimental

study, that can be considered as a feasibility study, and provided the specimens. However, since the machine for fabricating the RHFBS from a unique coil was not available yet, the specimens were built by welding two structural tubes - produced by cold rolling - to a cut flat plate that constitutes the web. This fact prevented to introduce an intermediate stiffener on the outermost flat elements that are part of the tubes, as illustrated in Fig. 1. This sort of detailing would be beneficial in order to reduce local buckling and crushing due to local effects of the flange in compression.

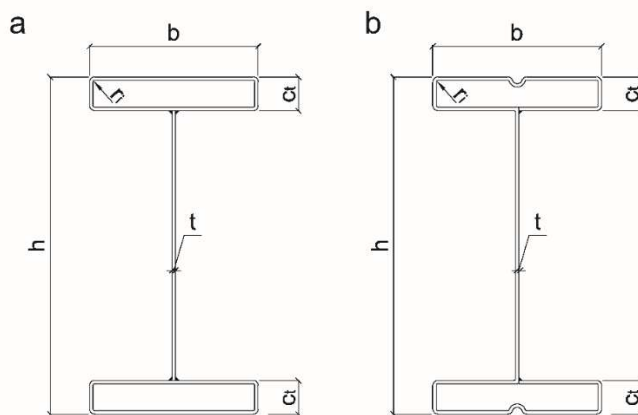


Fig. 1:Geometry of: (a) tested section and (b) optimised section.

Moreover, the way of producing the specimens was cause of higher imperfections relatively to those presumably expected if the appropriate cut machine had been used. In this respect, in agreement with the steelwork company, we convened to perform repeated tests – three for each section dimension – because some scatter in the results could appear. For instance, it was noticed increased imperfections owing to extensive welding between tubes and web plate and RHFBS-240 profiles, endowed with smaller elements and thicknesses, were more prone to be affected by the production process. This aspect was observed in the tests and confirmed during the numerical calibration process presented later on in the paper.

Based on the previous considerations, a careful measurement of the actual geometric properties of thin-walled profiles is important because even small deviations from the nominal values could significantly affect their local and global behaviour. As a result, Table 2 collects the actual measurements of the section dimensions as well as the actual length of the specimen L . As expected, the actual values differ from the nominal ones and they are generally lower. Global imperfections were also measured even though they could not influence the behaviour of the beams during the tests because any possible global buckling mode was prevented. In any case, for sake of completeness, for all the specimens the global imperfections in the two principal axes were measured and they were less than $L/2500$. Only for the T01 RHFBS-240 specimen a global

imperfection about the weak axis of approximately $L/1600$ was found. It was difficult to precisely quantify local initial imperfections and consequently, they were not measured. Nevertheless and as already observed, RHFB-240 profiles were overall more affected by imperfections.

Table 1. Nominal section dimensions of the specimens. Dimensions in mm.

	h_{nom}	b_{nom}	$c_{t,nom}$	t_{nom}	L_{nom}
RHFB-240	240	100	20	2.0	4500
RHFB-300	300	150	30	3.0	4500

Table 2. Measured section dimensions of the specimens. Dimensions in mm.

	h	b	c_t	t	r_i	L
T01 RHFB-240	235.2	100.0	19.8	1.92	1.75	4495
T02 RHFB-240	235.6	100.0	20.0	2.00	2.25	4495
T03 RHFB-240	235.3	99.9	19.7	2.01	2.50	4495
T04 RHFB-300	298.3	150.0	30.4	2.87	3.00	4498
T05 RHFB-300	296.8	150.1	30.0	2.86	3.50	4496
T06 RHFB-300	297.5	150.1	30.2	2.93	3.50	4498

3 MATERIAL CHARACTERISATION

A total of 25 tensile tests were carried out on material coupons extracted from the specimens. The tests were performed in accordance with EN ISO 6892-1 [20]. Both flats and corners were tested in order to establish the increase in yield strength owing to hardening induced by cold working and to obtain the stress-strain material relationships to be used in the numerical modelling. Corners were machined and tested to minimise eccentricities when loaded in the traction machine; in particular, the end parts were flattened. The yield strength f_y of steels used for structural applications classified according to EN10025-2 [21] is defined as the upper yield strength R_{eH} . Nevertheless, due to cold working, the corners undergo plastic deformation; thus, the yield point may not be well defined and the 0.2% proof stress ($R_{0.2p}$) is consequently provided. As highlighted in Table 3, a discrepancy among values of average yield strength between web and flange flats was observed, leading to so-called hybrid beams. This is particular evident for the RHFB-300 where the tube flat was characterised by significantly higher yield strength than the web.

Table 3. Tensile properties of steel.

	avg f_y (MPa)	COV	avg f_u (MPa)	COV	avg ϵ_f (%)	COV
RHFB-240						
Web	274.1	0.03	354.4	0.03	24.6	0.08
Tube flat	343.3	0.02	391.0	0.03	22.5	0.21
Tube corner	439.6	0.02	476.9	0.03	7.7	0.12
RHFB-300						
Web	258.5	0.01	355.6	0.00	25.6	0.09
Tube flat	394.8	0.02	438.1	0.02	25.8	0.16
Tube corner	512.2	0.06	551.8	0.07	10.6	0.06

The stress-strain relationships obtained from tensile tests included flexural residual stresses whose magnitude is significant in cold-formed sections [22]. In fact, when the material coupons were extracted from the specimens, bending caused by the release of flexural residual stresses was clearly observed, as shown in Fig. 2a.

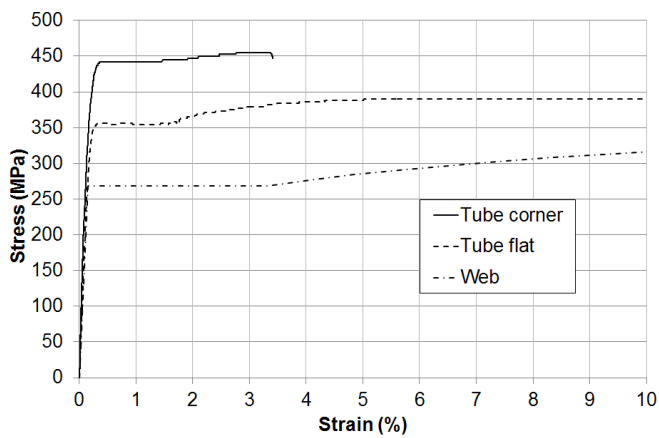
Then, once they were put into the traction machine by gripping the edges, flexural residual stresses were reintroduced through application of small loads. Conversely, membrane residual stresses were not measured because small with respect to flexural residual stresses, apart from corner regions [22].

The initial elastic modulus was found to be 202 GPa for the small tube, i.e. RHFB-240, and 203 GPa for the large tube, i.e. RHFB-300. Table 3 also reports on the average percentage elongation at failure ϵ_f based on an 80 mm gauge length.

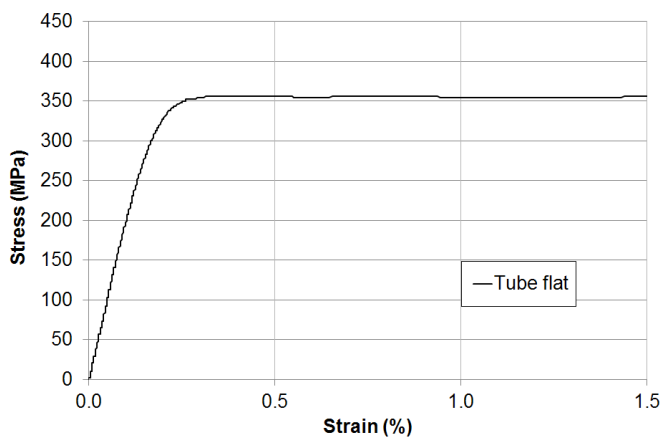


Fig. 2. (a) Curving of material coupon upon machining from the cross sections; and (b) testing machine.

Typical stress-strain relationships of the web, tube flats and tube corners are shown in Fig. 3a. The corner tests confirmed an increase in yield strength due to cold working. The stress-strain constitutive laws of the RHFB-240 tube flats did not exhibited a sharp transition between the elastic and the plastic range – see Fig. 3b -. This behaviour was less evident for the tubes of RHFB-300. In Fig. 3a it may be observed that elongation at failure does not attain values given in Table 3 because the extensometer had to be removed some instants before failure in order to avoid any damage, as it is possible observe in Fig. 2b.



(a)



(b)

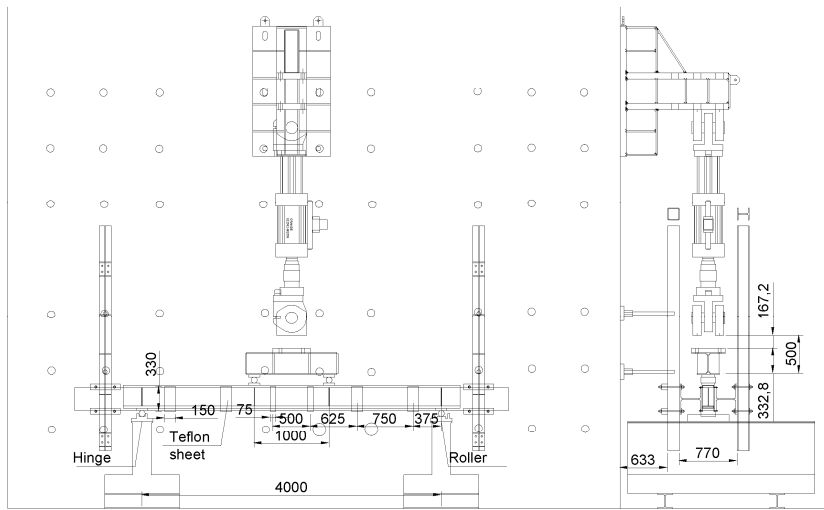
Fig. 3. RHFB-240. (a) Typical stress-strain relationship from tensile coupon tests; and (b) elastic-plastic transition of the tube flat.

4 STATIC TESTS

4.1 Experimental setup

The experimental setup for static tests – Fig. 4a - was conceived in order to induce a failure mode caused by the attainment of the maximum bending moment capacity of the section. Thus, each specimen was loaded according to a four-point bending scheme and was fully laterally-restrained by two HE300B profiles that assured restraint against LTB, as illustrated in Fig. 4b. Low-friction sheets were placed between the specimen and the HE300B and initially not in contact with the specimen. Had LTB occurred, they would have allowed the full cross-section bending tests to continue without affecting them thanks to the inherent small friction coefficient. However, LTB was not observed in any test. Moreover, transverse stiffeners were welded at supports and at load points in order to prevent either web buckling or web crushing or web crippling caused by concentrated transverse loads. The load was introduced by means of a hydraulic actuator that was displacement-controlled at a speed of 0.5 mm/min. The total length of the specimens and the distance between the two point loads were selected within the recommendation limits provided in Appendix A.3.4 of EN1993-1-3 [23]. In detail, the length of the specimen should be at least 15 times its greatest transversal dimension and point loads should be applied to the specimen to produce a length under uniform bending moment at midspan of at least $0.2 \times (\text{span})$ but not more than $0.33 \times (\text{span})$. Thus, the specimen length was 4.5 m, the span 4 m and the region of constant bending moment equal to 1 m. The end supports consisted of a hinge and a roller, respectively. In order to minimise local effects, load was applied through the web stiffeners, as depicted in Fig. 4c. In detail, the spreader rigid beam (see Fig. 4a) distributes the load to two metallic cylinders placed on the horizontal plates that are rested on the vertical lateral bracing plates visible in Fig. 4c.

The instrumentation applied to each specimen is shown in Fig. 5 and comprised: displacement transducers (A2-A8) installed along the specimen in order to measure the vertical deflection; a displacement transducer (A1) at the roller support in order to measure the horizontal movement and strain gauges (E1 and E2) glued on the top and on the bottom flange of the midspan section in order to record strains. The applied load was registered by the actuator load cell.



(a)



(b)



(c)

Fig. 4. a) Front and side views of the experimental setup. Dimensions in mm; b) T03 RHFB-240 setup; c) load application system through the web stiffeners.

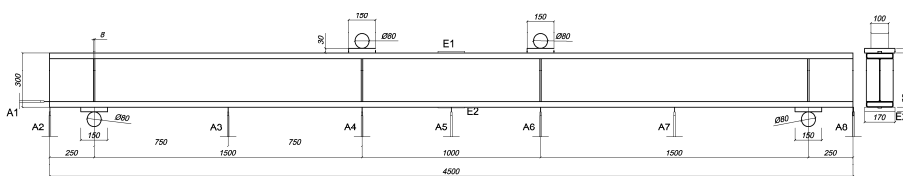


Fig. 5. Instrumentation setup. Dimension in mm.

4.2 Test results and discussion

For both sections, some similar features in terms of flexural behaviour were observed. In particular, during the tests the specimens experienced well distributed local buckling waves on the compression flange, see as an example Fig. 7a. This was expected because of the absence of an intermediate stiffener capable of increasing the critical buckling stress of the compression flange. Minor plasticization of the compression flange occurred early in the tests of RHFB-240 because more affected by imperfections introduced by the production process and more sensitive to local effects owing to small thicknesses. This led to a loss of stiffness early in the tests. Moreover, some minor plasticization was also observed outside the zone between the point loads owing to local imperfections associated with still significant bending moment close to the constant bending moment region, as illustrated in Fig. 6c-d and Fig. 7b. Nonetheless for each specimen, the eventual failure was caused by a formation of a main spatial plastic mechanism inside the zone of constant bending moment, as depicted in Fig. 6a-b and Fig. 7c-d. Particularly for RHFB-300, web buckling was also observed, as noticeable in Fig. 7d.

Results in terms of bending moment-vertical displacement curves are illustrated in Fig. 8 for RHFB-240 specimens and Fig. 9 for RHFB-300 specimens, respectively. The bending moment was computed by multiplying the half of the measured applied load by the distance between the bearing and the point load. As soon as the ultimate bending moment was reached, it suddenly decreased without exhibiting an appreciable plateau, which is typical of Class 4 sections as defined in EN1993-1-1 [19].

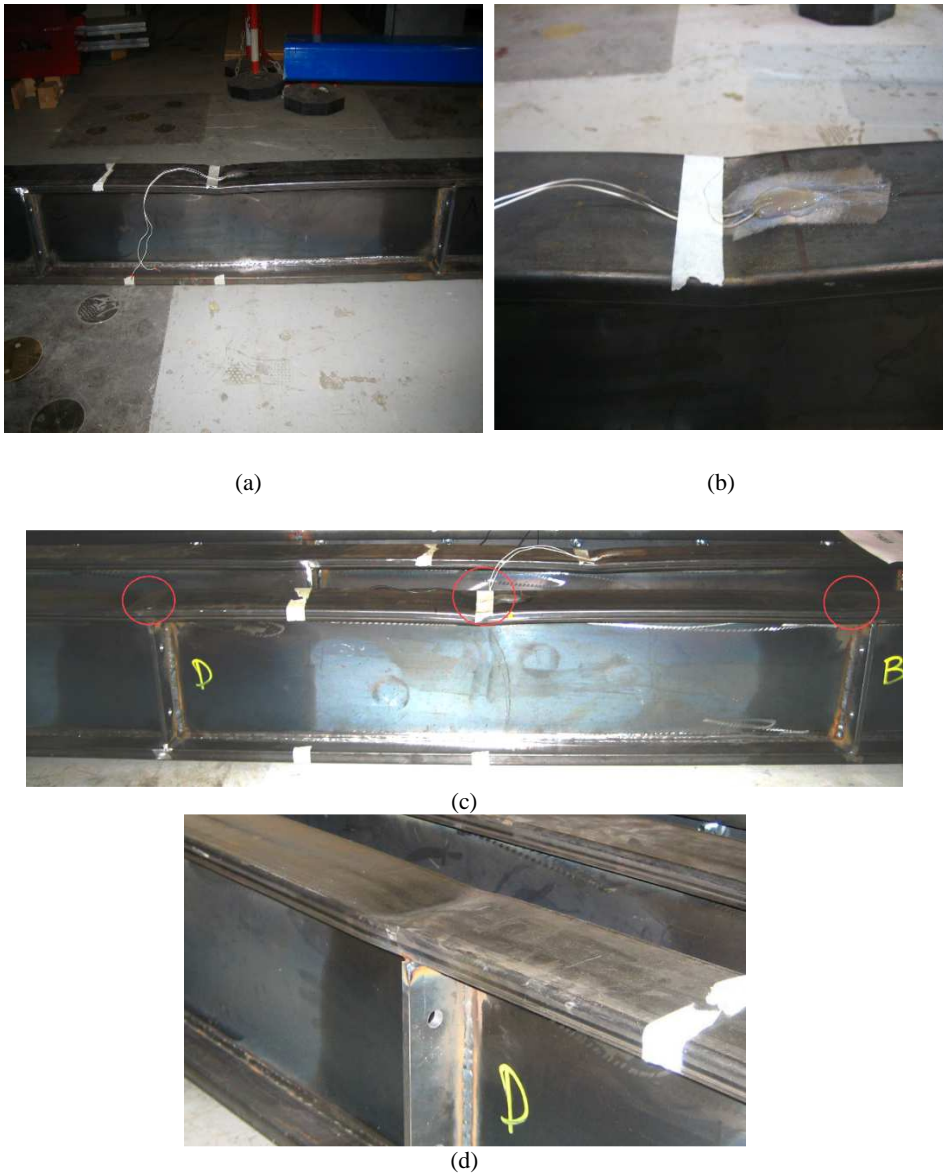
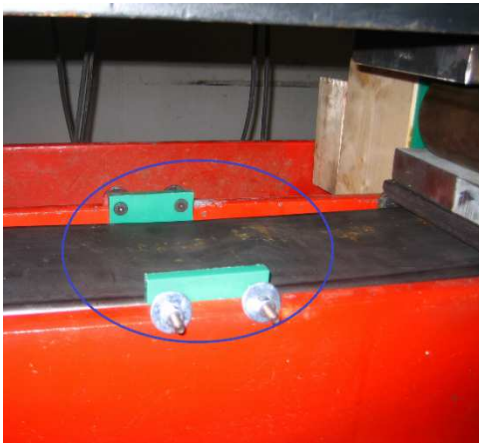


Fig. 6. RHFBS-240: a) T02 failure mode; b) T02 enlargement of the main plastic mechanism at failure; c) T03 minor plasticization outside the point loads (left), main plastic mechanism at failure (middle), minor plasticization between the point loads (right); d) enlargement of the plasticization outside the point loads.



(a)



(b)



(c)



(d)

Fig. 7. RHFB-300: a) T06 local buckling; b) T04 main spatial plastic mechanism; c) T04 highlight of the main spatial plastic mechanism (right) and of a secondary plastic mechanism (left); d) T06 failure mode with web buckling.

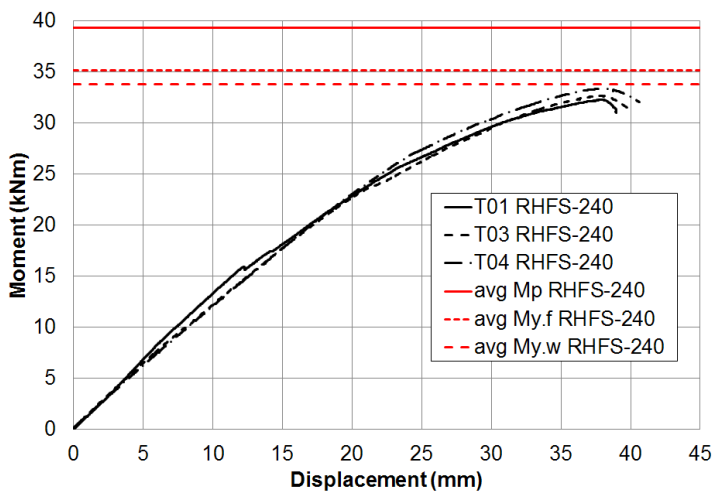


Fig. 8. RHFB-240: bending moment-displacement curves.

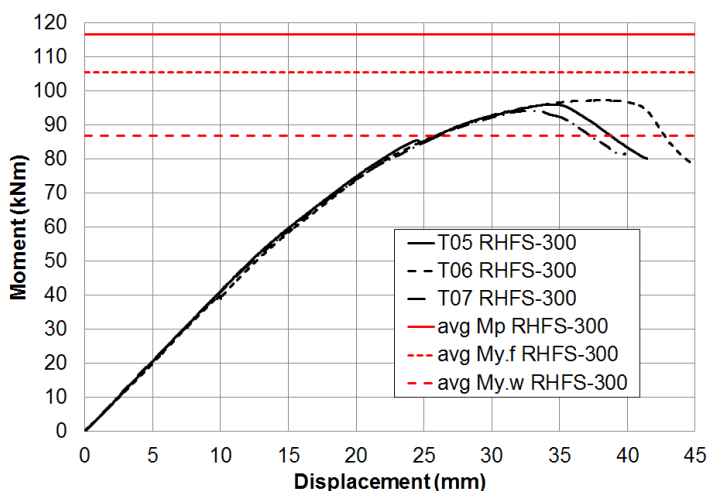


Fig. 9 RHFB-300: bending moment-displacement curves.

Moreover, in both Fig. 8 and Fig. 9 the average elastic moment M_y and the average plastic moment M_p of the specimens are shown. Both M_y and M_p were computed based on the actual geometric and mechanical properties. In this respect, the mechanical properties of tube flat coupons were used and no increase in yield strength in the tube corners was considered because membrane compressive residual stresses were not accounted for. In fact, as stated before, in cold-formed steel sections, compressive membrane residual stresses are small except for the corner regions where, owing to cold working, there is an increase in yield strength. Since these two effects tend to counteract one another [22] and the compressive membrane residual stresses were not measured, the elastic and the plastic bending moment were computed by disregarding the cold

working effect in the corners. This reasoning is consistent with the one employed in the numerical analyses presented in Section 5. M_y and M_p were calculated for each specimen and then averaged to obtain one single value for both section geometries, i.e. RHFB-240 and the RHFB-300, respectively. Such curves are useful for identifying which level of bending moment was achieved by the specimens. M_y was determined as the bending moment at which one fibre of the section attains first the elastic limit ($M_{y,w}$). Since the beams were of hybrid type because the tubes and the web were made of different steel grades with $f_{y,tube\flat} > f_{y,web}$, it occurred that the elastic limit was reached before in the web than in the outermost fibre of the tube plate, as schematized in Fig. 10. For this reason, and particularly for RHFB-300, the resulting elastic bending moment ($M_{y,w}$) does not exploit the flexural strength of the tube whose stress can be still well within the elastic range. Thus, in order to mobilise the full strength of the outermost fibre of the tube plate a partial plastic redistribution in the web has to be accepted, where its part in compression may be affected by local buckling phenomena. Thus, an additional estimate of the elastic bending moment ($M_{y,f}$) computed by the stress distribution shown in Fig. 10 was provided. It considers gross section stresses. All RHFB-240 collapsed before attaining the average elastic moment whichever the way to compute it; thus, confirming the typical flexural behaviour of a Class 4 section [19], as depicted in Fig. 8. For RHFB-300, it is interesting to note in Fig. 9 that if we consider the elastic bending moment by definition, i.e. $M_{y,w}$, the section flexural behaviour of the specimens may appear of Class 3. Nevertheless, at $M_{y,w}$, the tubes are in their elastic range with a significant reserve in flexural capacity before yielding that is not mobilised yet because $f_{y,tube\flat} \gg f_{y,web}$. In fact, if we now consider $M_{y,f}$, it may be observed that none of the specimens attained this level of bending moment hinting that local buckling affected the tube plate before achieving $f_{y,tube\flat}$ as well as the web after yielding. The latter comparison is more meaningful considering that in bending capacity tests the flanges are the main resisting elements, whereas the web mainly carries shear. In this specific case, about 90% of bending is carried by the tubes and about 10% by the web. Consequently, the section can be actually classified as Class 4. Moreover, such a behaviour was confirmed in the tests where local buckling of tube plate and of the web were clearly observed.

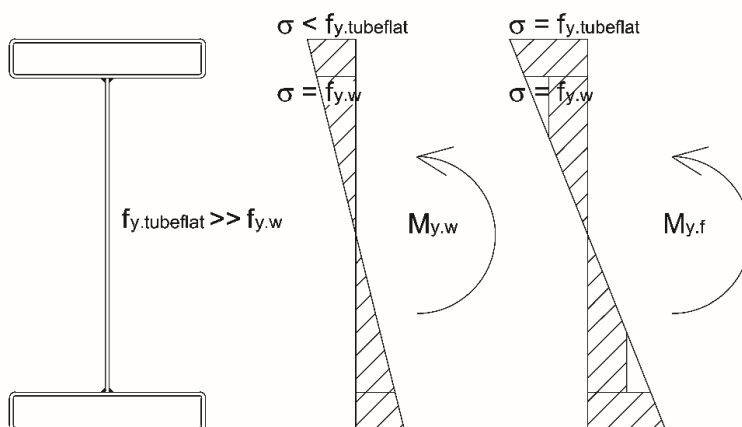


Fig. 10. Stress distribution assumed for computing the section elastic bending moment.

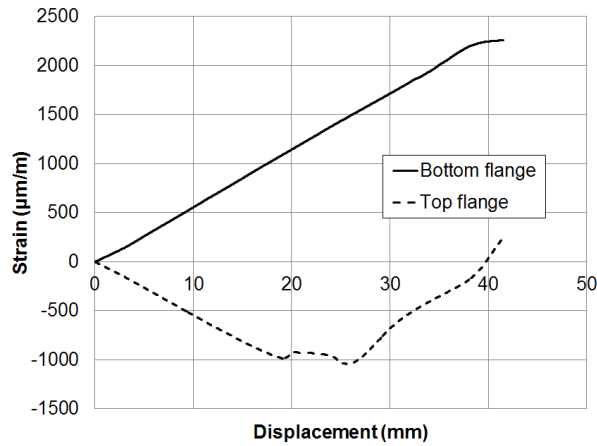
The results of the tests are summarised in Table 4 where the ultimate load (P_u), the ultimate bending moment (M_u), the vertical displacement at maximum load (δ_u) and the mass per unit length (g) of the specimens based on measured geometries are provided. The outcomes show that use of such profiles can be appealing in terms of the ratio flexural performance/weight in lieu of small hot rolled steel sections. In this respect, an estimate of weight savings is provided by determining through calculation the section modulus of IPE sections that would guarantee the average ultimate moment reached in tests by RHFBs considering the actual tube flat yield strengths: an IPE160A with mass per unit length equal to 12.7 kg/m, i.e. about +20% with respect to gRHFB-240, would be equivalent to the tested RHFB-240 section; and an IPE220 with $g = 26.2$ kg/m, i.e. about +25% with respect to gRHFB-300, is comparable to the tested RHFB-300 section.

Table 4. Flexural performance of RHFBs.

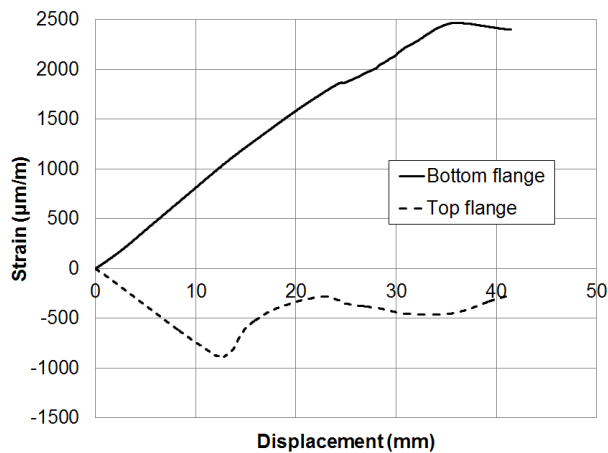
	P_u (kN)	M_u (kNm)	δ_u (mm)	g (kg/m)
T01 RHFB-240	43.0	32.3	37.6	10.0
T02 RHFB-240	43.6	32.7	37.7	10.4
T03 RHFB-240	44.5	33.4	37.8	10.4
T04 RHFB-300	128.0	96.0	34.2	21.2
T05 RHFB-300	129.7	97.3	37.9	21.0
T06 RHFB-300	125.6	94.2	32.7	21.6

Now, if we look at the strain gauge recordings as a function of the vertical displacement depicted in Fig. 11, it is possible to note that for both beam types the strain order of magnitude is the same. Moreover, since the strain gauges were glued at the midspan of the two outermost tube flanges - see Fig. 5 -, as soon as local elastic buckling initiated in the compression top flange the corresponding strain reading did not increase monotonically anymore and its evolution depends on how buckling developed locally.

This phenomenon occurred at essentially the same compressive strain level for both sections because one of the key parameters that govern plate elastic buckling, i.e. the local slenderness ratio of the tube flange - $b / t \approx 50$ -, is the same. Moreover, it is interesting to note that the theoretical elastic critical buckling strain $\epsilon_{cr.thr}$ of the tube outermost flange considering $k\sigma = 4$ is about equal to 1.45‰ [24]. A lower experimental value of strain at which plate buckling occurred, $\epsilon_{cr.exp}$, is consistent considering the presence of imperfections and residual stresses.



(a)



(b)

Fig. 11. a) T03 RHFB-240 strain-displacement curve; b) T04 RHFB-300 strain-displacement curve.

5 NUMERICAL MODELLING

The numerical model was developed to perform nonlinear analyses of the tests and was used to expand the available findings over a wider slenderness range through parametric studies. The multipurpose finite element software ANSYS [25] was employed. Model geometry, application of loads, boundary conditions and material properties were implemented to seek consistency with the real setup, actual dimensions of the specimens and mechanical properties of steel. All the assumptions and schematizations will be discussed in detail in Subsection 5.1-5.3.

5.1 Geometric model

All beams tested in the experimental campaign – T01, T02, T03, T04, T05 & T06 - were modelled through FE analysis. Shell elements were used in order to fully grasp all the main phenomena that govern the behaviour of the beam under bending, such as local buckling and plasticity diffusion [13]. The Shell 181 element of the ANSYS library [25] was used to model all the parts of the profile, i.e. the rectangular hollow flanges, the central web, the web stiffeners located at supports and at load points as well as the plates at supports, as shown in Fig. 12. The Shell 181 element is a four-node element with six degrees of freedom at each node. It is well suited for moderately thick elements and for large rotation and/or large strain nonlinear applications. It is shear flexible and uses a uniform reduced integration method [25].

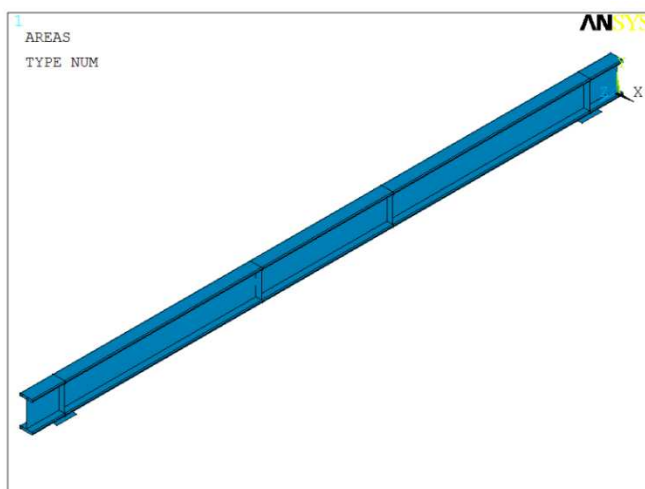


Fig. 12. FE model of the RHFB-240.

A uniform mesh discretization was implemented for all the components of the model using roughly square shape elements (aspect ratio close to one), the side dimension of which is about 5 mm wide. Mesh refinement was locally applied to zones of high concentration stresses, i.e. zone of supports and point loads, as highlighted in Fig. 13.

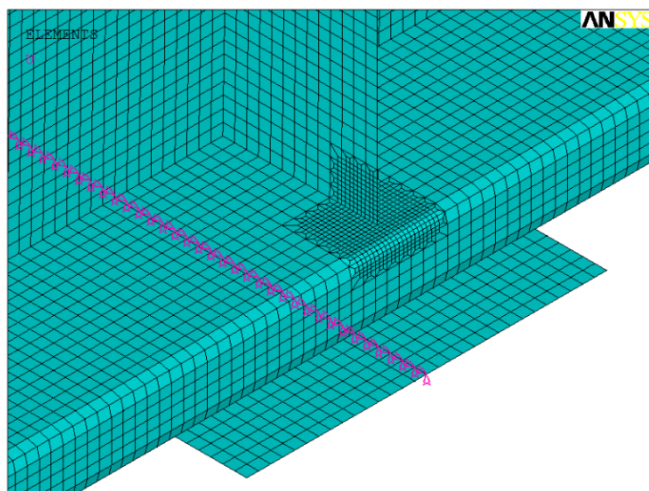


Fig. 13. Mesh refinement and restraint conditions located at the base of the plate that redistributes reaction forces at supports.

The geometry of each numerical model was developed consistently with the measured dimensions because small deviations from nominal values were detected, as described in Section 2.1. Local imperfections were not directly measured; nonetheless, they were introduced by means of an elastic buckling analysis. In particular, the lowest local buckling mode shape involving the compression flange was introduced into the model, as depicted in Fig. 14.

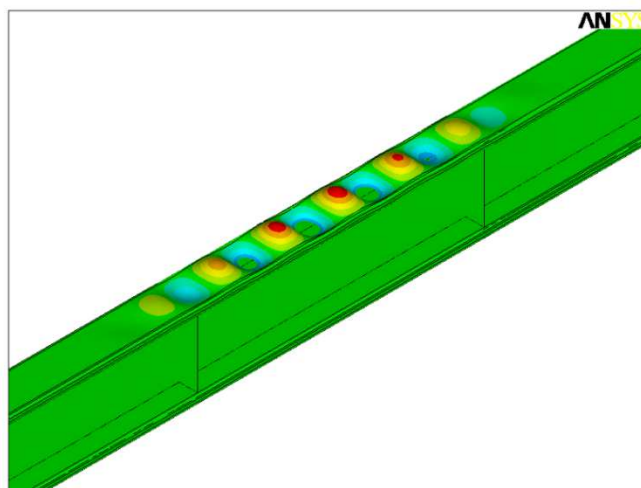


Fig. 14. Lowest local buckling mode shape of the compression flange.

Moreover, an imperfection of the web was also implemented. The amplitude of the imperfections was selected by following the approach proposed by Schafer and Peköz

[22]. In this respect, the maximum amplitude was assumed as a function of the element width according to the Eq (1) [22]:

$$d = 0.006w \quad (1)$$

where w is the element width and d represents the maximum imperfection amplitude. Analyses with different values of amplitude introduced in the web and in the top tube were performed and the ultimate load was compared with the experimental one. The amplitude values that better agreed with the experimental ultimate load corresponded to the maximum amplitude values as given in Eq (1) and they were then retained in all numerical simulations. For instance, the imperfection amplitude of the tube flange is about $d = 0.6$ mm for RHF B-240 and $d = 0.9$ mm for RHF B-300, respectively. In order to consider possible antisymmetric local buckling loads, the whole specimens were modelled.

5.2 Application of loads and restraints

Restraints were applied to the plates that were used to distribute the reaction forces at supports. In detail, a roller and a hinge were modelled at the supports by assigning the relevant condition to all nodes along a line strip below the plate support located underneath the bottom tube flange, as illustrated in Fig. 13. The plate and the bottom tube flange were connected together by means of rigid constraint equations – CERIG command [25] -. Finally, in order to prevent lateral torsional buckling and consistently with the experimental setup, restraints against horizontal displacement were punctually introduced along the top tube flange.

The load was applied by imposing increasing vertical displacement to the nodes of the web stiffeners located at half meter from the midspan. In this way, the evolution of the softening branch could be followed.

5.3 Material properties

The material mechanical properties implemented into the numerical model were derived directly from tensile tests on beam specimens drawn from the web and the tube flats. The cold working enhancement was not included in the corner zones because the membrane residual stresses were not modelled: in fact, they tend to counteract one another [22,26] as described in Section 4. The material constitutive law included the flexural residual stresses, as described in Section 2. True stress – strain relationships were employed for material properties because more representative of the state of material in large strain analyses. They read [25]:

$$\sigma_t = \sigma_e (1 + \varepsilon_e) \quad (2a)$$

$$\varepsilon_t = \ln(1 + \varepsilon_e) \quad (2b)$$

Where σ_t is the true stress, σ_e is the engineering stress, ε_t is the true strain and ε_e is the engineering strain.

The Poisson's ratio was taken equal to 0.30. The Multilinear Isotropic Hardening (MISO) material law was used for implementing the true stress – strain data. It allows including a user-defined stress-strain relationship by means of several linear segments. The MISO material is suitable for steel modelling because it relies on the Von Mises yield criterion. Moreover, an isotropic hardening rule was deemed adequate for the purpose because of the monotonic nature of the experimental tests.

5.4 Analysis of the results

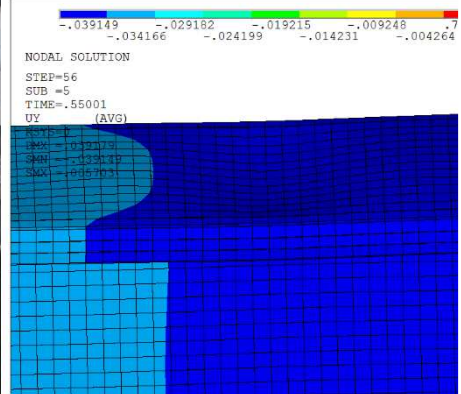
In order to verify the accuracy of the numerical model, the ultimate moment capacity and the failure mode obtained from the numerical analyses were compared with the test outcomes. From Table 5 it is possible to observe that good agreement between numerical and experimental results was achieved by comparing the ultimate moment capacity M_u and the displacement δ_u at M_u . Moreover, the mode of failure that involved the main spatial plastic mechanism of the top compression flange was well captured for both sections profiles, as illustrated in Fig. 15a-d. Fig. 15e-f show that web buckling was also well represented by the numerical models of RHFB-300 specimens. However, looking in detail at the mode of failures depicted in Fig. 15g-h, the FE model of the RHFB-240 specimens was not capable of detecting some minor plasticization mechanisms occurred early in the tests. As stated above, these profiles were more affected by imperfections and by local effects owing to smaller thicknesses and the production process. This phenomenon determined an increase in deformability of the specimens that is shown by the difference in elastic branch behaviour between tests and numerical analyses, as illustrated in Fig. 16a-c. This is more evident in T02 RHFB-240 and T03 RHFB-240, whilst for T01 RHFB-240 the bending moment at which the formation of a minor plastic mechanism occurs, is delayed and clearly highlighted by sudden deviation from linear behaviour. Nevertheless, the ultimate values of RHFB-240 numerical analyses were not significantly affected. In RHFB-300 tests, early minor local plasticization was not detected, and the numerical elastic behaviour well agrees with the experimental one, as illustrated in Fig. 16d-f.

Table 5. Comparison of the flexural behaviour between numerical and experimental results.

	$M_{u,FE} / M_{u,TEST}$	$\delta_{u,FE} / \delta_{u,TEST}$
T01 RHFB-240	1.02	0.90
T03 RHFB-240	1.05	0.93
T04 RHFB-240	1.04	0.93
T05 RHFB-300	1.03	0.98
T06 RHFB-300	0.98	0.81
T07 RHFB-300	1.04	0.95
Average	1.03	0.92
COV	0.02	0.06



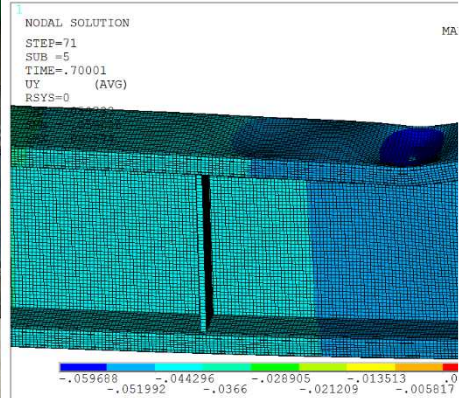
(a)



(b)



(c)



(d)

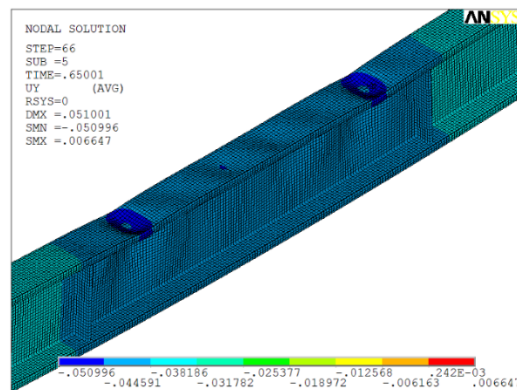
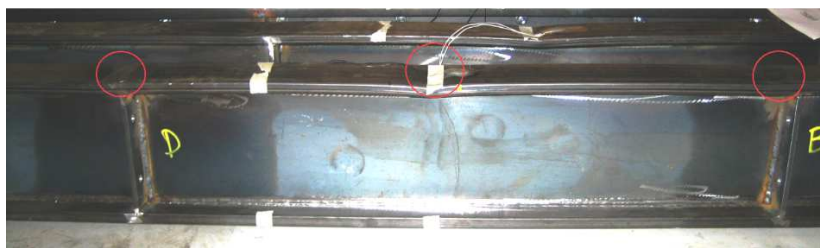
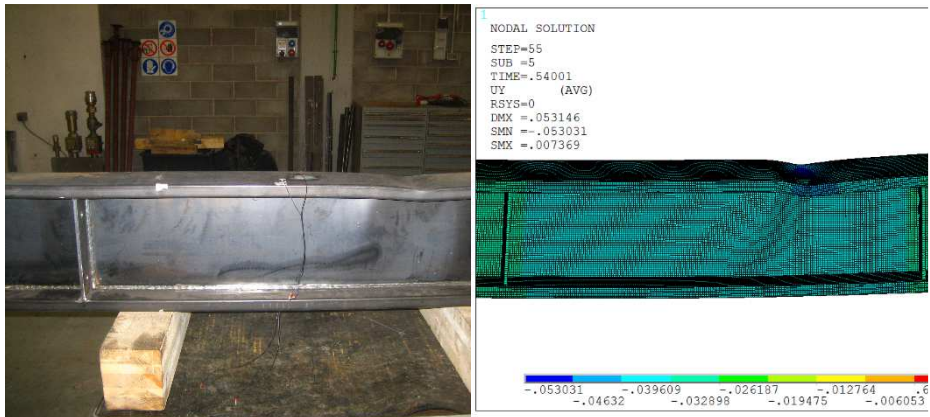
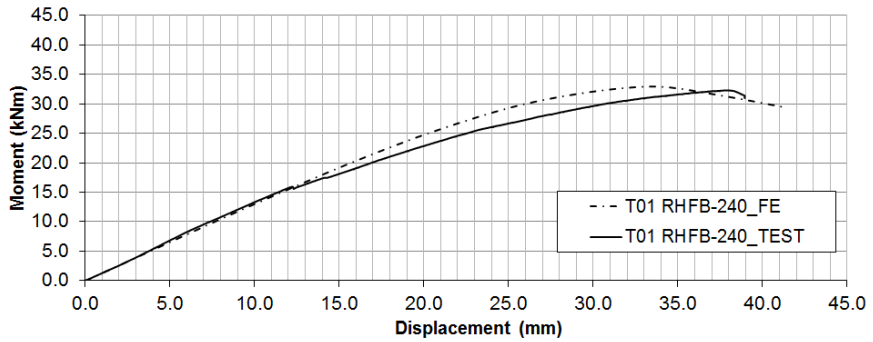
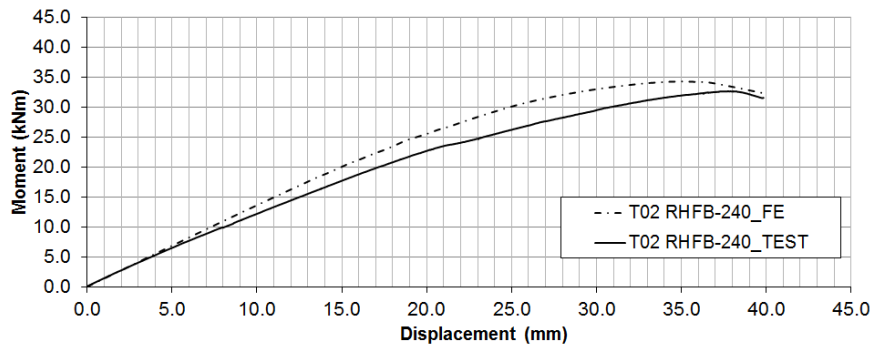


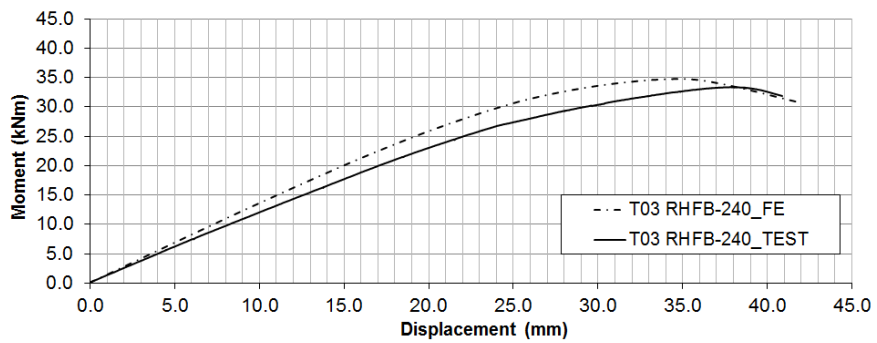
Fig. 15. Comparison of the mode of failure: a) main plastic mechanism RHFB-240 test; b) main plastic mechanism RHFB-240 FE; c) main plastic mechanism RHFB-300 test; d) main plastic mechanism RHFB-300 FE; e) web buckling RHFB-300 test; f) web buckling RHFB-300 FE; g) plastic mechanisms in RHFB-240 test; h) plastic mechanisms in the RHFB-240 FE analysis.



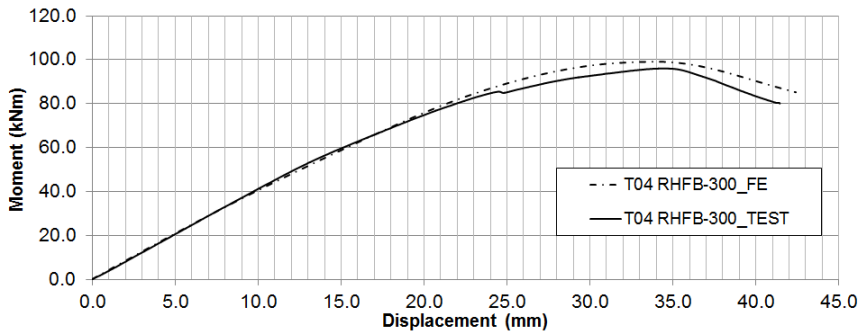
(a)



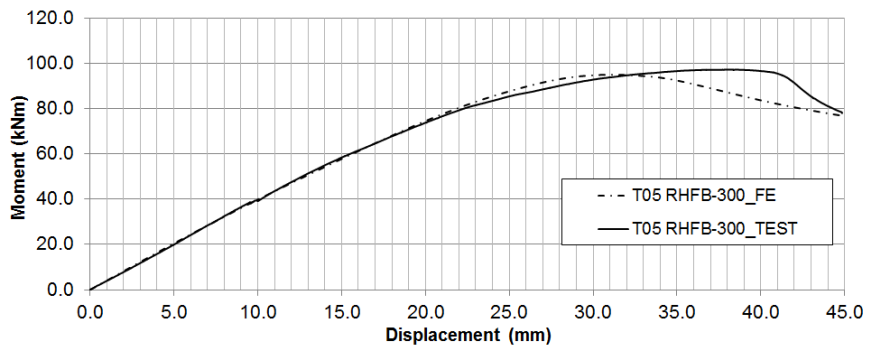
(b)



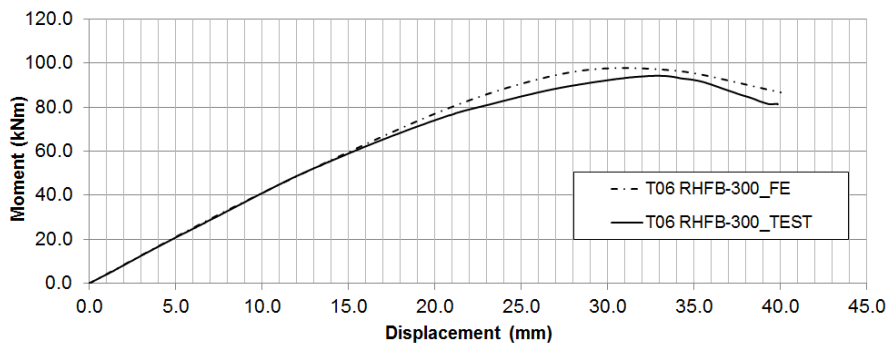
(c)



(d)



(e)

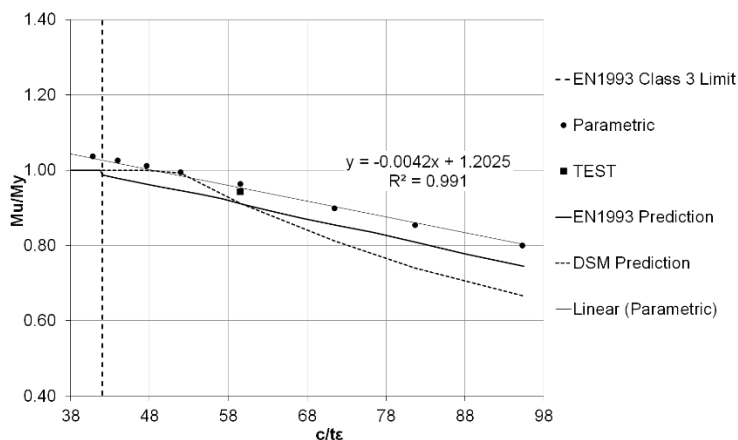


(f)

Fig. 16. Comparison of bending moment-displacement curves: a) T01 RHFB-240; b) T02 RHFB-240; c) T03 RHFB-240; d) T04 RHFB-300; e) T05 RHFB-300; f) T06 RHFB-300.

6 PARAMETRIC STUDIES

In order to broaden the available findings over a wider slenderness range of the tubes composing the flanges, a series of parametric studies was conducted. Material properties representative of material coupon tests that include flexural residual stresses were used in the parametric analyses. Local geometric imperfections were modelled by means of the lowest buckling mode shape. The amplitude of local imperfections was introduced according to Eq. (1). No global geometric imperfections were included because global buckling was prevented. A 4-point bending scheme was used with span of the beams set to 4 m and a distance of 1 m between the point loads. The effect of the moment gradient was not investigated as it was found to be negligible with respect to moment capacity of carbon steel [27] and stainless steel flexural members [28]. The dimensions of the cross section were the ones of the T01 RHF B-240 profile and the T04 RHF B-300 profile but the thickness, that was varied between 1.2 mm and 4 mm for the RHF B-240 profile and between 1.8 mm and 5 mm for the RHF B-300 cross section, respectively. The limit of a Class 3 section according to the EN1993-1-1 [19] was assessed by plotting the normalised ultimate moment M_u over the elastic bending moment M_y with respect to the most limiting $c/t\varepsilon$ slenderness value that was the tube flange in compression, where c is the flat width of the plate element, t its thickness and $\varepsilon = \sqrt{(235/f_y)}$. $M_y = M_y.f$, as described in Section 4, was employed. As expected, the parametric study showed no considerable difference between the two cross sections owing to geometry similarity normalised with respect to the material strength. In fact, from Fig. 17 it is possible to observe that trend line obtained through linear regression has same slope and intercept values. From Fig. 17 it is possible to note that EN1993 tends to be conservative by underestimating the flexural capacity of RHF B cross-sections. The Class 3 limit is also conservative: from the parametric analyses the onset of local buckling of the tube flange in compression, i.e. when $M_u/M_y < 1$, is observed for $c/t\varepsilon$ equal to about 48 instead of 42. Nevertheless, the EN1993 prediction exhibits a M_u/M_y vs. $c/t\varepsilon$ evolution that follows well the trend of FE results.



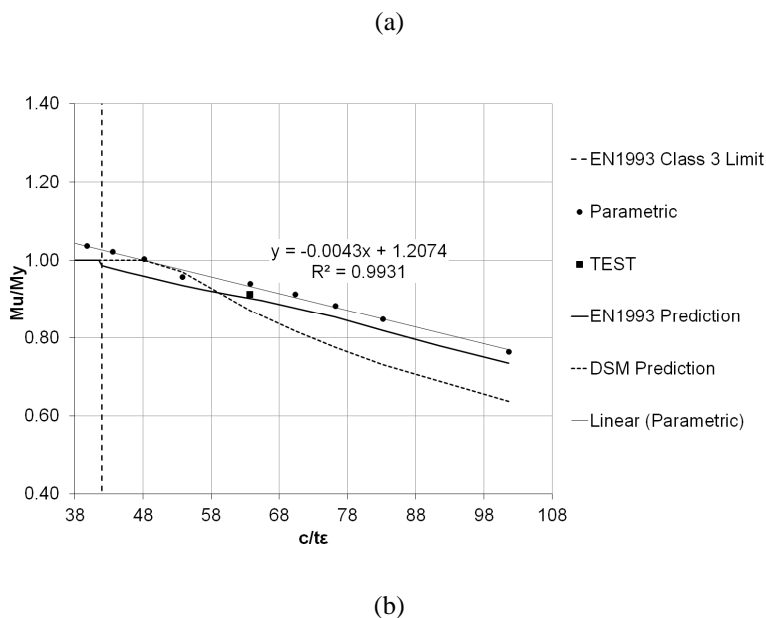


Fig. 17. Parametric analysis: a) RHF240; b) RHF230.

Furthermore, the capability of the DSM [2] to predict the flexural behaviour of RHF240s was investigated. The main idea behind this method is the determination of all elastic instabilities, i.e. local M_{crl} , distortional M_{crd} , global buckling M_{cre} and the bending moment that causes yield, i.e. M_y . The smallest moment among M_{crl} , M_{crd} , M_{cre} and M_y identifies the bending resistance of the section. Since lateral-torsional buckling and lateral-distortional buckling do not apply to the case study, only local buckling is considered, as illustrated in the finite strip solution depicted in Fig. 18 [29]. It is worth to point out that for comparison purposes input data of finite strip analyses in terms of geometry of the cross section and mechanical properties, i.e. yield strength, elastic modulus and Poisson's coefficient, were chosen consistently with the FE analyses. The stress distribution was assumed according to the M_{yf} . No imperfections were included and bending resistance beyond the elastic bending moment is not estimated. Thus, it is interesting to observe when local buckling becomes significant and affects the flexural strength of the beam by preventing the attainment of the elastic bending moment. Fig. 17a and b show that the DSM provides a good prediction for $c/t\epsilon$ slenderness value up to 55, then it tends to significantly underestimate the flexural strength ($c/t\epsilon > 60$).

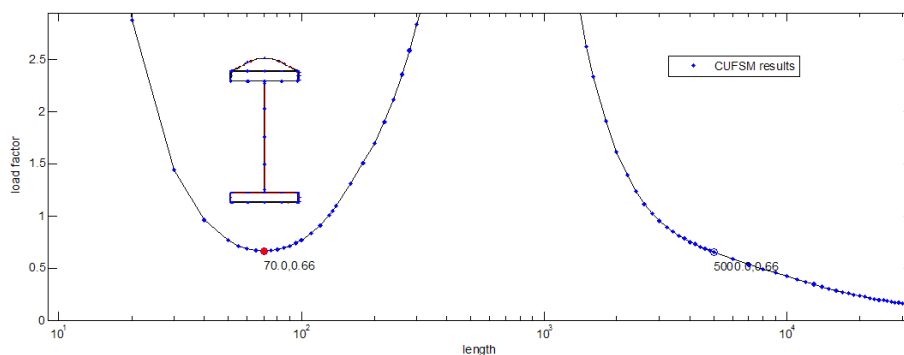


Fig. 18. Finite strip analysis of a RHFB-240 profile with thickness equal to 1.4 mm.

7 CONCLUSIONS

The article reported the results of a comprehensive experimental-numerical study on cold-formed laterally-restrained steel rectangular hollow flange beams (RHFBs) that was carried out in order to investigate their flexural capacity. The behaviour of RHFB-300 specimens was influenced by a significant difference in yield strength between the tubes and the web that induced local buckling and plastic behaviour in the web. All experimental tests showed well-distributed local buckling waves on the compression top flange. Some minor plasticization was observed outside the zone between the point loads owing to local imperfections associated with still significant bending moment close to the constant bending moment region. Furthermore, the RHFB-240 profiles exhibited minor plasticization, that caused an early loss of stiffness, prematurely in the tests because more prone to be affected by local imperfections and by local effects that were emphasized by a lack of optimisation in the way of production. In this respect, in order to reduce imperfections a more systematic production process with a dedicated cut machine is recommended. Along this line, the insertion of an intermediate stiffener in the external plates of the hollow flanges is beneficial for increasing the local buckling critical load of the plate. Nevertheless, the exploitation of such profiles can be attractive for structural applications as secondary beams in small-framed houses because of favourable flexural performance/weight ratio.

Calibration of the numerical model provided good agreement with experimental tests in terms of ultimate bending moment, ultimate displacement, mode of failure. The initial elastic stiffness was well reproduced in RHFB-300 beams whereas the FE was not capable of detecting some minor plasticization occurred early in the RHFB-240 specimen tests owing to local imperfections and local effects. Parametric analyses showed that both EN1993 and DSM tend to be conservative in predicting the section bending capacity of RHFB profiles. Nonetheless, the EN1993 prediction exhibits a M_u/M_y vs $c/t\epsilon$ evolution that follows well the trend provided by the FE results whereas DSM provides a good prediction for $c/t\epsilon$ slenderness value up to 55, then it tends to

significantly underestimate the flexural capacity of RHFB for high slenderness ratios ($c/t\epsilon > 60$) of the tube compression flange.

8 ACKNOWLEDGEMENTS

Dr. N. Tondini and the experimental programme have been supported by the Province of Trento through the Call 3 - post-doc 2009 (Outgoing) - FIRAS project, which is gratefully acknowledged. The steelwork company Gruppo Manni and in particular Eng. Adolfo Bozzoli are also gratefully acknowledged.

9 REFERENCES

- [1] Hancock GJ, Cold-formed steel structures; *Journal of Constructional Steel Research* 2003; 59:473-487.
- [2] Schafer BW. Review: The Direct Strength Method of cold-formed steel member design; *Journal of Constructional Steel Research* 2008; 64:766-778.
- [3] Li Z, Batista Abreu JC, Leng J, Ádány S, Schafer BW. Review: Constrained finite strip method developments and applications in cold-formed steel design, *Thin-Walled Structures* 2014; 81:2–18.
- [4] Lee YH, Tan CS, Mohammad S, Tahir MM, Shek PN. Review on Cold-Formed Steel Connections, *The Scientific World Journal* 2014; 1-11.
- [5] Wang L, Young B. Design of cold-formed steel channels with stiffened webs subjected to bending, *Thin-Walled Structures* 2014; 85:81–92.
- [6] Mahendran M, Keerthan P, Experimental studies of the shear behavior and strength of LiteSteel beams with stiffened web openings, *Engineering Structures* 2013; 49:840–854.
- [7] Anapayan T, Mahendran M. Improved design rules for hollow flange sections subject to lateral distortional buckling, *Thin-Walled Structures* 2012; 50:128-140.
- [8] Anapayan T, Mahendran M, Mahaarachchi D. Section moment capacity tests of LiteSteel beams, *Thin-Walled Structures* 2011, 49:502–512.
- [9] Anapayan T, Mahendran M, Mahaarachchi D. Lateral distortional buckling tests of a new hollow flange channel beam, *Thin-Walled Structures* 2011, 49:13–25.
- [10] Kurniawan CW, Mahendran M. Elastic lateral buckling of simply supported Lite Steel beams subject to transverse loading, *Thin-Walled Structures* 2009, 47:109–119.
- [11] Avery, P., Mahendran, M. Finite-element analysis of hollow flange beams with web stiffeners, *Journal of Structural Engineering* 1997; 123(9):1123-1129.
- [12] Mahendran M, Avery P. Buckling experiments on hollow flange beams with web stiffeners, *Journal of Structural Engineering* 1997; 123(9): 1130-1134.
- [13] Avery P, Mahendran M, Nasir A. Flexural capacity of hollow flange beams, *Journal of Constructional Steel Research* 2000; 53:201–223.
- [14] Hassanein MF, Kharoob OF, El Hadidy AM. Lateral–torsional buckling of hollow tubular flange plate girders with slender stiffened webs, *Thin-Walled Structures* 2013,

65:49–61.

- [15] Hassanein MF, Kharoob OF. Shear capacity of stiffened plate girders with compression tubular flanges and slender webs, *Thin-Walled Structures* 2013, 70:81–92.
- [16] Hassanein MF, Kharoob OF. Flexural strength of hollow tubular flange plate girders with slender stiffened webs under mid-span concentrated loads, *Thin-Walled Structures* 2013, 69:18–28.
- [17] Hassanein MF, Silvestre N. Lateral–distortional buckling of hollow tubular flange plate girders with slender unstiffened webs, *Engineering Structures* 2013, 56:572–584.
- [18] Hassanein MF. Shear strength of tubular flange plate girders with square web openings, *Engineering Structures* 2014, 58:92–104.
- [19] EN1993-1-1. Eurocode 3 Design of steel structures Part 1-1: General rules and rules for buildings, Bruxelles: CEN; 2005.
- [20] EN ISO 6892-1. Metallic materials – Tensile testing – Part 1: Method of test at room temperature, Bruxelles: CEN; 2009.
- [21] EN10025-2. Hot rolled products of structural steels - Part 2: Technical delivery conditions for non-alloy structural steels, Bruxelles: CEN; 2005.
- [22] Schafer BW, Peköz T. Computational modelling of cold-formed steel: characterizing geometric imperfections and residual stresses. *Journal of Constructional Steel Research* 1998, 47:193-210.
- [23] EN1993-1-3. Eurocode 3 - Design of steel structures - Part 1-3: General rules - Supplementary rules for cold-formed members and sheeting, Bruxelles: CEN; 2006.
- [24] EN1993-1-5. Eurocode 3 - Design of steel structures - Part 1-5: Plated structural elements, Bruxelles: CEN; 2006.
- [25] ANSYS. Documentation for ANSYS - Release 14.0. Copyright SAS IP, Inc., 2011.
- [26] Shifferaw Y, Schafer BW. Inelastic Bending Capacity of Cold-Formed Steel Members, *Journal of Structural Engineering* 2012; 138(4):468-480.
- [27] Kuhlmann U. Definition of flange slenderness limits on the basis of rotation capacity values. *Journal of Constructional Steel Research* 1989; 14(1):21-40.
- [28] Theofanous M, Gardner L. Experimental and numerical studies of lean duplex stainless steel beams. *Journal of Constructional Steel Research* 2010; 66:816-825.
- [29] Li Z, Schafer B W. Buckling analysis of cold-formed steel members with general boundary conditions using CUFSM: conventional and constrained finite strip methods. *Proceedings of the 20th International conference: Special Conference on Cold-Formed Steel Structures (St. Louis); 2010.*

TOPIC 2:

Coupling methodologies between a CFD and an FE software for the analysis of structures at high temperatures

1 Introduction

In recent years an increased interest towards the introduction of more reliable tools and methodologies concerning the evaluation of buildings structural behavior under fire action has developed between researchers. This was in part due to a regular and advantageous progress that involved the common upgrade of scientific civil structural knowledges. On the other hand, particular events, such as the collapse of the World Trade Center Tower 7 in 2001 [1] moved the attention towards the assessment of the effective reliability of structures involved in fire.

The Eurocodes, such as other structural design codes, have therefore provided new tools, by extending for example the records of available design fires to be used in order to assess the temperature field into the structural elements. As a consequence long-data gas-temperature curves, such as the standard ISO 834, have been sustained by the introduction of more detailed natural fire models (localized fire, zone models or CFD). These new tools allow to take into account with a higher level of realism fundamental phenomena such as the description of gas properties and mass and energy exchanges. Further an increase numbers of finite element software (ABAQUS, SAFIR, ANSYS, DIANA, etc.) have developed powerful computational tools that permit to perform nonlinear thermomechanical analyses of complex structures. An effort remains to be fulfilled in the deeper definition of the thermal gas temperature representative curves developed in relation with the range of possible natural fires. Therefore the integration of computational fluid dynamic software (CFD) and its coupling with finite element programs represents a desirable focus that should be investigated. The objective is fundamentally based on the introduction via zone models or CFD of a more realistic gas-phase development description by taking into account all physical phenomena and specific fire characteristics that may be connected to conditions and place in which the fire spreads. In this sense the ECSC research project, has introduced a new approach, called Natural Fire Safety Concept (NFSC) that is fundamentally based on the development of new strategies that reconsider with a more detailed order of accuracy the structural building safety by introducing new methodologies such for instance the CFD-FE coupling.

The present work analyses these issues, by introducing through a practical application, the possibility to effectively perform the coupling procedure between a CFD and an FE finite element software. The purpose is also focused in the understanding and definition

of the capabilities but also limitations that could be involved in the use of such procedures by finally comparing the obtained results with the outcomes that are instead derivable by using conventional and outdated design models.

2 CFD and FE software

The analysis of structures subjected to high temperatures requires the knowledge of appropriate tools and computation methods needed to initially define the characteristics of the fire and then perform thermomechanical analyses. As previously mentioned the Eurocode code reports for instance a list of fire models that could be used in the design practice. The code differentiates between the use of nominal temperature-time curves and natural fires.

Nominal temperature-time curves are based on ISO 834 Standard curve, External fire curve or Hydrocarbon curve that represent simplified fire models not able to take into account for instance the effective fire load density or ventilation conditions. Although these curves are widely diffused in the practice, they should, in the context of NFSC, be replaced by the introduction of natural fire models. Between them, Eurocode specifies the presence of advance fire models able to effectively consider gas properties, mass and energy exchange. Natural advance fire models are available based on One-zone Two-zone or Computational fluid dynamic (CFD) models. In particular CFD models are able to offer the temperature evolution in the compartment in a completely time dependent and space dependent manner and actually represents the more detailed way of analysis for describing the development of a fire.

Computational fluid dynamics solves the Navier-Stokes equations (momentum and mass conservation) and related diffusion transport equivalence (energy and species conservation) both for laminar and turbulent fluid. The output data (values of temperature, velocity, radiant intensity etc.) are obtained for each spatial grid point that is used to discretize the compartment. CFD is therefore an advanced modelling and sophisticated tool to represent the fire development. However, due to its complexity, specific expertise is needed to adequately model the involved phenomena. Moreover, it requires high computational demand and in coupling approach it is just the first step before solving the heat transfer analysis and the mechanical response of the structure. Some example of CFD-FE coupling procedures have been studied inside the Firestruct project [2] by interconnecting CFD models as JASMINE (1987), VESTA (2007) and FDS (2004) with the solid phase models SAFIR, DIANA and ANSYS.

In this work, we mainly focused on the application of Fire Dynamic Simulator (FDS) coupled with the FE software SAFIR.

Before introducing the methodology and assumptions that are at the base of the coupling approach, a brief summary, of the features of two codes is reported below.

2.1 Fire Dynamics Simulator (Mc Grattan et al., NIST) [3]

FDS is a computational fluid dynamics model of fire-driven fluid flow. FDS solves numerically a form of the Navier-Stokes equations appropriate for low-speed, thermally-driven flow with an emphasis on smoke and heat transport from fires. FDS is particularly suitable for solving practical fire problems in fire protection engineering, while at the same time it provides a tool to study fundamental fire dynamics and combustion. The program implements a model of turbulence that is treated by means of large eddy simulation although it is possible to use also the Direct Numerical Simulation (DNS). The combustion model is based on a single step, mixing-controlled chemical reaction which uses three lumped species (air, fuel and products). Radiative heat transfer is included in the model via the solution of the radiation transport equation for a grey gas, and in some limited cases using a wide band model. Boundary conditions are taken into account in the fire scenario. All solid surfaces are assigned thermal boundary conditions, plus information about the burning behavior of the material. Heat and mass transfer to and from solid surfaces is usually handled with empirical correlations. Effects of wind or different pressure through openings could be also modelled.

2.2 SAFIR (J-M. Franssen, University of Liege) [4]

SAFIR is a special purpose computer program that is specifically designed for structures involved in fire. However it can also be employed for the design at ambient temperature. It was developed at the University of Liege, Belgium, by Jean-Marc Franssen as the second generation of the structural fire code CEFICOSS. The program is based on the classical Finite Element Method and it allows to study one, two or three-dimensional structures. Different types of finite elements are implemented in the program (solid, beam, shell, truss elements). Functionally the software divides the thermomechanical analysis into two separate and consequential steps: at the beginning a thermal analysis is performed and the temperature in the structural element is obtained, subsequently based on the thermal response the mechanical behavior is computed. With reference to first phase the field of temperature in the cross section is obtained by assigning boundary condition to selected surface through generic time-temperature gas curve or external heat fluxes. The possibility to introduce the effect of localized fire, such as the Hasemi model reported in EN1991-1-2, is also allowed. The mechanical behavior is then computed by integrating the degraded materials mechanical properties with the appropriate stress-strain relation at high temperatures and taking into account the effects of thermal dilatation, material nonlinearity, geometrical nonlinearity and large displacements that influence the structural behavior under the specific load configuration.

3 Definition of different levels of coupling

The application of CFD-FE coupling methodologies for the study of structures subjected to fire allows to handle the analysis of thermomechanical structural response with a higher order of detail. A continuous and reversible exchange of informations and data can be performed during the numerical simulation by taking advantage of the specific capabilities of each tool (CFD or FE software). Three problems have to be solved when modelling the behaviour of a structure subjected to a compartment fire, each of them being governed by a different physical phenomenon and, hence, by different equations:

- 1) Definition of the temperature development in the compartment
- 2) Computation of the thermal response of the structure
- 3) Determination of the mechanical response

The fire development analysis yields the temperatures of gases and the radiative and mass flows in the compartment. By means of the thermal analysis, the temperatures in the structural elements are obtained. The mechanical response provides the behavior of the structural system, i.e. stresses, deflections, etc. Thus, some issues arise when an integrated modelling methodology CFD-FE is to be used to tackle the whole problem. It is natural to assign the task of performing the analysis of the compartment fire development to the CFD model and the mechanical response to the FE model, but it is not so straightforward to decide where to carry out the thermal analysis in the structural elements. Both software may be exploited to fulfil the task.

The coupling process refers to the level of interactions that are exchanged between the three problems. Different levels of coupling could be introduced by taking into account or alternatively omitting the mutual interactions that are involved. Fig.1 shows the possible levels of coupling. In detail the figure refers to the more complex level of coupling in which all the interactions between the three problems are considered. This methodology is called as “full coupling” approach or “two way coupling”.

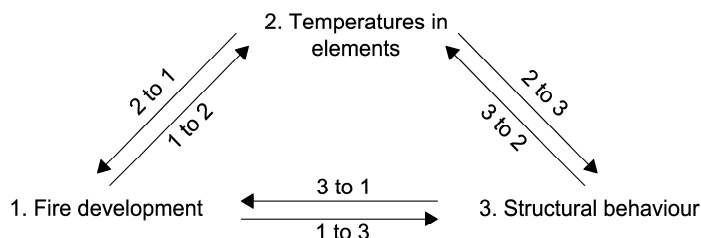


Fig.1 Full coupling approach between the three steps involved in the fire analysis

More in detail with reference to Fig.1:

From 1 to 2, the values of gas temperatures, radiative heat fluxes and convective coefficients, computed in 1 are then used to perform the heat transfer analysis in 2. Vice

versa step 2-1 allows to take into account in the fire development the effects of modified element temperature computed in 2 or the absorption of energy in the compartment. Coupling between 2-3 allows to transfer the thermal field of temperature of elements performed in 2 to point 3 in order to compute the structural behavior. Vice versa step 3-1 could be introduced by taking into account deformations (cracks or gaps induced in the cross section) and their effects on the section temperature propagation at the previous point.

Coupling step 1-3 and 3-1 means instead consider for instance the effect of the deflections obtained at point 3 in the modification of the gas flow computed at point 1. An example of a full coupling or two way approach is referred in Kumar et al [2] between VESTA a CFD software and DIANA an FE software.

Nevertheless the employment of a full coupling procedure could be problematic because presumably only specific CFD software could be compatible with other FE programs and vice versa. In addition the inclusion of structural elements in the fire model, that is necessary to take into account the exchange phenomena between step 1-3 and 3-1, is hazardous due to possible changes that are generally performed on the structural layout during construction processes. In these cases new analyses would be rerun whenever a consistent variation is applied.

For that reasons the present work has been focused on the description of a methodology that reduce the level of mutual interactions that are potentially included in the model. The proposed approach is here referred as “weak coupling” or “one way coupling”. It allows to reduce the level of interactions but at the same time it optimizes time of analysis and avoid aforementioned issues by proposing a more practical method that could be extended to the study of a wide number of cases.

3.1 Weak coupling approach

In the weak coupling approach all the mutual interactions are discarded (see Fig.2). The analysis is reduced to a first step (1 to 2) in which the information regarding the fire development, computed inside a CFD software, are transferred to a FE program that performs a thermal analysis of the structural element and subsequently the mechanical structural response (point 3). In this methodology all the analyses are sequential. As a consequence the number of simulations that must be rerun if a change is performed in the structure geometry are drastically reduced. In addition the computational weight is decreased due to the fact that the exchange of data between the two software is present only between step 1-2 where a transfer data file containing the information of the fire should be produced in order to successively compute the thermal temperature of the elements.

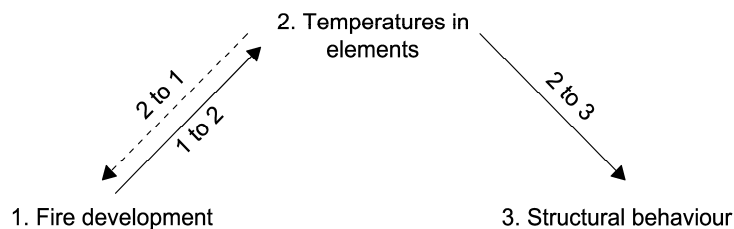


Fig.2 Weak coupling approach between the three steps involved in the fire analysis

Nonetheless, these simplifications imply some limitations that are discussed in detail in the attached paper [5].

4 Weak coupling CFD-FE approach: practical description of the procedure

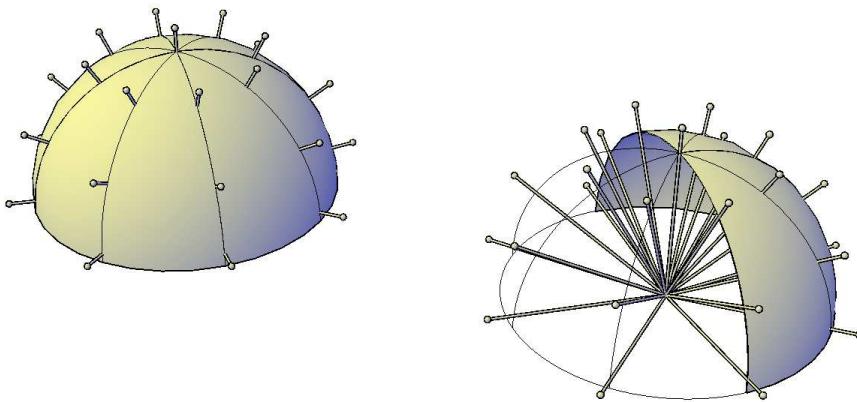
In the previous section the idea at the base of a “full” or “weak coupling approach” were presented by underlining the capabilities and the inner limits that potentially derive by the choice of one or the other procedure. Herein we mainly focused in the study of the weak coupling approach, by now introducing in the practice how this methodology is effectively achieved. The reported method refers specifically to the coupling procedure performed through the use of Fire Dynamics Simulator (for the CFD modeling of fire development) and the finite element program SAFIR for the study of thermal and mechanical response. Similar procedures based on the use of different couples of software (VESTA-DIANA, JASMINE-STELA, FDS-ANSYS and JASMINE-SAFIR) are discussed in [2].

The first step consists in the CFD modeling of the compartment on the basis of the significant fire scenario that is identified by the designer. At this level a compatibility in terms of coordinates reference system between the CFD and FE models should be recommended in order to avoid unnecessary transformations, that otherwise should be performed in the FE simulation. The model requires the definition of openings, boundary contours as presence of walls slabs or permanent obstructions and their relative thermal properties. The characteristics of the fire as the fuel chemical properties or the rate of heat release have then to be defined. The presence of winds effects, variation of pressure through openings or the activation of ventilation systems or sprinkler should be also introduced.

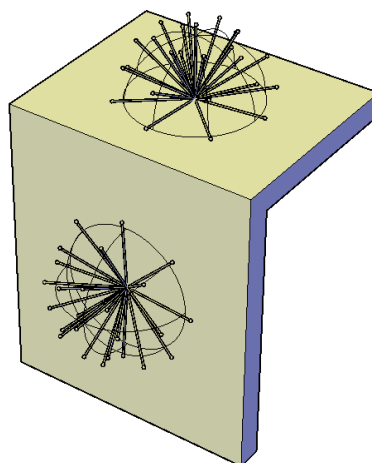
The CFD analysis is carried out by means of a thoughtful choice of the grid mesh size, analysis time-step, introduction of appropriate parameters for the radiation and combustion model. At the end of the analysis a transfer file is produced by the CFD program and written in an ASCII file format. This file contains the coordinates of the transfer point (that is the central point of each element of the mesh) and the number of directions in which radiant intensities and fluxes are given. These data are provided at each time-step and for each transfer point. The ASCII file contains also the computed gas temperatures and coefficients of convection. A Cartesian spatial interpolation is

then performed in SAFIR software at every time-step. The interpolation is necessary because the CFD transfer points generally not correspond to the structural points that are located in the nodeline of the beam elements or in the centerline of the slab (modeled by shell elements).

In order to provide a sufficient number of transfer points, it's always recommendable that the size of the spatial CFD domain is greater with respect to the minimum contour that includes all the structural elements, in this way all the structural points are surrounded by a sufficient number of transfer points that allow a correct interpolation. In addition a second linear interpolation, in the time domain, is also needed due to the different time step that could be used in the CFD simulation and in the thermal analysis. When the process of interpolation is finally completed, the information about gas temperature, radiant intensities and coefficient of convection are available for each structural point. With reference to gas temperature and convection coefficient, the correlation between provided data and structural point is univocal, since there is only one scalar value (one for gas temperature and one for convective coefficient) associated to the correspondent structural point. In the case of radiant intensities several values, whose total number is initially defined by the user, are given for one structural point. Each value represents a computed radiant intensities associated to a specific directions defined in the Cartesian system. In order to compute the impinging flux associated to the structural point all these intensities have to be integrated at the surface of the structure. The integration is performed on a hemisphere (Fig. 3a) oriented following the normal of the structural surface Fig.3b.



(a)



(b)

Fig.3 Integration of the radiant intensities necessary to compute the impinging flux on structural elements; a) Radiant intensities incoming on a hemisphere (The number of radiant intensities is purely representative), b) Necessity of a spherical interpolation due to different surfaces orientation.

It is noted that the directions of the intensities used for the integration are not the same initially given by the CFD analysis and relative transfer file. This mainly due to the different orientation of the structural elements towards the reference system of coordinate in the CFD model (Fig.3b). Another spherical interpolation has then to be performed in order to provide the definitive orientation of the radiant intensities to introduce in the formula for the integration of the impinging flux. The computed flux is then given by:

$$q = \sum_{i=1}^n I_i \cos \theta_i \omega_i \tag{1}$$

where n is the number of intensities considered for the integration, ω_i is the solid angle associated to the direction i , θ_i is the angle between the direction of the radiant intensity i and the normal to the surface, while I_i is the radiant intensity associated with the i -direction.

In the case of HE or IPE steel profiles, the determination of the shadow effects is important. As reported in [2] an algorithm of ray shooting from the surface to all the other surfaces of the section finds the angle of visibility towards the environment. With reference to Fig.4, if a local system of spherical coordinates is collocated on the surface of the element (with the polar system axis x parallel to the longitudinal axis of the beam), the integration is performed in the longitude window relying on the α view angle while for the latitude the integration is performed from $-\pi/2$ to $\pi/2$.

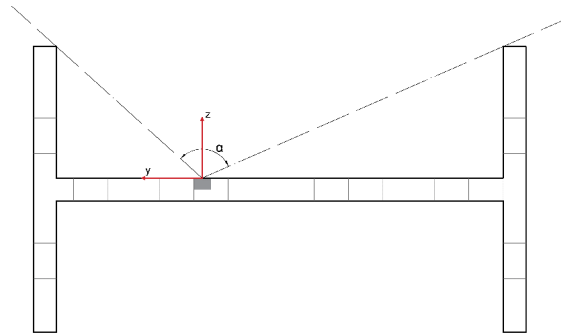


Fig.4 Determination of the angle of visibility for an IPE profile

5 Behaviour of real steel-concrete open car park subjected to localized fires

A practical case study, based on a composite steel-concrete car park, will be introduced in Section 6 to better understand the methodology at the base of the weak coupling approach. For that reason the fire performance of a multi-storey steel-concrete composite open car park, designed according to the Eurocodes [6,7], is analyzed through the coupling of a CFD and a FE software. The developed procedure is also compared with the outcomes arising from the use of a typical and simplified design approach (reported in the EN 1991-1-2 [7]), based on the Hasemi localized fire model. The purpose is addressed to evaluate the differences, in terms of structural response, due to a different choice of fire model and design methodology. Before discussing the results of the numerical analyses on the specific case study, some evidences about the real and effectively observed fire behavior of similar steel concrete composite structures designed for the same occupancy are herein reported. In particular we refer to structural fire tests performed on a 15x32 m open car park, as part of a European research project involving CTICM (France), ARBED (Luxembourg) and TNO (Netherlands) partners. The dimensional characteristics of the tested structure are reported in Fig.5.

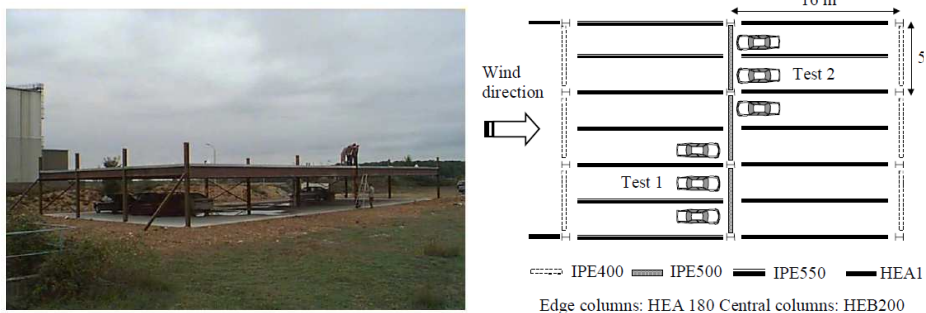


Fig.5 Experimental fire test on a real scale steel-concrete composite car park realized in France;
 a) View of the overall geometry, b) Plan view [9-10]

The tests took place in France in 1999 and involved two different experiments both realized by the usage of three adjacent burning cars that are collocated in different position of the floor area (see Fig. 5b). This specific fire scenario (three adjacent cars) was adopted because estimated the most severe in relation with the statistics provided from fire brigade [10]. The structure was realized with common steel profiles (IPE for beams and HEA/HEB for columns) and by means of a concrete composite slab of thickness 120mm (COFRASTRA 40). All the elements were unprotected. Fire was activated in the mid-car and successively independently propagated towards the two adjacent cars. The authors [8] reported the following considerations:

-the propagation of fire from the ignited car to the adjacent cars was always observed, but the time of propagation was significantly different due to the modified wind conditions observed during the two tests (wind was stronger in Test 2). This produced effects also in the determination of the total duration of the fire (see Fig. 6a). Nevertheless in both cases the maximum heating of the structural elements was comparable (see Fig. 6b).

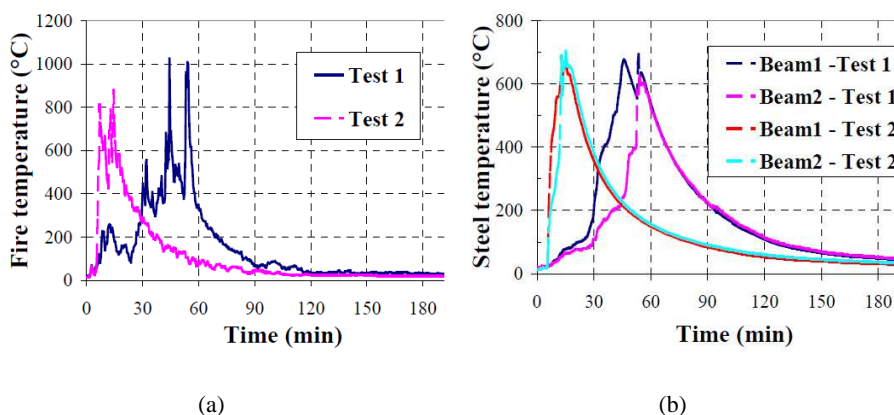


Fig.6 Experimental outputs; a) Measured temperature of gases, b) Temperature registered in the secondary steel beams [8]

-the deflection of midspan point of secondary beams (see Fig.7b) were significantly different in the two tests. This is justifiable again for the modified wind conditions and in particular as a consequence of wind direction in relation to cars position. In particular during Test 1, with light wind, the propagation of fire between the involved cars was slowly and the direction of wind pushed the flames outside the span beams by consequently reducing the heating area. On the other hand in Test 2 the wind pushed the flame towards the beam midspan by increasing the heating area. The maximum deflection in this case was raised before, due to the fact that fire diffused quickly among the involved cars with a higher magnitude of displacement.

-in both tests the effect of fire and relative structure deformations are far from cause the collapse of the structure.

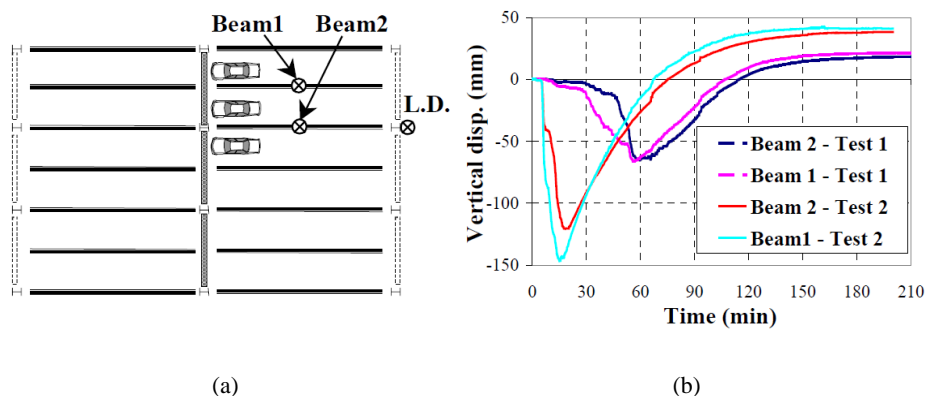


Fig.7 Experimental outputs; a) Position of the detection points for the measure of displacement, b) Vertical displacement of selected beam points [8]

The aforementioned experimental fire test, although not directly comparable to case study introduced in Section 6 (for geometry, structural elements size etc.), supports the objectives to be pursued in the context of the introduction of advanced methods for the thermomechanical analysis of structures. At first the test demonstrates that the fire resistance of suitably sized and designed steel-concrete structures could be satisfactory and not require the use of additional fire protections in order to avoid structural collapse. Secondly the use of simplified methods of analysis such as the use of standard fire curves or simplified localized fire model is too penalizing and not consistent with the real observations. Advanced methods are then suggested in order to capture the real behavior under exceptional actions and offer a more realistic definition of the problem. The CFD – FE coupling methodology that is finally introduced in next paragraph, through a practical application, represents in this sense a significant upgrade as means of investigation that should be introduced also in the design practice.

6 Case study: a steel-concrete open car park, CFD-FE weak coupling

A multi storey steel-concrete open car park, was investigated by means of a weak coupling CFD-FE procedure by at the same time comparing the obtained results with the outcomes deriving by the use of a simplified and less computationally demanding approach based on the Hasemi fire model (EN 1991-1-2 [7]). The geometry and characteristics of the car park are reported in the attached paper [5].

The analysis starts from the identification of all significant fire scenarios that have to be taken into account in order to investigate the most severe fire configuration. The INERIS document [11] was followed in this process by at the end defining the reference scenario in Fig. 8a. The delay time necessary for the ignition of the adjacent cars is fixed, following again [11], in 12 minutes. The severity of the chosen fire scenario was also confirmed by the preliminary FE analyses, performed with the Hasemi model, on other significant fire scenarios discussed in [5]. The CFD-FE coupling, that is extremely time-consuming was then applied only with reference to this fire scenario. In order to

evaluate the performance of the open car park a 3D finite element model, used both for the application of the Hasemi fire model and the introduction of weak coupling approach was realized in SAFIR. Only one half of the car park was modelled by considering that for that typology is extremely unlikely that the fire could diffuse to all floors.

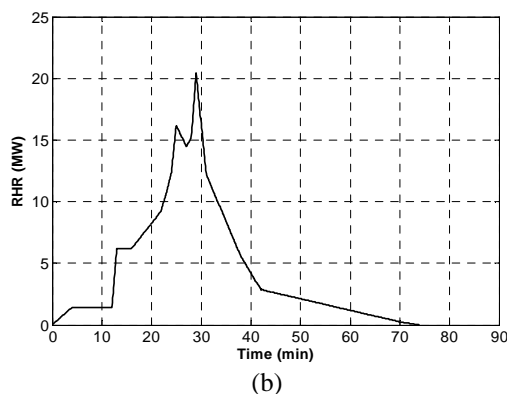
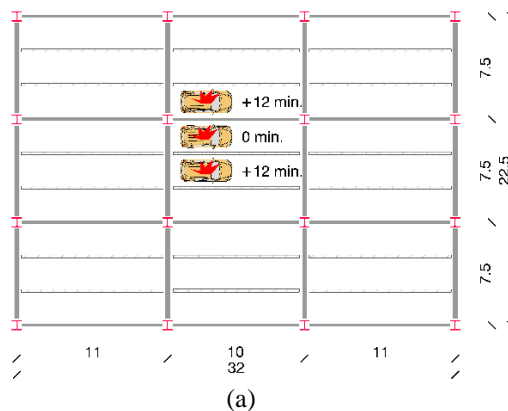


Fig.8 Analyzed fire scenario; a) Position of cars for the reference fire scenario involving three cars, b) Rate of heat release as a function of time by three cars in the reference fire scenario

The concrete slab was modelled by means of shell elements whereas beams were introduced with Bernoulli elements (Fig. 9a). To take into account the column continuity the total height of the superior and inferior floor level columns were modelled in SAFIR. Other indications are reported in [5].

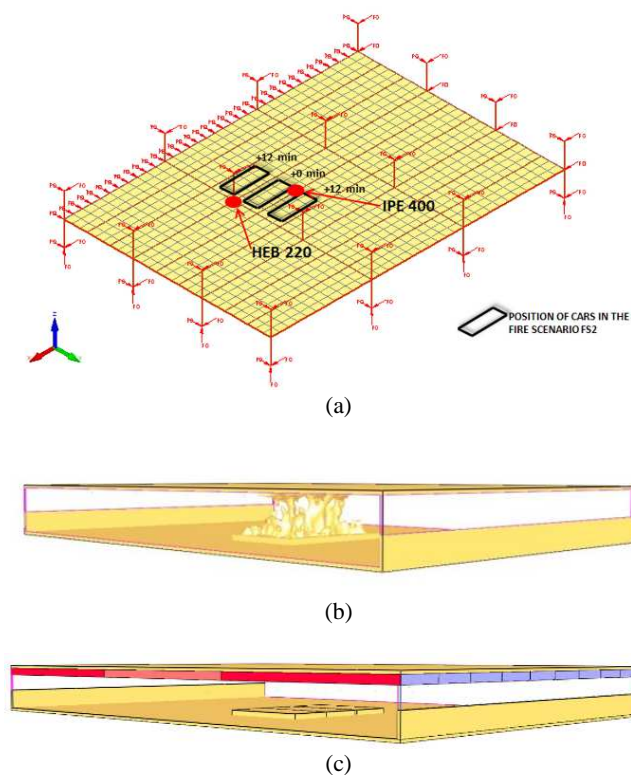


Fig.9 Numerical modelling; a) FE element model of the car park in SAFIR, b) FDS model of the compartment without the inclusion of superior beams c) FDS model of the compartment with the inclusion of superior beams

Initially the application of the simplified localized fire model of Hasemi (performed with the only assistance of a FE software) is introduced. The obtained results would be finally compared with the weak coupling outcomes discussed at the end of the paragraph.

The reference fire scenario was then initially studied by means of the Hasemi fire localized model described in the EN1991-1-2. The Hasemi model is also implemented into SAFIR program that on the base of the cars locations and relative data concerning rate of heat release (RHR) initially performs a thermal analysis on the base of the computed heat flux associated to structural points. The determination of the temperature field into the structural element is then followed by the computation of the mechanical response of the structure. An example of the thermal distribution computed for a secondary beam (IPE400) and the top part of a column (HEB220), whose position is highlighted in Fig.9a, are depicted in Fig.10.

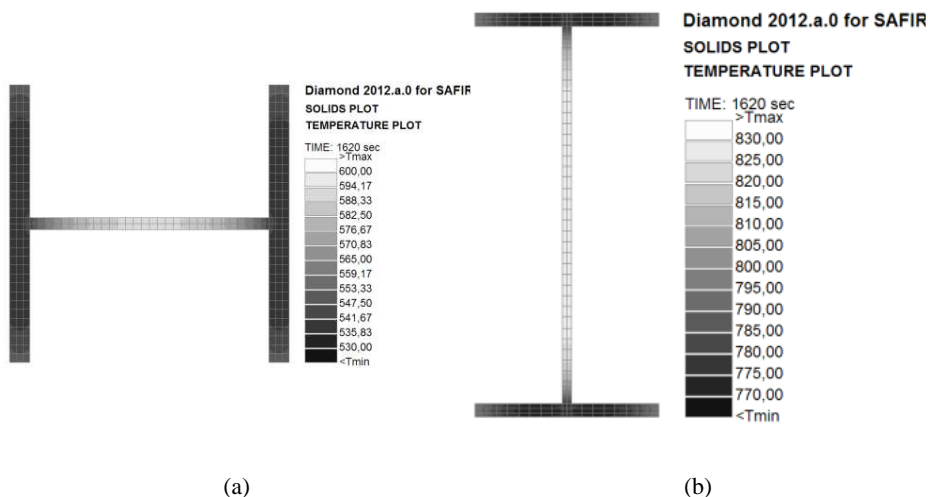


Fig.10 Cross section temperature distribution under a localized fire Hasemi model, measured at collapse (27 min.); a) HEB220 column steel profile, b) IPE400 secondary beam steel profile

The displacement of two significant structural points (secondary beam and top column) signed in Fig.11a are showed in Fig.11b. Results show that the application of the Hasemi localized fire model implicates the structural collapse of the structure (due to column failure) after 27 minutes. The collapse happened when the thermal input connected to the RHR curve depicted in Fig.8b, and the resulting computed heat flux are near to the absolute peak that is attainable from the fire load of three vehicles.

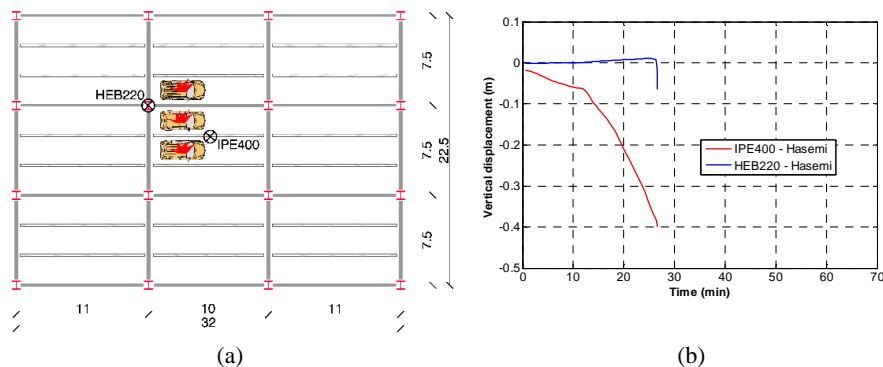


Fig.11 Structural numerical response of the structure under a Hasemi localized fire model; a) Position of structural points in which the displacement is detected, b) Vertical displacements of reference points (top column and secondary beam midspan)

Without enter into the detail of the fire development model performed by means of Fire dynamics Simulator and that is better discussed in [5]; we herein limit to note that a compartment numerical scheme of the car park (Fig. 9b and Fig.9c) was developed in FDS by introducing the correct boundary conditions (external openings), by assigning

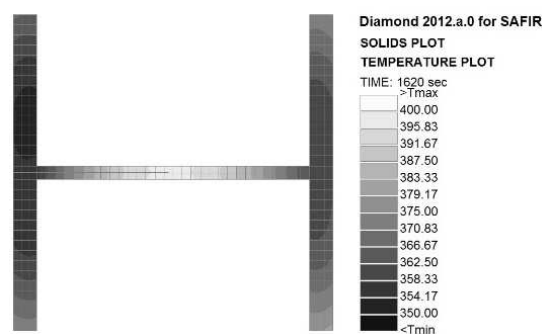
the appropriate thermal properties of the space obstructions and defining the suitable parameters for soot yield (production of smokes) and heat of combustion. A sensitivity mesh analysis was also performed in relation to the severity of the fire and heat release by taking into account that the large eddy simulation technique, adopted by FDS, is based on the assumption that the numerical mesh should be fine enough to allow the formation of eddies that are responsible for the mixing [3].

The burning cars were simulated by assigning to the obstructions located at 30 cm from the floor (wheels level) the RHR curve provided in [11].

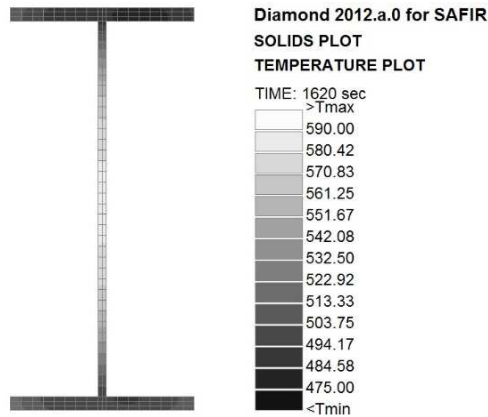
The effect of wind, that could be significant as discussed in Section 5, is not taken into account in the CFD model. The purpose of this work is to perform, under similar conditions, a comparative study between a simplified model based on Hasemi localized fire and the application of an advance methodology based on CFD-FE coupling.

Although the weak coupling approach is based on the hypothesis of neglecting the effect of the structural elements, for this particular structure the ratio between the beam and the ceiling heights suggests to perform a second CFD analysis by introducing the superior beam that could represents a barrier for the hot gases flow. Conservatively these elements were introduced by means of adiabatic surfaces. The deflections of structural beams in the CFD model and their relative impact on gas flow were however not taken into account in the analysis.

Following the standard weak coupling procedure at the end of the CFD analysis a transfer file, containing the information of the fire, is created and transferred to the FE software for the thermal and the final mechanical response. A thermal analysis was then initially performed in SAFIR on the basis of the radiant intensities contained in the CFD file. The integration of the radiant intensities allows to compute the impinging flux that is associated to the structural point. This procedure conduces to the definition of the thermal field of the structural elements that now takes into account also shadow effects and the orientation of the element with referent to fire source. In fact Fig.12a and Fig.12b demonstrate that cross section elements directly exposed to fire are hotter respect to other section elements in shadow.



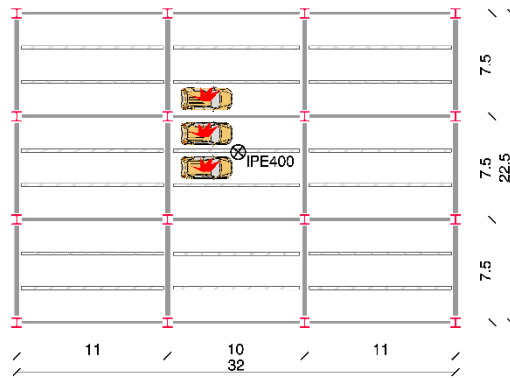
(a)



(b)

Fig.12 Cross section temperature distribution measured at collapse (27 min.); a) HEB220 column steel profile, b) IPE400 secondary beam steel profile

The mechanical analysis is then finally performed on the base of the new temperatures obtained through the coupling between FDS and SAFIR. Fig.13b demonstrates that the value of displacements are significantly inferior respect to the Hasemi analysis outputs. In addition no structural failure occurs during all the duration of the fire.



(a)

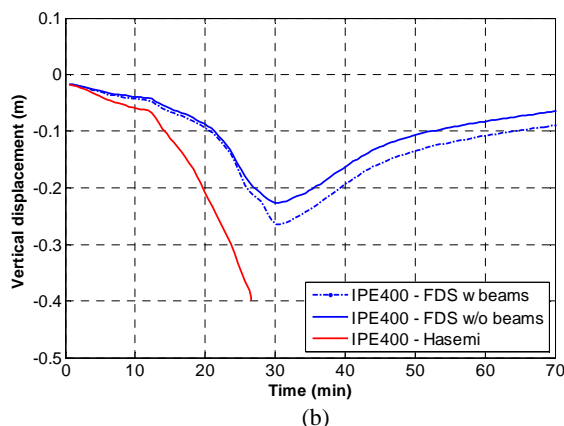


Fig.13 Structural numerical response of the structure under CFD-FE coupling approach; a) Position of structural point in which the displacement is detected b) Vertical displacement of reference point by assuming the FDS model with or without superior beams and comparison with correspondent Hasemi model

The performed comparison has finally demonstrated that different practicable approaches, in the determination of the structural fire resistance, could produce different response of the structure reliability. In the case of the Hasemi model, the simplifications and assumptions that are implicit assumed in the model, and better discussed in [5] (i.e. neglecting of heat absorption by the boundary elements, assumptions of continuously impacting flame model, lack of shadow effects and flux orientation information) produce extremely conservative results. In this context, the importance of advanced numerical tools based on a more refined methods of investigation is demonstrated.

References

- [1] NIST, *Final Report on the Collapse of World Trade Center Building 7, Federal Building and Fire Safety Investigation of the World Trade Center Disaster*, 2008
- [2] Kumar S. et al., *FIRESTRUC - Integrating advanced three-dimensional modelling methodologies for predicting thermo-mechanical behaviour of steel and composite structures subjected to natural fires*, Research Programme of the Research Fund for Coal and Steel, RFS-CR-03030 Final Report, 2006
- [3] McGrattan K. et al., *Fire Dynamics Simulator, User's Guide - Version 5*, NIST
- [4] Franssen J-M., *User's Manual for SAFIR, A computer program for analysis of structures subjected to fire*, University of Liege - Department Argenco Service Structural Engineering.
- [5] Tondini N., Morbioli A., Vassart O., Lechene S., Franssen J-M., An integrated modelling strategy between a CFD and an FE software: methodology and application, *Journal of Structural Fire Engineering* (2016); 7(3).
- [6] European Committee for Standardisation, *Eurocode 3 Design of steel structures - Part 1-1. General rules and rules for buildings*

-
- [7] European Committee for Standardisation, *Eurocode 3 Design of steel structures - Part 1-2. General rules Structural fire design*
- [8] Zhao B., Kruppa J., *Structural behavior of an open car park under real fire scenarios*, Second International Workshop "Structures in fire", Christchurch, 2002.
- [9] Joyeux D. et al, *Demonstration of real fire tests in car parks and high buildings*, Contract n. 7215 PP 025, Final Report, 2001.
- [10] Joyeux D., *Statistiques sur les feux de parking en France*, INC-99/1-DJ/NB, January 1999
- [11] INERIS, *Parcs de Stationnement en Superstructure largement ventiles*, Avis D'expert Sur les Scénarios D'incendie, CTICM, 2001

PAPER 2: An integrated modelling strategy between a CFD and an FE software: methodology and application

The following paper was published in:

Journal of Structural Fire Engineering (EMERALD)

"An integrated modelling strategy between a CFD and an FE software", Journal of Structural Fire Engineering, Vol. 7 Issue 3 pp. 217 – 233 (2016)

<http://dx.doi.org/10.1108/JSFE-09-2016-015>

An integrated modelling strategy between a CFD and an FE software: Methodology and application to compartment fires

Nicola Tondini*, **Andrea Morbioli***, **Olivier Vassart****, **Sullivan Lechêne*****,
Jean-Marc Franssen****

* Department of Civil, Environmental and Mechanical Engineering, University of Trento, Via Mesiano 77, 38123 Trento, Italy
e-mails: nicola.tondini@unitn.it, andrea.morbioli@unitn.it

** R & D Long Product, Arcelormittal, Rue de Luxembourg 66, 4221 Esch-sur-Alzette, Luxembourg
e-mail: olivier.vassart@arcelormittal.com

*** Centre Scientifique et Technique du Bâtiment (CSTB), 84 avenue Jean Jaurès, Champs-sur-Marne, 77447 Marne-la-Vallée Cedex 2 France
e-mail: sullivan.lechene@cstb.fr

**** Structural Engineering Division, University of Liege, Chemin de Chevreuils 1, 4000 Liege, Belgium
e-mail: jm.franssen@ulg.ac.be

Keywords: CFD-FE coupling, weak coupling, open car parks, steel structures, fire behaviour.

Abstract: This paper presents the assumptions and the issues that arise when developing an integrated modelling methodology between a Computational Fluid Dynamics (CFD) software applied to compartment fires and a Finite Element (FE) software applied to structural systems. Particular emphasis is given to the weak coupling approach developed between the CFD code Fire Dynamics Simulator (FDS) and the FE software SAFIR. Then, to show the potential benefits of such a methodology, a multi-storey steel-concrete composite open car park was considered. Thus, a typical design approach employing the Hasemi model is compared with a more advanced analysis that relies on the proposed FDS-SAFIR coupling. Results show that the FDS-SAFIR coupling allows overcoming shortcomings of simplified models by performing the thermal analysis in the structural elements based on more advanced modelling of the fire development, whereas it appears that the Hasemi model is more conservative in terms of thermal action.

1 INTRODUCTION

To obtain the thermo-mechanical response of structures exposed to fire, integrated modelling methodologies applied to compartment fires would represent a powerful tool to widen the application field of structural fire safety engineering by overcoming limitations associated with simplified procedures. For instance, the simplified Hasemi localised fire model [1] and incorporated in EN1991-1-2 [2] is suitable for analysing the fire performance of open car parks. It provides the heat flux at the ceiling level; thus, being appropriate for beams and slab. However, simplified models that provide information about the thermal action along the height of a column owing to localised fires are not yet available and cautionary assumptions are usually taken. As a result, this may lead to a conservative fire design. To overcome this issue, Computational Fluid Dynamics (CFD) advanced fire models that are capable of an accurate modelling, both in time and in space, of the fire development represent a tempting alternative. The exploitation of integrated modelling strategies based on the coupling between CFD and FE programs are already used in medicine, e.g. for modelling the blood flow in arteries [3]. However, in the fire engineering field, very few applications are available and the ones that have been developed are often limited to specific software pairs [4]. The Research Fund of Coal and Steel (RFCS) project called FIRESTRUCT [5] dealt with this issue by studying different coupling approaches and employing different software. In this paper, the weak coupling approach developed between the CFD software FDS and the FE software SAFIR is described, but it has to be underlined that the methodology could be used with any CFD and any FE software. The work is finally enriched by reporting on the comparison between the fire performance of a steel-concrete composite open car park analysed by applying first the simplified Hasemi model and then the FDS-SAFIR integrated methodology.

2 OVERVIEW ON INTEGRATED CFD-FE METHODOLOGY

2.1 Compartment fires: problem definition

Three problems have to be solved when modelling the behaviour of a structure subjected to a compartment fire, each of them being governed by a different physical phenomenon and, hence, by different equations: 1) temperature development in the compartment; 2) thermal response of the structure and 3) mechanical response of the structure. The fire development analysis yields the temperatures of gases and the radiative and mass flows in the compartment. By means of the thermal analysis, the temperatures in the structural elements are obtained. The mechanical response provides the behaviour of the structural system, i.e. stresses, deflections etc. Several differences distinguish these three processes. First, the spatial scale of the thermal analysis in the structure is an order of magnitude smaller than the spatial scale used for the development of the compartment temperature and the mechanical response. Second, the time scale may be different to solve the problem within CFD and FE analysis. Third, as regards the temperature development in the compartment and the mechanical

response a 3D analysis is generally required, whereas for the thermal analysis a 2D analysis is usually sufficient. Thus, some issues arise when an integrated modelling methodology CFD-FE is to be used to tackle the whole problem. It is natural to assign the task of performing the analysis of the compartment fire development to the CFD model and the mechanical response to the FE model, but it is not so straightforward to decide where to carry out the thermal analysis in the structural elements. Both software may be exploited to fulfil the task. The advantages to perform the thermal analysis in the CFD model are, first, to get direct information about the temperature development in the compartment and, second, to take into account the energy absorbed by the structure. On the other hand, if the thermal analysis in the structure is carried out in the FE model, all necessary data are directly available by the FE code to determine the mechanical response. Moreover, the choice also depends on how the CFD and the FE codes can accurately solve the heat conduction equation with respect to the particular problem under study. Whatever the choice, the difficulties arise when data have to be exchanged between the two software, because of different scales in space and time. Moreover, if the thermal analysis is performed in the CFD software, the compartment model must include the structure as well. The latter aspect is not desirable, as described later on.

2.2 Levels of coupling

From the description of the problem, it is clear that coupling CFD to FE is far from straightforward and that the selected level of coupling influences the complexity of the model. In reality, all three problems are mutually coupled - full coupling or two-way coupling - as shown in Fig. 1. Table 1 reports on the main phenomena involved in a compartment fire along with their mutual interactions and it intends to highlight the large amount of interactions that are extremely difficult to deal comprehensively with [5].

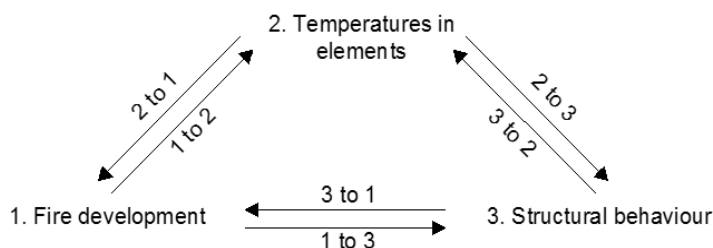


Fig. 1: Full coupling between the main phenomena involved in a compartment fire.

Table 1: Mutual interactions between main phenomena involved in a compartment fire.

PHENOMENON	COUPLING					
	1 to 2	2 to 3	3 to 1	1 to 3	3 to 2	2 to 1
FIRE						
Convection and radiation to structural elements	x					
VELOCITY OF GASES						
Convection factors	x					
Dynamic pressure on walls, windows				x		
PRESSURE						
Static pressure on walls, windows				x		
TEMPERATURE IN MATERIALS						
Thermal elongation of elements		x				
Degradation of mechanical properties		x				
Absorption of energy from the compartment						x
PLASTICITY AND CRACKING IN ELEMENTS						
Generation of heat or heat leakage			x		x	
Modification of material thermal properties					x	
DISPLACEMENTS IN ELEMENTS						
Modification of the gas flow			x			
Modification of the element thermal exposure					x	

The implementation of full coupling allows taking into account all phenomena and it guarantees a general field of application as well as a solution that tends to be exact. An example of full coupling is the interface developed between VESTA, a CFD software, and DIANA, an FE software developed by TNO in the Netherlands [5]. However, an integrated methodology that relies on full coupling is very complex to achieve. The first reason lies in various uncertainties that question the so-called exactness of the method. For instance, heat leakage through cracks in concrete (3 to 1 and 3 to 2) or gypsum plaster board enclosures are still very difficult to quantify because they do not follow deterministic rules. Moreover, from a programming point of view, the code of the selected CFD software and the code of the FE program have to be modified so that they can communicate for the exchange of data, but it means that in most cases the integrated methodology will not work if another CFD or another FE software is used. This is a clear drawback in terms of versatility and flexibility. Furthermore, for each simulation, a CFD specialist as well as an FE specialist are required since the two models cannot be run independently. Other typical issues that may occur in the design practice are related to possible modifications that the structure undergoes during the construction process as well as modifications of the structure that have to be applied because of an unsatisfactory behaviour in terms of fire safety requirements. Since the structural elements must be included in the CFD model, any changes in the structural system imply that the whole analysis must be re-run, entailing large time-consuming analyses. From these considerations, a simplified approach, the so-called weak coupling, is proposed to overcome the major aforementioned issues with the aim to be applicable to a wide number of likely-to-occur scenarios in compartment fires.

3 PROPOSED WEAK COUPLING METHODOLOGY

3.1 Assumptions and general remarks

In the proposed weak coupling (or one-way) approach, the mutual interactions are discarded, as illustrated in Fig. 2. For weak coupling we mean that: i) the degree of interdependence, from a computer programming point of view, between the CFD software and the FE software is low; ii) the multi physics problem is treated through sequential analyses, i.e. the fire development analysis is performed first, then the thermal analysis in the structural elements and finally the mechanical analysis of the structure that does not consequently influence the temperature field in the structural elements. As a result, the CFD software models the fire development, while the FE program performs the thermal and the mechanical analyses. The fire development is calculated independently of the thermal response in the linear elements of the structure such as steel columns, beams or truss girders. If part of the structure is made of planar elements that also constitute boundaries of the compartment such as concrete walls or slabs, they must be modelled, perhaps with some degrees of approximation [6], in the fire development analysis. The FE software will nevertheless compute the detailed temperature field in these structural elements subsequently. Therefore, if p variations

of the structure must be evaluated under q fire scenarios, only q CFD analyses have to be performed, compared to $p \cdot q$ coupled analyses in a full coupling approach.

In this strategy, the thermal response of the structure represents the input of the mechanical analysis. Hence, it can be performed first, over the whole time domain, and then the resulting data are transferred at the beginning of the mechanical analysis, which is performed subsequently.

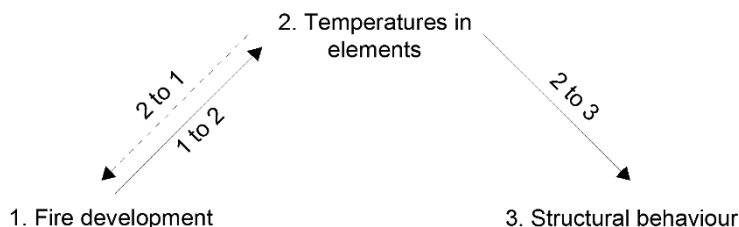


Fig. 2: Weak coupling between the main phenomena involved in a compartment fire.

Nonetheless, these simplifications imply some limitations:

i) the dimensions of the structural elements and their displacements perpendicular to their longitudinal axis shall be small compared to the dimensions of the compartment in order not to significantly influence the temperatures and the air flow around the elements. According to this assumption, a series of 2D thermal analyses rather than a unique 3D thermal analysis is made on the structural elements because the transverse dimension of the section of the elements is small with respect to the longitudinal dimensions. For instance, a 1 m x 1 m concrete columns in a 100 m² compartment should clearly be considered in the CFD model. Very flexible structures that are sensitive to air pressure variation are also not suitable for such an integrated modelling methodology because the effects of air pressure variation on the displacements of the structure cannot be neglected. Floor systems designed according to the tensile membrane action also exhibit very large displacements during the fire and may not comply with this requirement if the floor to ceiling distance is small compared to the displacement.

ii) It is possible, for each 2D thermal analysis, to consider the boundary conditions at the surface of the section at the same point, namely the point of the section located on the node line of the beam element; for example the centre of gravity of the section. The influence of the distance from the node line of the section to the border of the section is neglected. This is consistent with the fact that the structure is not present in the CFD analysis because the size of the section perpendicular to the longitudinal axis is negligible with respect to the size of the compartment; the distance from the centre of the section to the border (approximately $\frac{1}{2}$ of the size of the section) is then also negligible.

iii) Generally, in the CFD model the dimensions of a rectangular compartment

correspond to the clear distances between opposite walls. However, in the FE model a slab is generally modelled in correspondence to its centreline as illustrated in Fig. 3. Thus, the slab would fall outside the CFD domain and assumptions have to be made to determine thermal information at the slab centreline.

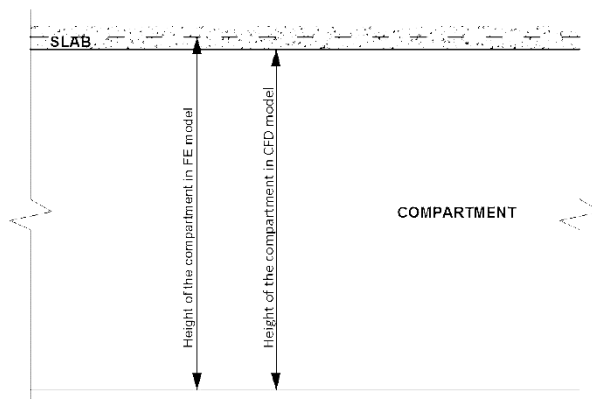


Fig. 3: Different compartment dimensions for the CFD and the FE model.

iv) As the structure is not included in the CFD model, the effect of shielding from any structural elements on others cannot be detected. For example, if a series of closely-spaced columns one behind the other is impinged by a radiant flux with direction parallel to the column series, the magnitude of the flux received by each column will only depend on the distance of each single column from the fire source and no effects of shielding will be taken into account on the columns behind the first one.

v) Irrigated structures in which water is circulating to keep the temperature of the structure within acceptable limits cannot be neglected because they may contribute in evacuating important amount of energy from the compartment.

This procedure is thus particularly well adapted for metallic structures made of relatively thin members (frame, truss girders) and located in large compartments (railway or airport entrance halls, exhibition halls) where a localised fire is developing and simplified thermal models, such as those proposed in EN1991-1-2 [2], cannot be employed because the geometry of the compartment is too complex or the position of the structure in the compartment with respect to the position of the fire is not within the field of application of a simplified model.

3.2 How it works

In this section, the practical issues that have to be solved when implementing such an approach are presented. The programs used in this paper to illustrate the proposed integrated methodology are FDS [7] and SAFIR [8]. The main steps needed to couple CFD and FE models are:

- 1) at the end of the CFD analysis, a transfer file containing all information regarding

the state in the compartment, i.e. temperature of gas and radiant intensities from various directions, is produced. These quantities can be provided at each grid point of the CFD model (the grid that was required to allow a precise determination of the solution) or instead at grid points representing only the part of the compartment where the structure to be analysed is located. Convection factors are also transferred but a uniform value introduced by the user before performing the thermal analysis is instead used; typically, a value of $35 \text{ W/m}^2\text{K}$ as suggested in EN1991-1-2 [2].

The format of the transfer file should be as standardised as possible so that in a future perspective it could be used for any choice of CFD and FE software. Hence, type of file (e.g. ASCII), syntax, type of reference system, type and format of numbers, presence of blank lines etc. have to be clearly stated. Such a format has been proposed within the FIRESTRUCT project and can be obtained from the authors. Radiant intensities from different directions are preferred to impinging radiant fluxes on predefined surfaces because the structural elements are not included in the CFD model and thus no information is available at that stage about the shape of the cross sections. The fluxes at the surface of the structural elements will be computed within the FE software by integrating the radiant intensities, which allows taking into account possible shadow effects in concave sections.

2) A 3D Cartesian spatial interpolation is needed because the points of the structure where the information is needed (called here “the structural points”) generally do not coincide with the points of the CFD grid where the information is provided. If any structural points fall outside the CFD domain for the reason described in Section 3.1, they are moved to the closest boundary of the CFD domain where the Cartesian interpolation can be made, namely the boundary corresponding to the centre of the outermost cells because FDS provides the information at the centre of cells (see Fig. 4). A trilinear interpolation algorithm was successfully implemented in SAFIR to fulfill the 3D Cartesian interpolation.

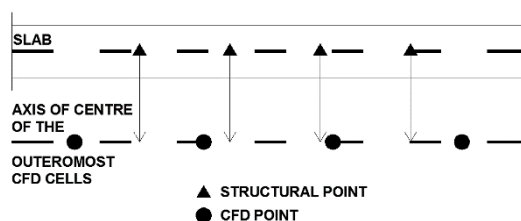


Fig. 4: Case of structural points outside the CFD domain.

3) An interpolation in the time domain is also necessary because the time steps of the CFD analysis and the time steps of the thermal analysis may not be the same. In this case, a simple linear interpolation was exploited.

4) To get the impinging fluxes q on the surface of the structural elements a spherical numerical integration of radiant intensities I has to be performed. A numerical integration can be performed according to Eq (1).

$$q = \sum_{i=1}^n I_i \cos \theta_i \omega_i \quad (1)$$

where n is the number of intensities considered for the integration, ω_i is the solid angle associated to the direction i , θ_i is the angle between the direction of the radiant intensity i and the normal to the surface while I_i is the radiant intensity associated with the i -direction.

The directions of the intensities which are required to perform the spherical integration are generally not the directions in which the intensities are given by the CFD analysis. This is particularly the case if the structural elements are not parallel to the axes of the system of coordinates used in the CFD analysis (e.g. for diagonals in a truss girder). A spherical interpolation is thus performed to obtain the radiant intensities in the directions required by the numerical integration. Rotations of local axes are required to find the surface system of coordinates taking into account the direction of the longitudinal axis and the shape of the cross-section.

It is essential that the type of mesh and type of system of coordinates used in the CFD analysis (step 1) be clearly defined and taken into account in steps 2 and 4. The format of the transfer file is based on the assumption of a structured rectangular mesh in a dextrorsum Cartesian system of coordinates. The position of the origin of the system of coordinates and the directions of the X, Y and Z axes as well as the direction of gravity shall be common in the CFD and in the FE analyses.

4 APPLICATION OF THE PROPOSED METHODOLOGY TO A STRUCTURAL SYSTEM

To show the potential benefits of such a methodology, the fire performance analysis of a multi-storey steel-concrete composite open car park designed according to the Eurocodes for which simplified localised fire models are in their range of applicability is presented. Thus, a typical design approach that employs the Hasemi model is compared with a more advanced analysis that relies on the proposed FDS-SAFIR coupling.

4.1 Description of the open car park

The structure is a four-storey steel-concrete composite open car park. The elevation and plan layouts are illustrated in Fig. 5a and 5b. The steel-framed structure was designed according to the Eurocodes and was made of steel grade S275, of a composite slab of concrete class C25/30 and profiled steel sheets (see Fig. 5c), of secondary beams IPE400 and IPE450, of primary beams IPE500 and IPE400 and of steel columns HEB200, HEB220 and HEB240. Moreover, the structure was assumed braced. An adequate degree of openings along the perimeter was allowed for the car park to be

classified as open. Both primary and secondary beams were considered as simply supported whilst columns were continuous along their entire height. No fire protection was applied to the structure.

OPEN CAR PARK - FLOOR PLAN TYPE

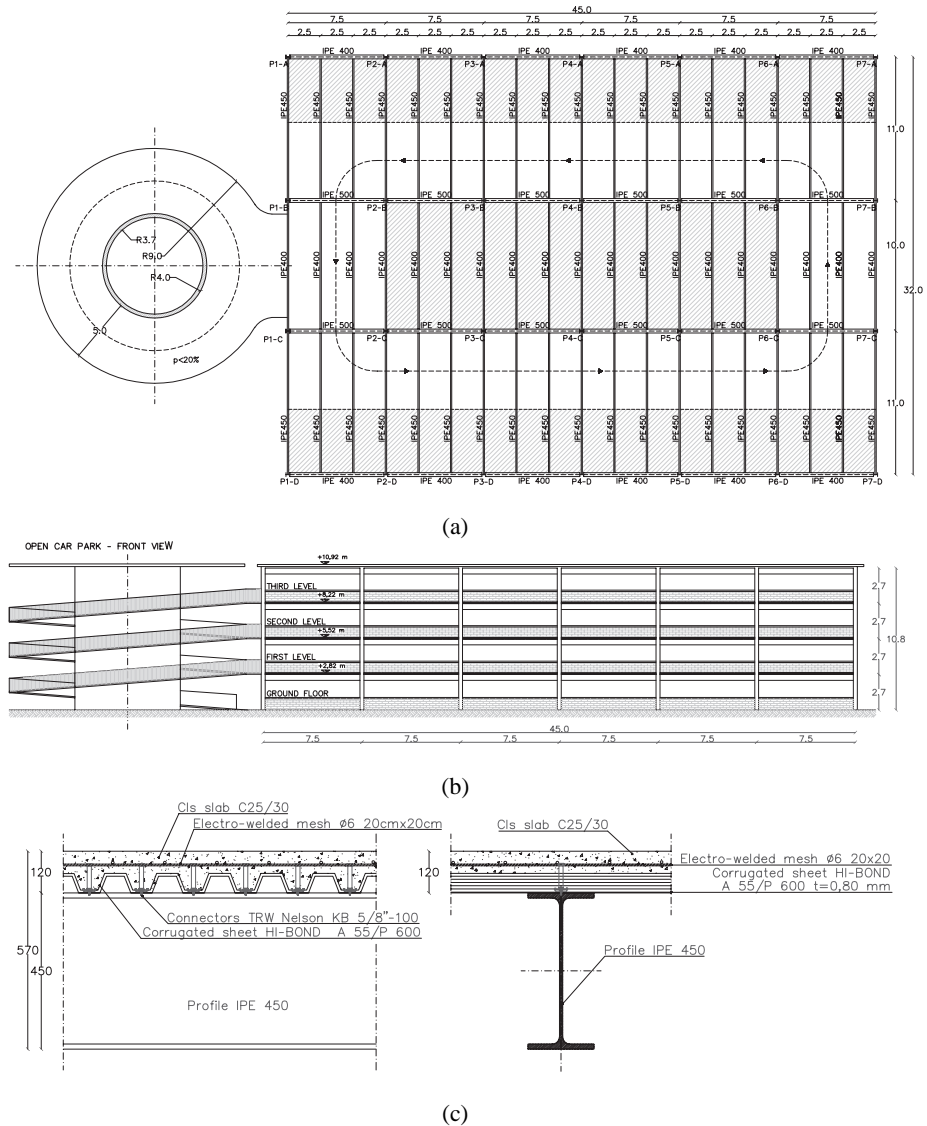
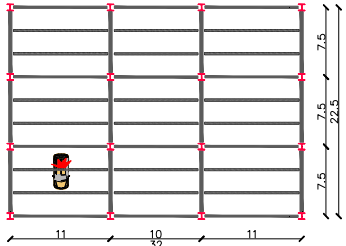
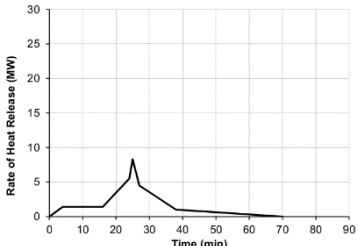
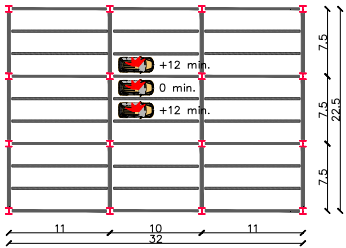
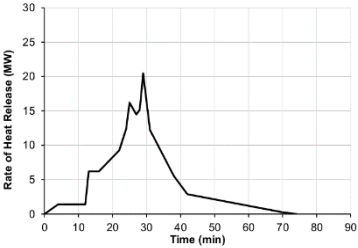
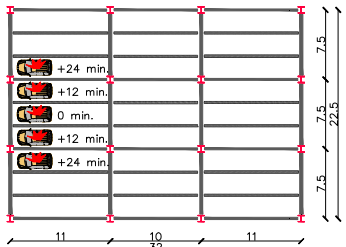
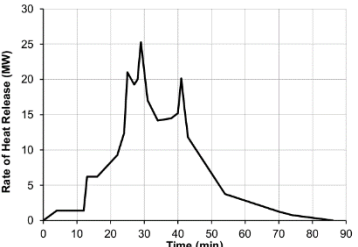


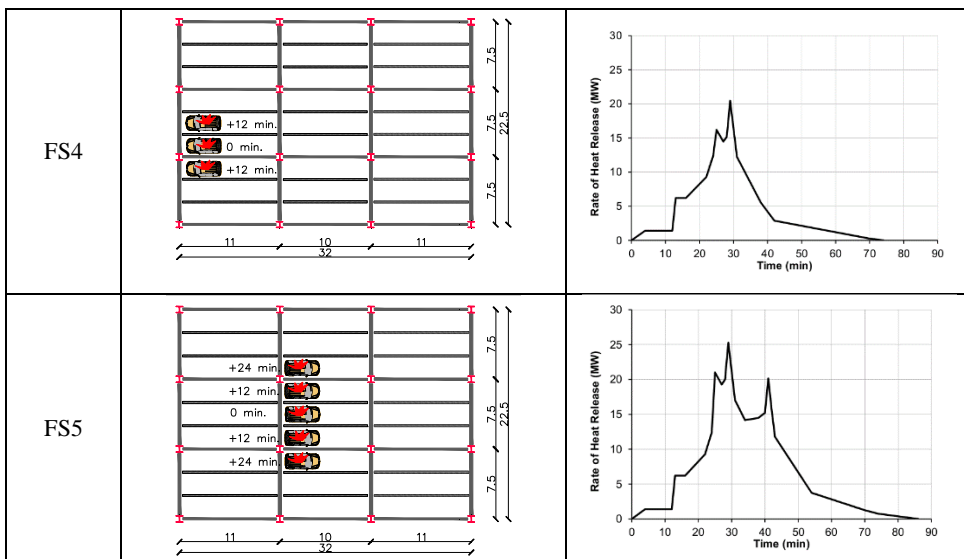
Fig. 5: Geometric layout of the open car park: a) plan view, dimensions in m; b) elevation view, dimensions in m; c) detail of the composite slab, dimensions in mm.

4.2 Definition of fire scenarios

Different fire scenarios with a variable number of vehicles by assuming Rate of Heat Release (RHR) curves representative of burning cars of Class 3 were considered [9]. By taking into account the car park layout, the analysed fire scenarios are shown in Table 2. When multiple cars were involved into a fire, a time shift ignition between nearby cars was envisaged as observed in real car fires. As a result, the ignition of cars just next to the first that ignites the fire was delayed of 12 min. Moreover, it is worth pointing out that the worst fire scenario for the column, i.e. four burning cars around it, was not considered because of the car park layout. In fact, the likelihood of occurrence of this scenario is very low owing to the absence of face-to-face parking spots around the column, see Fig. 5a. Then, based on the definition of the fire scenarios the two approaches, i.e. Hasemi model and FDS-SAFIR coupling, were employed.

Table 2: Fire scenarios

Fire scenario	Position of vehicles in half car park	Characteristics of the fire (RHR curve)
FS1		
FS2		
FS3		



4.3 3D Finite element model

To evaluate the fire performance of the open car park, a 3D FE model was developed in SAFIR [8]. Since the deterministic fire scenarios for car parks, as provided in [9], are localised fires, only a small part of the car park is significantly influenced by each fire scenario. Thus, half of it was actually modelled and boundary conditions that guaranteed slab continuity were applied. Moreover, it is very unlikely that a fire could spread to all floors; consequently, only fire scenarios acting at one level of the car park were modelled by relying on a good compartmentalization of the slab.

The slab was modelled by means of shell elements, whereas beams were modelled with Bernoulli beam elements. To take into account the column continuity, the columns of the floor above were also included into the model, as illustrated in Fig. 6, and they were kept at ambient temperature. Relevant vertical loads in the fire situation [10] were applied to the structure and they comprised dead load, self-weight and live load; the latter equal to 2.5 kN/m^2 [11]. In Fig. 6 two critical sections are highlighted: i) the top section of the nearest column to the fire (point HEB220); and the section of the secondary beam that under the critical fire scenario experiences the largest vertical displacement (point IPE400). In the remainder of the article, comparisons were made at such points.

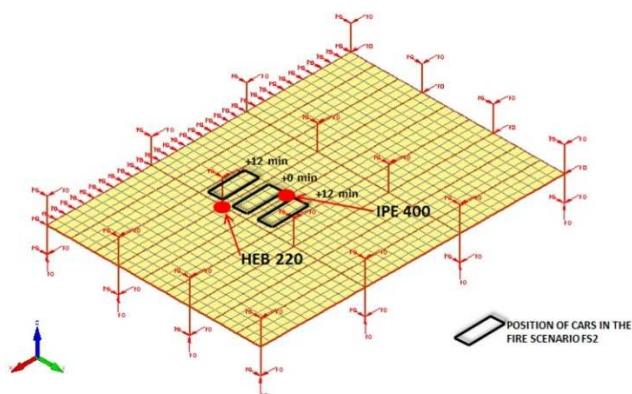


Fig. 6: 3D finite element model of half car park and positions of the cars in FS2.

4.4 Fire analysis of the car park with the Hasemi model

The study of the fire performance of the car park was initially carried out by analysing it under all fire scenarios shown in Table 5 by means of the Hasemi model. This allowed the identification of the most critical one that was then analysed through the application of the FDS-SAFIR integrated strategy. This way of proceeding was pursued because the FDS-SAFIR coupling is more computationally demanding and time consuming. Furthermore, SAFIR already implements the Hasemi model; thus it results quite handy to perform such an analysis.

4.4.1 Thermal analysis

Thermal analyses were conducted on each structural element: slab, columns and beams. Primary beams were considered exposed on 3 sides with the slab on top of them whilst secondary beams were exposed on 4 sides since more than 15% of the top flange was not covered by the steel sheet of the slab [12]. The slab on the top of the primary beams was used in thermal analyses for reproducing the non-uniform temperature distribution in the section. However, in the mechanical analyses it was not effective because the slab was already modelled by means of shell elements. In the absence of a simplified model, a cautious thermal action was applied along the entire height of the column and equal to the heat flux determined at its summit with the Hasemi model. As a result, the temperature distribution at failure in the HEB220 column top section and in the critical section of the IPE400 secondary beam owing to FS2, as depicted in Fig. 6, is shown in Fig. 7.

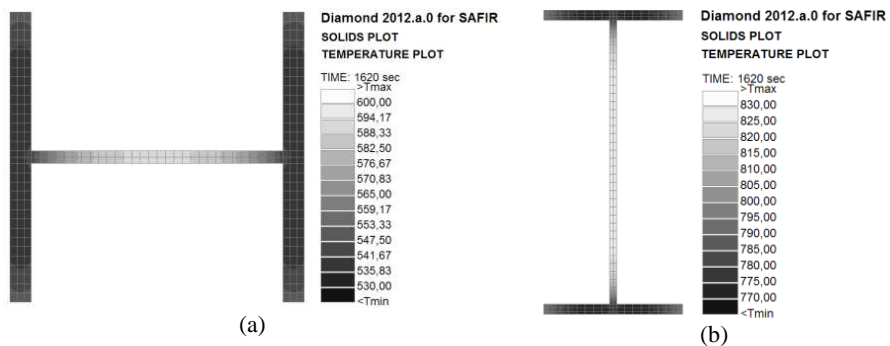
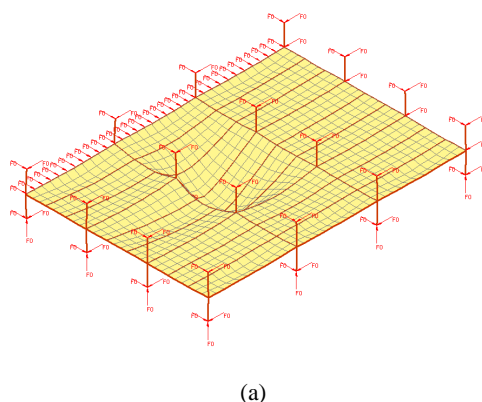


Fig. 7: Hasemi model – FS2: temperature distribution in significant sections at failure ($t = 27$ min): a) at the top of the column (HEB220); b) in the secondary beam (IPE400).

4.4.2 Mechanical analysis

From the results of the mechanical analyses performed for each fire scenario, it was found out that FS2 was the most critical one as entailed the collapse of the HEB220 column directly located next to the burning cars after 27 min of fire exposure. FS3 also caused structural failure but later in the analysis because of a larger time shift in the ignition of cars next to the column. The deformed shape and the vertical displacement of the structure at collapse ($t = 27$ min) are illustrated in Fig. 8a and 8b. Fig. 8c shows the evolution of the vertical displacements at the two critical sections highlighted in Fig. 6.



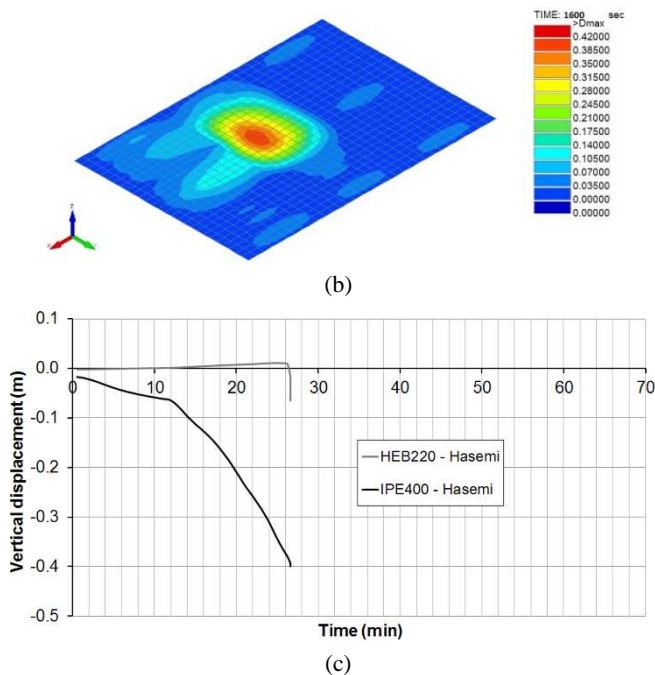


Fig. 8: Hasemi model – FS2: a) deformed shape at failure amplified by a factor of 10; b) vertical displacements (in metres) at failure; c) evolution of the vertical displacements at the critical sections of the HEB220 column and of the IPE400 secondary beam.

4.5 Fire analysis of the car park with the FDS-SAFIR coupling approach

4.5.1 Modelling of the fire development

To minimise border effects with respect to the smoke flow, more than half of the car park was modelled in FDS and the fire development under the most critical scenario (FS2) was analysed. According to the proposed strategy, no structural elements across the compartment were included in the CFD model, see Fig. 9a. Thus, the influence of beams and columns on the smoke flow was initially neglected. The boundary conditions were consistently modelled with physical parameters that describe the thermal properties of the concrete slab, floor and parapets [13]. The burning cars were simulated by assigning to the obstructions located at 30 cm from the floor, i.e. the wheel mean height, the relevant Class 3 car RHR curve according to the INERIS document [9]. The default fire parameters according to FDS version 5.5.3 [7] were used. However, to better represent the real properties of a car fire, a value of soot yield equal to 0.22 was chosen [14] and a value of heat of combustion equal to 44.4 MJ/kg, typical of gasoline, was selected. The mesh of the compartment was selected by means of a sensitivity analysis performed to provide an adequate grid capable of accurately modelling the characteristics of the localised fire. Fig. 9b shows the temperature evolution with

different cell grid dimensions at the ceiling level above the 3-car fire with slightly time-modified RHR to reach the peak in a shorter time. The difference in temperature is very small between the two grids; thus, a 15 cm x 15 cm x 15 cm mesh grid was deemed adequate to model such a localised fire. Furthermore, the appropriateness of this mesh was also verified according to Ma and Quintiere [15] and to the guidelines included in the FDS user manual [7] that confirmed its adequacy. Possible wind effects were not taken into account inside the CFD model.

At the end of the analysis, the transfer file with the relevant information about the fire development was created to be exploited by SAFIR for the thermal analysis.

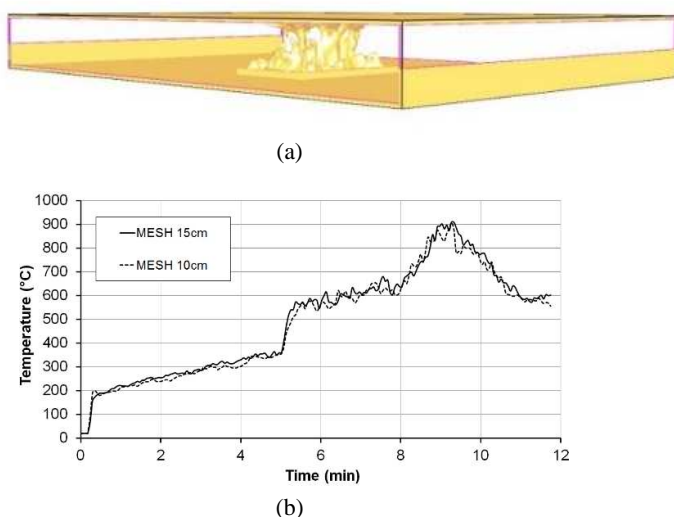


Fig. 9: FDS-SAFIR – FS2: a) fire development modelling; b) temperature development at the ceiling level with different mesh grids owing to a Class 3 3-car time-shifted fire.

For this structure, the ratio between the beam and the ceiling heights suggested an additional analysis that included the beams in the CFD model because they likely act as a barrier that traps the hot gases to some extent influencing the smoke flow. Hence, the effect of modelling the beams in the CFD model was analysed. They were approximately and conservatively included into the CFD model by means of adiabatic surfaces of the same height of the actual beams, as shown in Fig. 10a. Moreover, Fig. 10a also provides indication of the obstruction extent of the beams in relation to the height of the compartment. Then, the fire development analysis was re-run and the results of the two analyses are compared in Fig. 10b-10d. In greater detail, the temperature distribution at the ceiling level in the compartment after 30 min and the gas temperature evolution around the top of the nearest column to the fire, i.e. HEB220 in Fig. 6, are shown. As expected, the influence of the beams on the smoke flow exists

and locally the increase in gas temperature is not negligible. Therefore, for this structural typology the influence of beams on the CFD modelling has to be always carefully checked. Nonetheless, it will be shown that this local effect on the global mechanical behaviour is small.

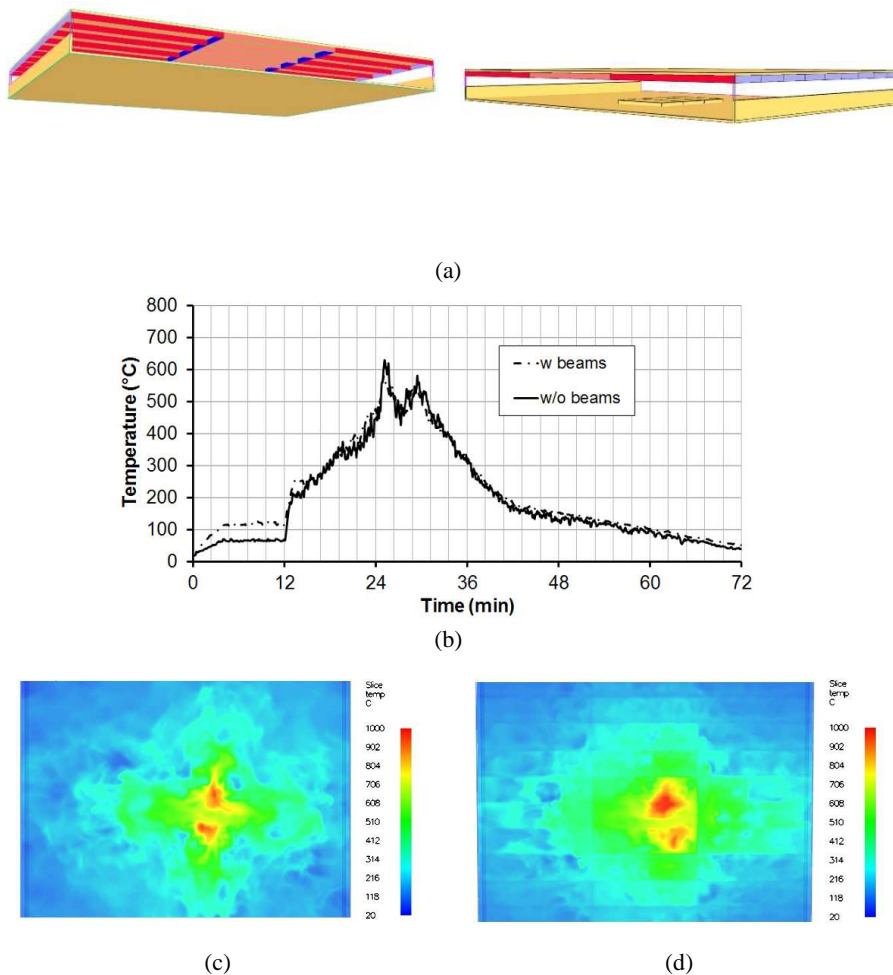


Fig. 10: FDS-SAFIR – FS2: a) Compartment modelling with beams included in the CFD model; b) gas temperature evolution around the top of the HEB220 column without (w/o) and with (w) beams included in the CFD model; c) gas temperature distribution at ceiling level at 30 min without including beams; d) gas temperature distribution at the ceiling level at 30 min including beams.

4.5.2 Thermal analysis

To perform the thermal analyses in each section, the data obtained from the CFD analyses were then exploited by SAFIR. The results at the most critical sections in the case without beams included in the CFD model are shown in Fig. 11 and 12a. From Fig. 12a, it is possible to note that the temperatures obtained from the Hasemi model are much higher than those obtained from CFD data. The main reasons of this marked difference are the following: 1) the Hasemi model has been derived by means of experimental tests performed with a ceiling made of perlite boards, i.e. an insulating material, so that heat absorption through the ceiling was negligible whereas the concrete slab behaves as a heat sink that causes a decrease in gas temperature at the ceiling level; 2) the Hasemi model implicitly assumes that the flame impacts the ceiling but as observed in the CFD analysis and as estimated by the Heskestad model [2], it only occurs for about one sixth of the fire duration; 3) the heat flux computed by means of the Hasemi model was applied to structural sections without considering any shadow effects and flux orientation with respect to the position of the structural elements. The ability of the proposed methodology of taking into account flux orientation and shadow effects is clearly visible in Fig. 11.

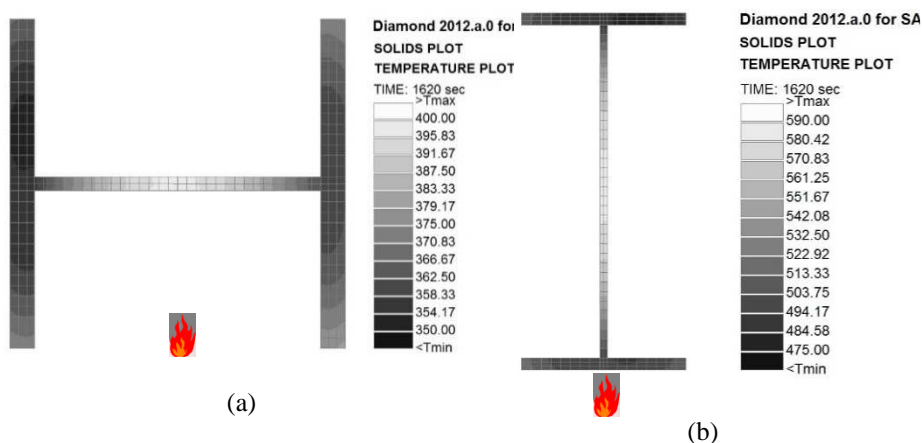
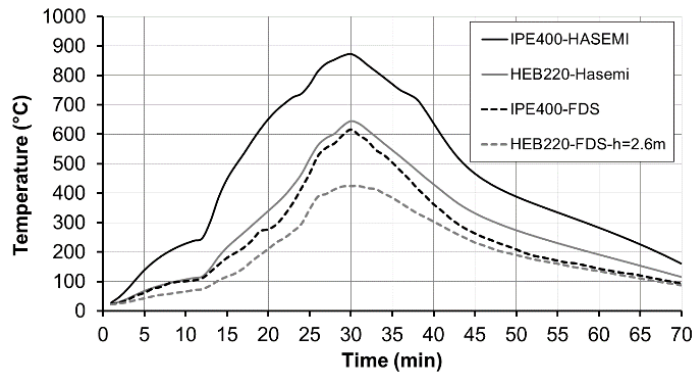


Fig. 11: FDS-SAFIR – FS2. CFD model w/o beams; temperature distribution at 27 min in the critical section: a) of the column (HEB220) and b) of the secondary beam (IPE400).

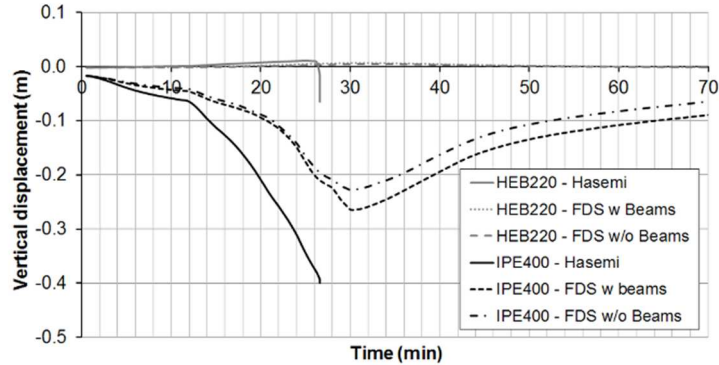
4.5.3 Mechanical analysis

The comparison of the mechanical analyses (Fig. 12b) highlights that no failure occurred when the integrated strategy FDS-SAFIR was applied owing to a more accurate analysis of the fire development that resulted in lower thermal actions on

structural elements, above all along the columns. The presence of the beams in the CFD model influences the smoke flow; however, they did not affect the global behaviour to a large extent, as illustrated in Fig. 12b. For example, the difference in terms of vertical displacement experienced by the column between the cases “FDS w/o beams” and “FDS w beams” is very small (Fig. 12b). Note a sensitive reduction of vertical displacement at 27 min, as illustrated in Fig. 12c and 12d, with respect to the Hasemi model analysis (Fig. 8a and 8b).



(a)



(b)

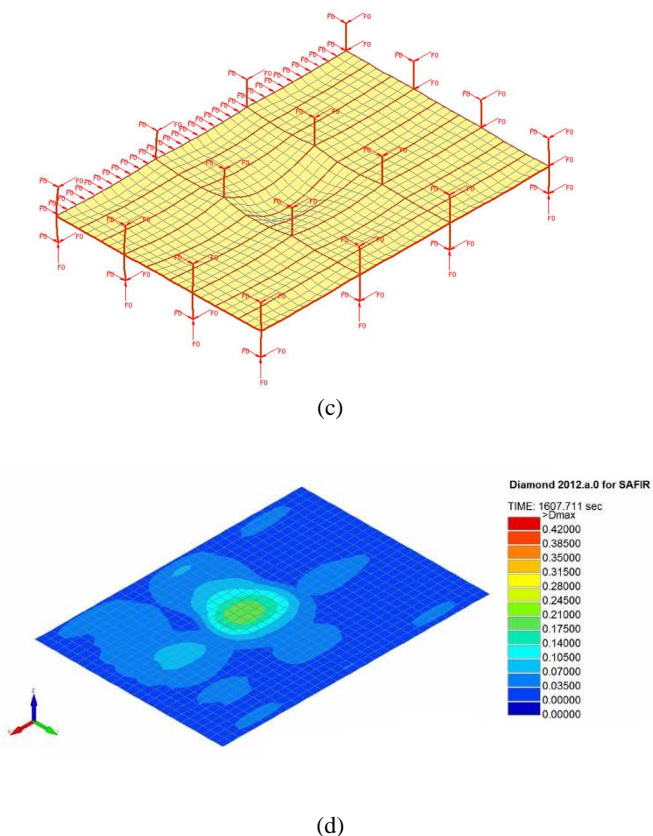


Fig. 12: FDS-SAFIR – FS2. a) Comparison of the temperature evolution in the web of critical sections of the column (HEB220) and of the secondary beam (IPE400), CFD model w/o beams; b) comparison of the mechanical response of the critical sections of the column (HEB220) and of the secondary beam (IPE400); c) deformed shape at 27 min amplified by a factor of 10; d) vertical displacements (in metres) at 27 min.

5. CONCLUSIONS

This article presented an integrated modelling strategy between a CFD software and an FE software that has been recently applied to FDS and SAFIR. Although it implies some simplifications, the proposed weak coupling approach is more desirable for practical applications with respect to a full coupling approach because it can cover a wide number of likely-to-occur scenarios in compartment fires by being at the same time less computational demanding and handier to use. The potential benefit of the integrated methodology was shown when applied to a steel-concrete composite open car park and then compared with the simplified Hasemi model. In fact, the fire performance analysis of the open car park highlighted that the FDS-SAFIR methodology allows overcoming shortcomings of simplified models by performing the thermal analysis in the structural elements based on more advanced modelling of the

fire development, provided that a careful assessment of all assumptions be performed. Conversely, the Hasemi model revealed to be more conservative in terms of thermal action. In particular, its application entailed the collapse of the structure under study after 27 min, whereas by means of the proposed integrated modelling FDS-SAFIR the structure survived for the whole duration of the most critical fire scenario.

References

- [1] Pchelintsev, A., Hasemi, Y., Wakamatsu, T., Yokobayashi, Y., Experimental and numerical study on the behavior of a steel beam under ceiling exposed to a localized fire, Fire Safety Science – Proceedings of the fifth International Symposium, Melbourne, Australia, 3-7 March, 1997, 1153-1164.
- [2] EN 1991-1-2, Eurocode 1: Actions on structures – Part 1-2: General actions – Actions on structures exposed to fire, European Standard, CEN, 2004.
- [3] Zhao, S.Z., Xu, X.Y. and Collins, M.W, The numerical analysis of fluid-solid interactions for blood flow in arterial structures Part 2: Development of coupled fluid-solid algorithms, Proceedings of the Institution of Mechanical Engineers, Part H: Journal of Engineering in Medicine, 1998, 212(4), 241-252.
- [4] Fellinger, J., Kenyon, Y., Breunese, A. and Lemaire, A., A coupled CFD-FEA study of a tunnel structure exposed to a fire, in: Grayson, S.J., ed., Interflam 2004 – 10th International Fire Science & Engineering Conference, Interscience Communications Ltd, London, 2004, 2, 1349–1360.
- [5] Welch, S., Miles, S., Kumar, S., Lemaire, T., Chan, A., FIRESTRUC - Integrating advanced three-dimensional modelling methodologies for predicting thermo-mechanical behaviour of steel and composite structures subjected to natural fires, in: Karlsson, B., ed., Fire Safety Science – Proceedings of the Ninth International Symposium, International Association for Fire Safety Science, Reykjavik, Iceland, 2008, 1315-1326.
- [6] Cooper, L.Y., Franssen, J.-M., Basis for using fire modeling with 1-D thermal analyses of partitions to simulate 2-D and 3-D structural performance in real fires, Fire Safety Journal, 1999, 33(2), 115-128.
- [7] McGrattan, K., Klein, B., Hostikka, S. and Floyd, J., Fire Dynamics Simulator (Version 5). User's guide, Special Publication 1019-5, National Institute of Standards and Technology (NIST), 2007.
- [8] Franssen, J.-M., SAFIR: A thermal/structural program for modeling structures under fire, Engineering Journal, 2005, 42(3), 143-158.
- [9] INERIS, Parcs de stationnement en superstructure largement ventilés. Avis d'expert sur les scénarios d'incendie, CTICM, 2001.
- [10] EN 1990, Eurocode 0: Basis of structural design, European Standard, CEN, 2002.

-
- [11] Decreto Ministeriale 14/01/08, Norme Tecniche per le Costruzioni, Consiglio Superiore dei Lavori Pubblici, 2008.
- [12] EN 1994-1-2, Eurocode 4: Design of composite steel and concrete structures Part 1-2: General rules - Structural fire design, European Standard, CEN, 2005.
- [13] EN 1992-1-2, Eurocode 2 Design of concrete structures Part 1-2: General rules – Structural fire design, European Standard, CEN, 2004.
- [14] Deckers X., Haga S., Tilley N. and Merci B., Smoke control in case of fire in a large car park: CFD simulations of full-scale configurations, Fire Safety Journal, 2013, 57, 22-34.
- [15] Ma, T.G. and Quintiere, J.G., Numerical simulation of axi-symmetric fire plumes: accuracy and limitations, Fire Safety Journal, 2003, 38(5), 467-492.

TOPIC 3

Development of a co-rotational beam element for the study of steel structures subjected to fire loadings

1 Introduction

Structural steel is one of the most employed construction materials in the field of civil engineering thanks to its numerous features that make it ideal for a large number of applications because of its relative light weight, high strength and ductility as well as of its ability to be combined with other buildings materials such as concrete, timber or glass. Steel represents a flexible choice that is suitable for small and medium-sized buildings (sheds, houses, offices) but it exhibits its maximum potentialities when employed for buildings such as: large complexes for exhibition, logistics, industry manufacturing, and in the construction of bridges, airports, stations etc. In fact, it allows to maximize building spaces by covering long spans, and at the same time ensuring ease of installation with resulting reduction in construction cost and time, in particularly if compared with other constructive solutions. Among the few weaknesses of steel structures, the fire behaviour represents a significant issue. In fact, steel has on one hand, the tendency to heat up quickly owing to high thermal conductivity and high section factors of the profiles, on the other hand it exhibits a rapid degradation with temperature of the mechanical properties such as yield strength and Young's modulus. In the past, these problems were often solved with the systematic use of active protection systems and material cover protection which have often proven to be a reliable system despite some exceptions [1]. In recent years the increase in labour costs combined with the serious economic crisis in the construction industry, have contributed to progressively move the attention towards the possibility to use unprotected steel by employing Natural Fire Safety Concept (NFSC) which relies on the use of natural fire models to represent the thermal action. It is also based on the definition of performance levels that can depend on the building typology. Surely, thermomechanical finite element software represents one of the main tools for analysing the behaviour of steel structures under fire in the context of NFSC. Thus a reliable numerical modelling of the structural behaviour under fire is paramount.

Many researchers have therefore contributed to introduce numerical models able to predict the real behaviour of structures involved in fire. In recent years Fire Engineering group in Nanyang Technological University developed for example the tool FEMFAN [2]; while Lien et al. [3] proposed a Vector Form Intrinsic Finite Element (VFIFE), for the nonlinear study of steel structures under the effect of high temperatures. The

common purpose always relies on the development of increasingly efficient computational devices able to predict the complexity of the physical thermomechanical phenomena. The developed procedures are usually compared with the available findings based on experimental tests that represents a fundamental step in the process of validation. In this sense a recognised reference finding is represented for instance by Cardington tests performed in the laboratory of the Building Research Establishment (BRE) on a full-sized composite frame. Other series of tests on steel structures under high temperatures are available in [4,5,6].

On this basis other specifically fire design programs for the analysis of structures subjected to high temperature have spread and commercialized during the years such as SAFIR, developed by Franssen at the University of Liege (Belgium), or VULCAN developed at the University of Sheffield (UK). In addition, multipurpose software such as ABAQUS, ANSYS, DIANA have increased their attention by introducing wider library of thermo-mechanical elements that connected with the use of more powerful interfaces have allowed to expand the treatment of these issues also in the engineering practice. On these premises, the reported research introduces a 2D beam finite element, developed in Matlab environment, for thermomechanical analysis of steel structures based on co-rotational theory, which is able to capture the effects of large displacements and rotations. Material nonlinearity and plasticity effects are taken into account also by means of EN1993-1-2 constitutive law for carbon steel at high temperature that was used to reproduce experimental tests on steel specimens. The main novelty is however represented in the implementation of a branch switching procedure for capturing instability effects at high temperature without introducing initial geometrical imperfections as it usually done in normal commercial codes. In fact, the benefit in the practice is twofold: i) reduction of the complexity of the model geometry that would not require the explicit inclusion of the global geometrical imperfection to capture buckling phenomena and ii) no need to assume the magnitude of the global geometrical imperfections that is often not trivial.

An optimisation of standard convergence procedure, based on a different choice of displacement predictor, was then introduced and tested. The potentialities of the element are shown by comparing it with the existing commercial software ABAQUS and SAFIR.

2 Co-rotational beam element

The proposed two dimensional thermomechanical finite element is derived from the co-rotational (CR) beam theory. This approach, that is an alternatively and more recent way to derive nonlinear finite elements, is basically characterized by the introduction of a local, element based, reference system. This local frame, that follows the element during its motion, supports the presence of a second global reference system that instead remains fixed. On this assumption the co-rotational approach mainly differs from Total Lagrangian (TL) or Updated Lagrangian (UL) formulations in which the description of

displacements and rotations necessary to derive the beam kinematic is fulfilled with reference to a unique fixed global reference system. A detailed description of the co-rotational formulation for a 2D dimensional beam element was introduced in [7], that discussed the idea of a “consistent CR formulation” where the stiffness matrix appears as the true variation of the internal force [8]. Other authors [9] proposed a modified form called “element independent co-rotational formulation” that lies on the use of projection operators, without any explicit use of “shadow” configurations [8]. The co-rotational formulation was also used as base to derive several beam finite elements characterized by specific capabilities for practical applications. Nonlinear dynamic co-rotational beam elements were introduced by [10], while [11] presented applications based on the development of co-rotational finite element for the study of composite beams with interlayer slips. The finite element presented hereinafter mainly follows the formulation developed by [7] and successively reported in [12] for the study of nonlinear beam elements at ambient temperature by now extending the field of application to the study of steel structures subjected to high temperatures.

Without entering into detail, with a recurring list of all kinematic quantities or equations introduced for the implementation of the thermo-mechanical finite element that are better presented in [7,12,13]; herein we limit our attention to the main features of this method by highlighting the potentialities but also the limits that may be involved in the use of such procedure. A synthetic scheme of the co-rotational beam finite element implementation with the description of the main kinematic terms is however presented, for completeness, in Section 3.

The idea of introducing a second reference system, that continuously translates and rotates with the element and that follows it as a “shadow”, was initially introduced by Horrigmoe and Bergan [14]. This assumption allows to potentially separate the motion of the element into two parts: a rigid body motion associated with the global fixed reference system and a pure deformation that is described with reference to the local frame. In this way, it is shown [15], that the tangent stiffness matrix can be obtained as the sum of two contributions: the first that depends only on the rotation and translation of the local reference system and a second contribution that whereas is connected to the deformation of the element expressed with reference to the local mobile frame. The use of a local reference system leads to obtain relative small values of displacement and rotation with reference to the local frame with a first significant advantage that relies in the low-order of nonlinearity associated to the local deformation. A second important aspect is that, when a linear formulation is selected for the description of the local strain, the co-rotational formulation allows to separate the treatment of geometrical and mechanical nonlinearities. The geometrical nonlinearities are taken into account at the level of the rigid body motion of the local reference system towards the global one, while the material nonlinearity are treated at the level of the local system. This allows to derive the tangent stiffness matrix and the internal force vector in a relative simplified way. The so obtained formulation is particular attractive for 2D dimensional problems while for 3D beams, the non-additive nature of three dimensional rotations entailed a

more complicated formulation necessary to define the beam kinematic. It is finally important to underline that the domain of application of the co-rotational theory is limited a priori by a kinematic assumption regarding the strain admissible limit. In other words the theory is generally employed for problems characterized by large displacements and rotations but under the assumption of small strains.

3 Finite element model implementation of co-rotational beam theory

A schematization of the procedure of the beam kinematic is herein synthetically reported. A more detailed description could be found in [7,12,13].

Due to the presence of two different reference systems, the co-rotational procedure implies the computations of element quantities for the two reference frames. Local element terms, as local internal force \mathbf{f}_{loc} vector and local tangent stiffness matrix \mathbf{K}_{loc} , are then initially computed in the local frame and then transformed into the global correspondent quantities \mathbf{f}_{glob} and \mathbf{K}_{glob} .

In order to provide a physical meaning to reported kinematic terms, Fig. 1 is then introduced.

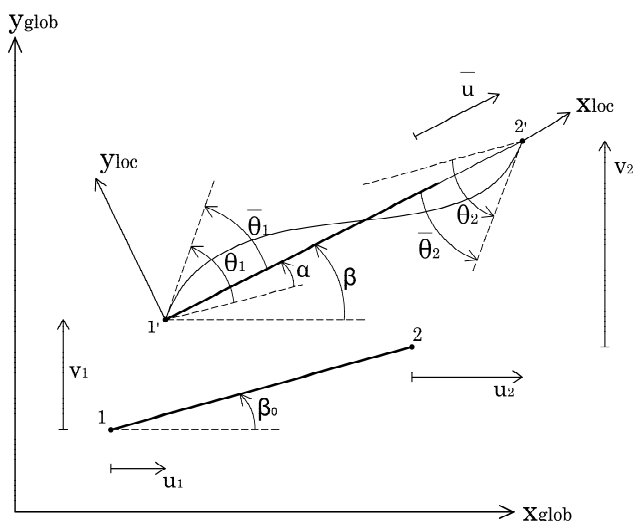


Fig.1 Beam Kinematic

Two different displacement vectors have to be defined for the local and global reference frame:

$$\mathbf{q}_{glob} = [u_1 \quad v_1 \quad \theta_1 \quad u_2 \quad v_2 \quad \theta_2]^T \quad (1)$$

$$\mathbf{q}_{loc} = [\bar{u} \quad \bar{\theta}_1 \quad \bar{\theta}_2]^T \quad (2)$$

In Fig.1, α denotes the angle of rigid rotation while with β and β_0 we indicate the inclination towards the global reference system of the beam line that connects the end nodes respectively in the initial and current configuration. When a solution \mathbf{u} is obtained in term of global displacements referred to free DOF, the co-rotational theory requires at the beginning the computation of the local quantities \mathbf{f}_{loc} and \mathbf{K}_{loc} .

Their derivation implies the definition of the local displacement terms of the vector \mathbf{q}_{loc} that are obtained from the current and initial length of the element (l_n, l_o), from the values of rotation in global displacements θ_1, θ_2 and by means of the rigid rotation angle α (see Eq. (3-5)).

$$\bar{u} = l_n - l_o \tag{3}$$

$$\bar{\theta}_1 = \theta_1 - \alpha \tag{4}$$

$$\bar{\theta}_2 = \theta_2 - \alpha \tag{5}$$

In Eq. (3-5) the terms $\theta_1, \theta_2, \alpha, l_n$ are function of the displacement components of the vector \mathbf{u} . In the co-rotational approach different beam theories (i.e. Bernoulli, Timoshenko) and formulations for the expression of local strain could be introduced at the local level; this potentially conduces to obtain different finite elements with different characteristics. The local strain is in any case function of the components of \mathbf{q}_{loc} .

A more detailed description of the local element formulations employed in this work and their capabilities with reference to thermomechanical applications are reported in the attached paper [13].

The derivation of internal local forces \mathbf{f}_{loc} and local stiffness matrix \mathbf{K}_{loc} is then performed on the base of the theorem of virtual work. A Gauss quadrature integration at the level of cross section and beam length, is performed in order to treat the nonlinear relation between stresses and strains on the base of the specific constitutive law chosen to describe the material behaviour. After obtaining the value of \mathbf{f}_{loc} and \mathbf{K}_{loc} the global quantities are finally computed by means of the application of matrix transformation that takes into account the kinematic terms introduced at the beginning of the paragraph and reported in Fig.1. A more detailed description is present in [13].

The procedure that allows to obtain new solution points is then similar to conventional finite element kinematic theory, as hereinafter described. The computation is performed based on the global quantities, nevertheless when a global term is introduced, the co-rotational theory suppose that a preliminary computation of the local quantities, on the base of the specific local formulation assumed to describe local strains, has already been performed.

-At the generic step, a solution equilibrium point, in terms of displacement vector \mathbf{u} is searched, by iterative solving through a Newton Raphson scheme, the system of nonlinear Eq. (6)

$$(\mathbf{f}_{\text{glob}} - \mathbf{f}_{\text{ext}}) = \mathbf{f}_{\text{res}} = \mathbf{K}_{\text{glob}} \mathbf{u} \quad (6)$$

In Eq. (6) the internal force vector \mathbf{f}_{glob} and the stiffness matrix \mathbf{K}_{glob} are expressed as global quantities; whilst with \mathbf{f}_{ext} we indicate the external force vector that subtracted to \mathbf{f}_{glob} defines the residual term \mathbf{f}_{res} whose norm is checked in order to satisfy a tolerance value r that is accurately fixed. If the check is satisfied the displacement vector \mathbf{u} represents the new equilibrium point of the solution at step i , otherwise new iterations are performed by updating the value of \mathbf{u} until convergence is obtained.

-when a new step is introduced, and a variation in applied forces is performed, a first computation of \mathbf{f}_{glob} and \mathbf{K}_{glob} is fulfilled based on a displacement trial solution predictor $\mathbf{u}_{\text{trial}}$. This predictor is usually chosen equal to the last converged solution \mathbf{u} at the previous step, although different choices could be performed in order to reduce the computational cost as discussed and proposed in [13]. A new norm is then computed by using new values of \mathbf{f}_{glob} and \mathbf{f}_{ext} at new step. If the norm r does not satisfy the fixed tolerance new iterations inside Newton Raphson loop are necessary in order to obtain the new solution \mathbf{u} valid for the new step.

The following algorithm better summarises what introduced:

Table 1 Solution scheme for a co-rotational finite element

<p>-known quantities at step n: $\mathbf{u} \quad \lambda \quad \mathbf{K}_{\text{glob}}(\mathbf{u}) \quad \mathbf{f}_{\text{glob}}(\mathbf{u})$</p> <p>-new step n+1: $\lambda = \lambda + \Delta\lambda$ $\mathbf{f}_{\text{res}}(\mathbf{u}) = \mathbf{f}_{\text{glob}}(\mathbf{u}) - \lambda \mathbf{f}_{\text{ext}}$ $r = \ \mathbf{f}_{\text{res}}(\mathbf{u})\$ <i>while</i> $r > \text{tol}$ $\Delta\mathbf{u} = -\mathbf{K}_{\text{glob}}^{-1} \mathbf{f}_{\text{res}}(\mathbf{u})$ $\mathbf{u} = \mathbf{u} + \Delta\mathbf{u}$ compute $\mathbf{K}_{\text{glob}}(\mathbf{u}) \quad \mathbf{f}_{\text{glob}}(\mathbf{u})$ $\mathbf{f}_{\text{res}}(\mathbf{u}) = \mathbf{f}_{\text{glob}}(\mathbf{u}) - \lambda \mathbf{f}_{\text{ext}}$ $r = \ \mathbf{f}_{\text{res}}(\mathbf{u})\$ <i>end</i></p>
--

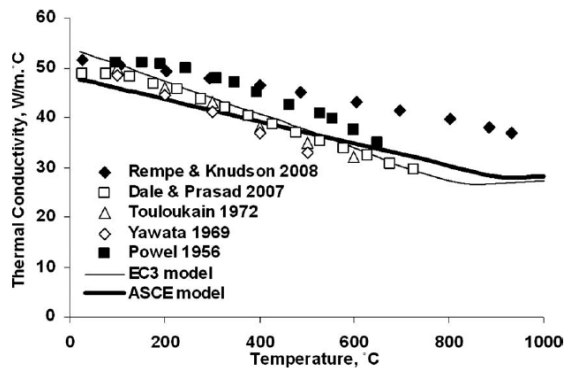
The algorithm represents a typical solution based on a load control procedure with a Newton Raphson corrector scheme. In the case of fire analysis, the external load \mathbf{f}_{ext} , associated to mechanical forces, is reasonably assumed constant at each step so the load parameter λ could be fixed as 1. The increment of temperature is introduced at each step by computing the relative thermal elongation and the degradation of the material

mechanical properties. An additive procedure, necessary to update the values of stresses and strains and the variation of the constitutive law with temperature, has to be supported to the solution scheme here presented. This procedure is briefly described Section 5 and better investigated in [13].

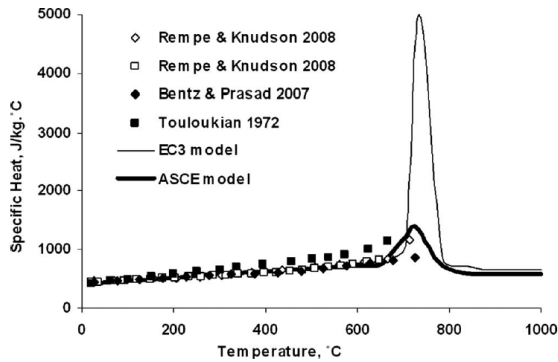
4 Thermomechanical behavior of carbon steel at high temperature

The proposed finite element is specifically conceived for the study of steel structures under high temperatures. As a consequence, an adequate knowledge of material behavior under fire conditions is paramount in order to define realistic and accurate models that allow to evaluate the fire resistance of steel members via finite element simulations. Thermal, mechanical and deformations properties must be consequently investigated.

In the specific case, the definition of thermal properties is not fundamental because the cross section temperature field is given as an input data based on a heat transfer analysis that is previously performed. Nevertheless, if a thermal analysis is initially performed, the knowledge of thermal conductivity and specific heat is essential to derive the regime of temperatures necessary in order to then derive the mechanical response. Kodur et al. [16] review the available tests and models, available in literature, regarding thermal conductivity and specific heat (see Fig. 2a and Fig. 2b).



(a)

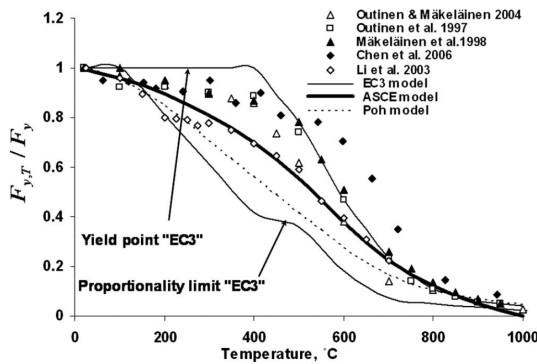


(b)

Fig.2 Steel properties under the effect of temperature as predicted by models and experimental tests;

a) Thermal conductivity, b) Specific heat [16]

In any case, the input data introduced for all the fire analyses and reported in [13] follow the thermal properties and computation methods provided by EN1993-1-2 [17]. Conversely, the mechanical properties and how they change with temperature are directly taken into account in the definition of the beam element. The degradation of yield strength and elastic modulus was historically derived from experimental tests performed according to transient or steady-state conditions. As described in [16] variations in test methods, as for example the application of a different strain rate, produce direct effects on the derived mechanical properties. Since only limits for strain rates are defined by codes, a great variability in terms of results is present between different test data as shown in Fig. 3a and Fig. 3b.



(a)

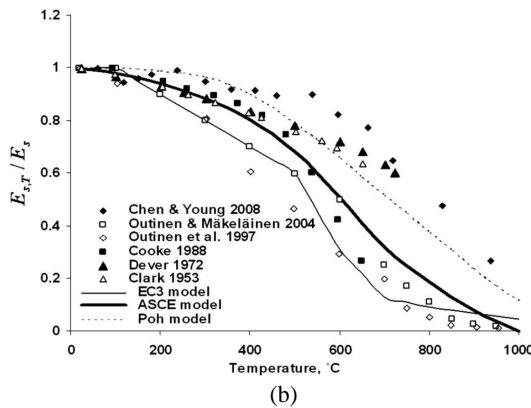


Fig.3 Steel properties under the effect of temperature as predicted by models and experimental tests;

a) Yield strength, b) Elastic modulus [16]

It's also interesting to observe that different models (Eurocode 3 and ASCE) provided different degradation curves, for example the Eurocode 3 curve is more conservative than ASCE predictions for the elastic modulus whilst for the yield strength Eurocode 3 assumes no reduction until the temperature of 400 °C. The proposed finite element implements the mechanical steel properties of Eurocode 3 although in the validation phase against experimental tests [13] the degradation coefficients proposed by [18] were assumed in order to better fit test results. In both cases the constitutive stress-strain curve is the one proposed by the Eurocode and depicted in Fig. 4.

The curve implies also the definition of a proportional limit f_p .

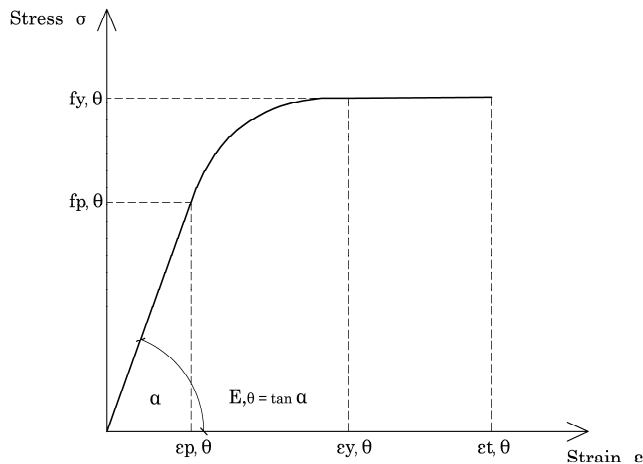


Fig.4 Eurocode 3 stress-strain constitutive law for carbon steel at high temperature

The choice of such constitutive law was also suggested by the opportunity to take into account implicitly part of the high-temperature creep strain [18, 19] whose effects in steel could become noticeable at temperature above 300°C-400°C [16]. An application with a bilinear constitutive law was also introduced in [13].

Finally the deformation properties are described by the definition of the thermal strain that is introduced in according to Eurocode 3 prescriptions. A comparison of implemented thermal strain with the provision of ASCE model and the outcomes of experimental tests is reported in Fig. 5.

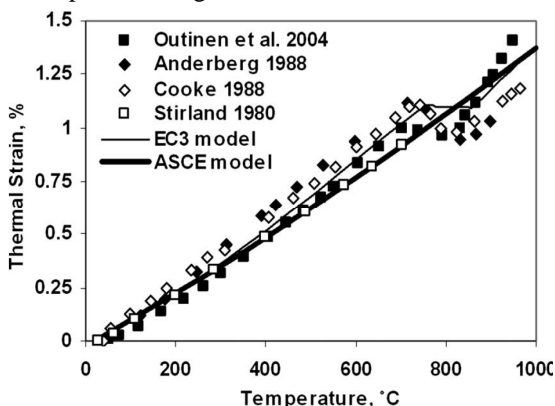


Fig.5 Thermal strain: comparison between available models and experimental data outcomes [16]

5 Integration of material constitutive law

In the previous paragraphs the co-rotational beam formulation was introduced in order to describe the principles of beam kinematics and the derivation of local and global expression of internal force vector and stiffness tangent matrix. Under this form, the finite element is potentially able to perform nonlinear analysis by taking into account geometrical and material nonlinearity.

The purpose is now to extend the field of application of the finite element by introducing the effects of temperature on steel numerical-simulated structures.

With reference for example to a uniaxial problem the total strain is given by:

$$\epsilon_T = \epsilon_\sigma + \epsilon_0 \tag{7}$$

In Eq. (7) ϵ_T represents the total strain that is now obtained as the sum of the stress-related strain ϵ_σ and the initial strain ϵ_0 . In the initial strain is then possible to distinguish between different contributions as the effect of thermal dilatation ϵ_{th} or creep strain ϵ_{cr} that, as introduced in the previous paragraph, could implicitly taken into account because of a specific choice of the integrated stress-strain law [18, 19].

After defining the strain quantities it's then possible specify the integration scheme that

allows to compute at each new step, and for each Gauss integration point, the updated value of stress, tangent modulus and consequently derive, the new expression of local tangent stiffness matrix and internal force vector. The procedure differs depending on the specific local formulation that is adopted to formulate the local strain. In the case of Bernoulli element the integration of constitutive law was performed on a uniaxial law; for the Timoshenko element the material integration is defined under plane stress conditions by considering a Von Mises yield surface. The proposed models are based on the assumption of isotropic hardening that is a quite satisfactory assumption for steel structure involved in fire. The procedure for the integration of the material constitutive law at different temperature is hereinafter briefly reported limiting to the uniaxial case. This method allows to move from an equilibrium point at step n to a new value of stress on the constitutive material law at temperature T_{n+1} by taking into account the variation of temperature that is performed between the steps.

Under the effect of temperature the axial strain increment is given by:

$$\Delta\varepsilon = \Delta\varepsilon_{\sigma} + \Delta\varepsilon_{th} \quad (8)$$

Where $\Delta\varepsilon_{\sigma}$ is the strain increment induced by stress while $\Delta\varepsilon_{th}$ is the thermal strain increment that could be expressed as:

$$\Delta\varepsilon_{th} = \alpha_{th}\Delta T = \alpha_{th}(T_{n+1} - T_n) \quad (9)$$

In Eq. (9), α_{th} represents the thermal expansion coefficient, T_n and T_{n+1} respectively the temperature at time n and $n+1$.

With reference again to Fig. 6, when a thermal increment ΔT is introduced from a converged solution at temperature T_n point (A), the updating procedure that allows to compute the new values of stress and tangent modulus $En=d\sigma/d\varepsilon$ at temperature T_{n+1} follows the curve A-B-C. The A-B curve represents the unloading until point B with residual strain ε_{pl} , that is assumed as a reference point in order to process a new loading at temperature (B-C curve), this choice is set due to the hypothesis that the plastic strain is not affected by a temperature variation [20]. Point C represents finally the new value of stress that is obtained on the stress-strain curve at T_{n+1} .

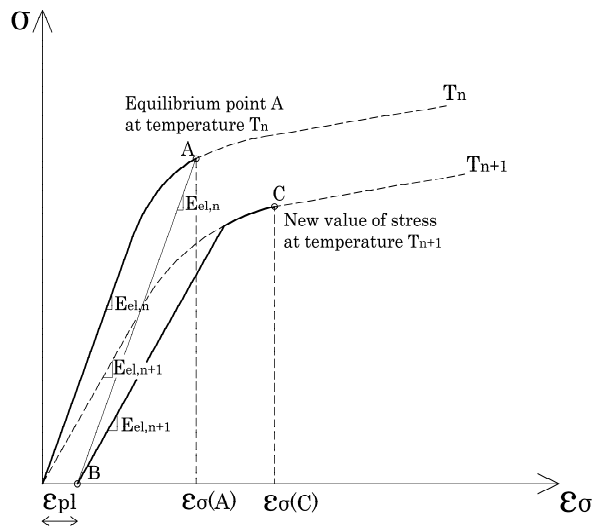


Fig. 6 Integration of material uniaxial constitutive law at high temperature

Several examples of steel frames subjected by fire in [13]. Experimental tests and commercial finite element outcomes obtained under same results are compared with the predictions of the developed finite element. ABAQUS and SAFIR software were introduced for the comparison. An example of validation against an experimental test, based on a steel frame subjected to ISO 834 curve, is reported in Fig.7. Fig. 8 shows instead the numerical comparison between the co-rotational beam element and the SAFIR software outcomes in term of displacements on a heated L steel frame. The complete descriptions of the case studies, together with other examples, are reported in [13].

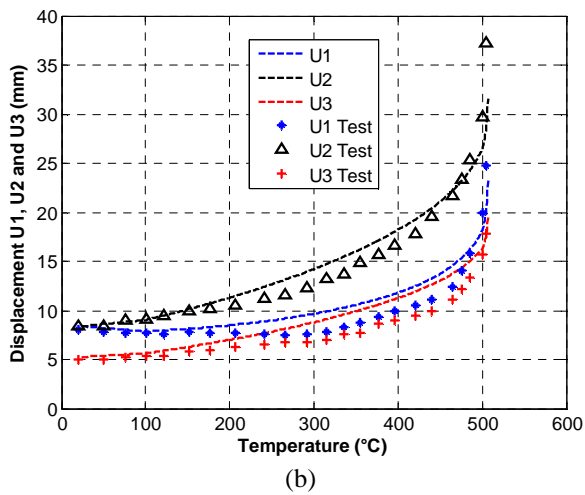
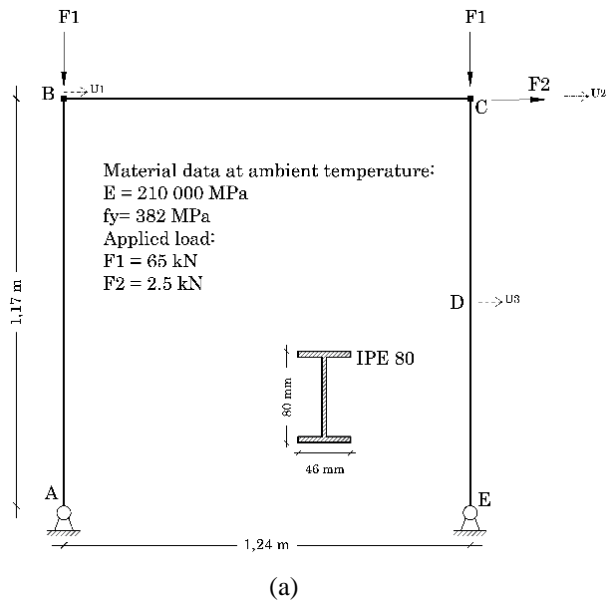


Fig. 7 Finite element validation against experimental test: steel portal frame subjected to an ISO 834 fire curve; a) Geometry and data of the case study, b) Comparison of displacements as function of element temperature

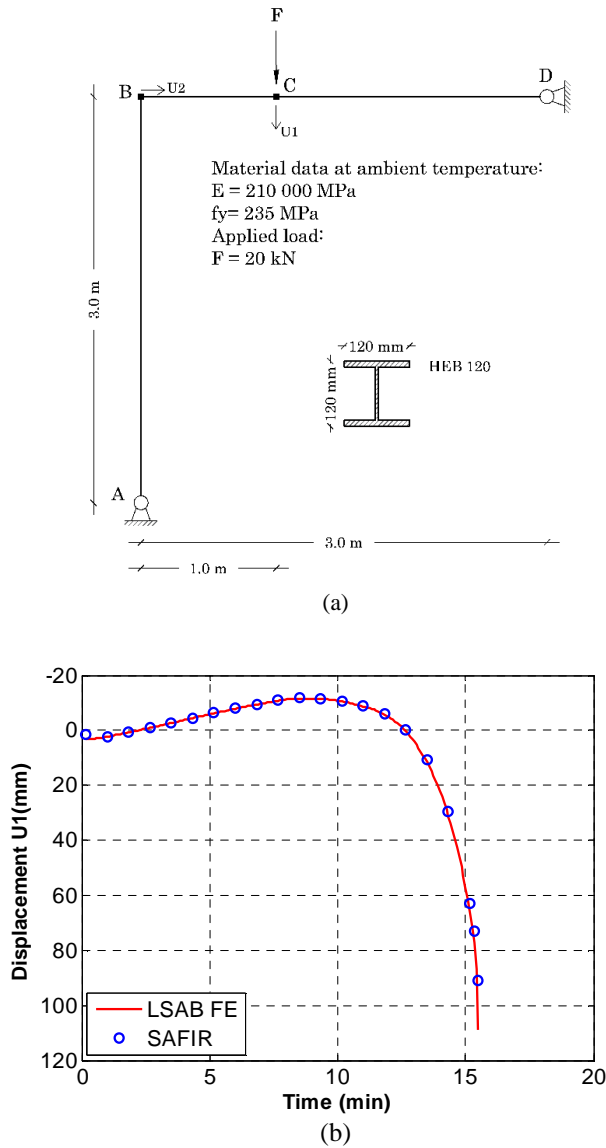


Fig. 8 Example of finite element validation against numerical predictions of SAFIR software; a) Geometry and data of the case study, b) Comparison between the two models on the vertical displacement of loaded node

6 Optimization of convergence procedure based on different displacement predictor

Some improvements were tested on the thermomechanical code in order to optimize the time of analysis. A modified displacement predictor is tested in [13] to increase the efficiency of the structural nonlinear analysis. The objective is to ensure an improvement in terms of computational cost of the solution through modification of the displacement estimate with which the Newton-Raphson iteration scheme starts at each time step.

In the classical approach the Newton-Raphson scheme starts from the solution computed at the last converged equilibrium point, namely the value of the displacement at free DOF nodes.

$$u_{n+1} = u_n \tag{10}$$

The tested predictor, that should improve the computational efficiency, is based on the simple but reasonable idea that when high nonlinear analyses are performed, the knowledge of the history pattern of the previously converged solutions is meaningful to estimate the trial equilibrium point. On these premises, the modified displacement predictor is a linear function of u_n and u_{n-1} , as shown in Eq. (11)

$$u_{n+1} = u_n + \frac{t_{n+1} - t_n}{t_n - t_{n-1}} (u_n - u_{n-1}) \tag{11}$$

In Eq. (11), not only the last converged solution u_n but also the second last equilibrium point u_{n-1} is exploited to provide a more realistic value of the trial displacement solution u_{n+1} . Tests of optimisation were performed on some case studies in order to prove the advantage in using such predictor by obtaining comforting results [13].

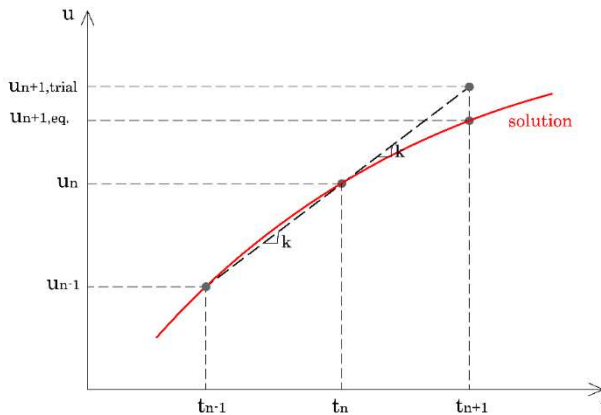


Fig. 9 Scheme of the proposed displacement predictor

7 Path following techniques, branch-switching procedure applied to instability problems of steel structures subjected to fire

A specific section is reported in [13] for the analysis of instability phenomena in elastoplasticity and under the effect of high temperatures. The purpose is to introduce a direct procedure, hereinafter indicated as branch-switching, that allows to analyse post buckling behavior without explicitly introducing any geometrical imperfections or alternatively small forces in order to induce instability. Generally, FE codes used for structural fire applications need to explicitly introduce the geometrical imperfections, sometimes in approximated way with the application of equivalent horizontal forces, as shown in Fig. 10; the branch switching procedure analyses instead the ideal problem. In this way the user does not need to identify and quantify geometrical shape and amplitude imperfections or alternatively estimate a suitable value of equivalent forces. This consequently increases the level of solution reliability by reducing preliminary and time consuming operations that should be neglected. As a result, this procedure has the major advantage to detect possible bifurcation points of a structural system that is subjected to both mechanical and thermal loads. In fact, since the thermal loads typically vary with time also the buckling modes do, because of the thermal effect on the structure, i.e. thermal expansion, possible load redistribution, loss of stiffness etc. Thus, for a generic thermal exposure, the buckling mode shapes at ambient temperature are different from those at elevated temperature and it can be extremely difficult to foresee them a priori. A linear buckling analysis performed at ambient temperature to identify the initial imperfections to be introduced into the model could be even misleading. Conversely, the proposed FE has shown the ability to overcome this issue.

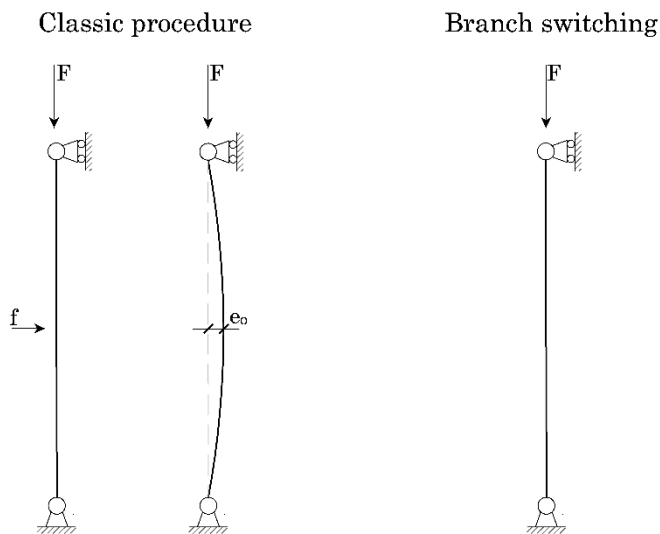


Fig. 10 Difference between the finite element model of a compressed column to be introduced

in a commercial finite element code and via branch-switching procedure

The implemented method allows to automatically detect bifurcation points on the fundamental equilibrium path and then performing branch-switching on the secondary path when instability occurs. The branch switching procedure support the conventional algorithm necessary to consequentially obtained new equilibrium points, nevertheless this method is activated only on the base of a check that is performed at the end of the solution step on the base of the properties of the global converged stiffness matrix \mathbf{K}_{glob} . Table 2 summarises the difference between the conventional procedure and what instead is performed when branch switching is activated.

A more detailed description of the procedure is present in [13], the method is based on minimization procedure and notion of instability introduced by Petryk [21]. The idea is that along a stable deformation path, the displacement \mathbf{u} corresponds to an absolute minimum of the functional J .

$$J = \frac{1}{2} \mathbf{u}^T \mathbf{K} \mathbf{u} - \mathbf{u}^T \mathbf{f}_{ex} \quad (12)$$

Branch switching introduce an incremental solution to equilibrium equations that reduces J , in this way an unstable fundamental path is rejected and a stable secondary path is selected.

The critical point is detected by computing the diagonal matrix \mathbf{w} containing the eigenvalues of the global stiffness matrix \mathbf{K} calculated at each converged solution. If one or more negative eigenvalues are present in the diagonal matrix ($\lambda_1, \lambda_2, \lambda_3, \dots$), the solution computed at that equilibrium point represents a possible critical point. After having obtained the position of the critical point, the first solution on the secondary path is computed by minimizing J . In order to do that a new displacement predictor \mathbf{u}_{BS} has to replace the old one. The new displacement predictor is obtained by introducing a perturbation vector which in principle can be arbitrary. However, it is common practice to use the eigenvector \mathbf{v} associated with the corresponding negative, and highest in absolute value, eigenvalue λ_{\min} of \mathbf{K} as highlighted in Eq. (13)

$$\mathbf{u}_{BS} = \mathbf{u} + \frac{1}{100} \frac{\|\mathbf{u}\|}{\|\mathbf{v}\|} \mathbf{v} \quad (13)$$

Table 2 Modifications introduced in the solution scheme by branch-switching procedure

Conventional procedure	Branch switching procedure
<p>known quantities at <i>step n</i>: \mathbf{u} $\mathbf{K}_{glob}(\mathbf{u})$ $\mathbf{f}_{glob}(\mathbf{u})$ \mathbf{K}_{glob} is positive definite</p> <p>new <i>step n+1</i>: $T = T + \Delta T$ $\mathbf{f}_{res}(\mathbf{u}) = \mathbf{f}_{glob}(\mathbf{u}) - \mathbf{f}_{ext}$ $r = \ \mathbf{f}_{res}(\mathbf{u})\$ while $r > tol$ $\Delta \mathbf{u} = -\mathbf{K}_{glob}^{-1} \mathbf{f}_{res}(\mathbf{u})$ $\mathbf{u} = \mathbf{u} + \Delta \mathbf{u}$ compute $\mathbf{K}_{glob}(\mathbf{u})$ $\mathbf{f}_{glob}(\mathbf{u})$ $\mathbf{f}_{res}(\mathbf{u}) = \mathbf{f}_{glob}(\mathbf{u}) - \mathbf{f}_{ext}$ $r = \ \mathbf{f}_{res}(\mathbf{u})\$ end</p>	<p>known quantities at <i>step n</i>: \mathbf{u} $\mathbf{K}_{glob}(\mathbf{u})$ $\mathbf{f}_{glob}(\mathbf{u})$ \mathbf{K}_{glob} is not positive definite</p> <p>new <i>step n+1</i>: $T = T + \Delta T$ $\mathbf{u}_{BS} = f(\mathbf{u}, \mathbf{v}_{min})$ $\mathbf{f}_{res}(\mathbf{u}_{BS}) = \mathbf{f}_{glob}(\mathbf{u}_{BS}) - \mathbf{f}_{ext}$ $r = \ \mathbf{f}_{res}(\mathbf{u}_{BS})\$ while $r > tol$ $\Delta \mathbf{u} = -(\mathbf{K}_{glob} + 1.1 \lambda_{min} \mathbf{I})^{-1} \mathbf{f}_{res}(\mathbf{u}_{BS})$ $\mathbf{u} = \mathbf{u}_{BS} + \Delta \mathbf{u}$ compute $\mathbf{K}_{glob}(\mathbf{u})$ $\mathbf{f}_{glob}(\mathbf{u})$ $\mathbf{f}_{res}(\mathbf{u}) = \mathbf{f}_{glob}(\mathbf{u}) - \mathbf{f}_{ext}$ $r = \ \mathbf{f}_{res}(\mathbf{u})\$ end</p>
<p>compute eigenvalues λ_i and associated eigenvectors \mathbf{v} of \mathbf{K}_{glob} check if \mathbf{K}_{glob} is positive definite</p>	<p>compute eigenvalues λ_i and associated eigenvectors \mathbf{v} of \mathbf{K}_{glob} check if \mathbf{K}_{glob} is positive definite</p>

The minimization procedure consists in solving at each iteration the nonlinear system:

$$(\mathbf{K}^i + \mu \mathbf{I}) \Delta \mathbf{u} = -\mathbf{r}^i \tag{14}$$

where \mathbf{I} is the identity matrix, \mathbf{r} is the residual vector while μ is a coefficient that can be set equal to either $1.1 \lambda_{min}$, where λ_{min} is the lowest eigenvalue of \mathbf{K} , or to 0 if \mathbf{K} is positive definite. At the end of each iteration the displacement is updated by means of:

$$\mathbf{u}^{i+1} = \mathbf{u}^i + \Delta \mathbf{u} \tag{15}$$

The successive equilibrium points on the secondary path are then computed through

classical Newton-Raphson procedure.

More details and results of branch-switching applications on steel members subjected to instability under the effects of high temperatures are reported and discussed in [13].

References

- [1] NIST, *Final Report on the Collapse of World Trade Center Building 7, Federal Building and Fire Safety Investigation of the World Trade Center Disaster*, 2008
- [2] Tan K.H., Ting S.K., Huang Z.F., *Visco-elasto-plastic analysis of steel frames in fire*, Journal of Structural Engineering ASCE (2002);128(1): 105-114
- [3] Lien K.H., Chiou Y.J., Wang R.Z., Hsiao P.A., *Vector Form Intrinsic Finite Element analysis of nonlinear behavior of steel structures exposed to fire*, Engineering Structures (2010); 32: 80-92
- [4] Wang Y.C., Moore D.B., *Steel frames in fire: analysis*, Engineering Structures (1995); 17(6): 462-472
- [5] Franssen J.M., Cooke G.M.E., Latham D.J., *Numerical Simulation of a Full Scale Fire Test on a Loaded Steel Framework*, Journal of Constructional Steel Research (1995); 35: 377-408
- [6] Zhao J.C., Shen Z.Y., *Experimental studies of the behaviour of unprotected steel frames in fire*, Journal of Constructional Steel Research (1999); 50: 137-150
- [7] Crisfield M.A., *Non-linear Finite Element Analysis of Solids and Structures, Volume 1: Essentials*, Wiley, Chichester, England
- [8] Felippa C.A., Haugen B., *Unified Formulation of Small-Strain Corotational Finite Elements: I. Theory*, Report No. CU-CAS-05-02, Department of Aerospace Engineering Sciences and Center for Aerospace Structures, University of Colorado 2005
- [9] Rankin C.C., Brogan F. A., *An element-independent corotational procedure for the treatment of large rotations*, ASME J. Pressure Vessel Technology (1986), 108, 165–174
- [10] Le T-N., Battini J-M., Hjjaj M., *A consistent 3D corotational beam element for nonlinear dynamic analysis of flexible structures (2014)*, Computer Methods in Applied Mechanics and Engineering; 269: 538-565
- [11] Battini J-M., Nguyen Q-H., Hjjaj M., *Non-linear finite element analysis of composite beams with interlayer slips*, Computers & Structures (2009); 87(13-14): 904-912
- [12] Battini J.M., *Co-rotational beam elements in instability problems*, PhD thesis (2002), Department of Structural Engineering KTH, Stockholm, Sweden
- [13] Morbioli A., Battini J-M., Tondini N., *A co-rotational two dimensional beam element for the analysis of elastic-plastic instability of steel structures subjected to fire*

-
- [14] Horrigmoe G., Bergan P.G., *Instability analysis of free-form shells by flat finite elements*, Computer Methods in Applied Mechanics and Engineering (1978);16: 11–35
- [15] Krenk S., *Non-linear modelling and analysis of solids and structures*, Cambridge University Press, New York, 2009.
- [16] Kodur V., Dwaikat M., Fike R., *High-temperature Properties of Steel for Fire Resistance Modeling of Structures*, Journal of Materials in Civil Engineering (2010): 22(5): 423-434
- [17] European Committee for Standardisation, *Eurocode 3 Design of steel structures - Part 1-2. General rules Structural fire design*
- [18] Rubert A., Schaumann P., *Structural Steel and Plane Frame Assemblies under Fire Actions*, Fire Safety Journal (1986); 10: 173-184
- [19] Buchanan A.H., *Structural design for fire safety*, Wiley, New York, 2001
- [20] Franssen J.M., The Unloading of Building Materials Submitted to Fire, Fire Safety Journal (1990): 213-227
- [21] Petryk H., Thermann K., *On discretized plasticity problems with bifurcation*, International Journal of Solids Structures (1992); 29(6): 745-765

**PAPER 3: A co-rotational two dimensional beam element for the
analysis of elastic-plastic instability of steel structures subjected to
fire**

A co-rotational two dimensional beam element for the analysis of elastic-plastic instability of steel structures subjected to fire

Andrea Morbioli¹, Nicola Tondini^{1*} and Jean-Marc Battini²

¹University of Trento – Department of Civil, Environmental and Mechanical Engineering, Via Mesiano, 77 38123, Trento, Italy

²KTH, Royal Institute of Technology - Department of Civil and Architectural Engineering, SE-10044 Stockholm, Sweden.

*Corresponding author: Tel: +39 0461 28 19 76; e-mail address:

nicola.tondini@unitn.it

Keywords: Co-rotational formulation, steel structures, fire behaviour, path-following technique, branch-switching procedure, flexural instability, buckling analysis

Abstract

The paper describes the development of a two-dimensional (2D) nonlinear beam finite element that includes advanced path-following capabilities for detecting bifurcation instability of steel elements subjected to fire loading. The beam finite element has been conceived for analysing phenomena typically exhibited by steel structural elements subjected to fire such as material property degradation and large displacements. The element implements both Euler-Bernoulli and Timoshenko beam theories and could therefore be used to analyse slender to moderately stocky structures. A co-rotational formulation was implemented for describing the beam kinematic. The degradation of the steel mechanical properties at high temperature according to the Eurocode 1993-1-2 was accounted for by integrating the material constitutive law based on a predetermined temperature field in the cross section. An improved displacement predictor for estimating the displacement field at the beginning of each time step was successfully implemented and allowed to significantly decrease the computational time. Furthermore, advanced path-following methods that detect secondary equilibrium paths owing to instability occurrence were implemented to analyse the elastic-plastic

post-buckling behaviour of compressed steel elements at high temperature without the need of introducing geometrical imperfections. In order to highlight the potential practical implications of the developed finite element, a parametric analysis was performed to show that the element is able to reproduce the EN1993-1-2 buckling curve. Validation against experimental data found in literature and numerical outcomes obtained with commercial software like ABAQUS and SAFIR is thoroughly described.

1 INTRODUCTION

Numerical modelling by means of the finite element (FE) method has become very popular in the structural engineering community. In fact, the increased capabilities of commercial FE software associated with reduced computational time and increased user-friendliness have determined widespread diffusion in design offices. However, despite the wide use of such codes, the majority of the structural FE analyses performed in the practice still remains in the linear range, even in cases where a high nonlinear behaviour is expected; e.g. the seismic behaviour of a dissipative moment resisting frame analysed by means of linear dynamic analysis with elastic response spectrum reduced by the behaviour factor. An exception stands out and it is when FE simulations are employed to analyse the structural fire behaviour. In this case, the structural elements affected by thermal attack exhibit both distributed material nonlinearity owing to mechanical property degradation at elevated temperature and geometrical nonlinearity due to large displacements and there is no means to account for them in a simplified manner by carrying out linear FE analyses. Thus, it is clear that the FE elements selected to model structures under fire action need to capture these highly nonlinear phenomena if the results can be considered representative of the actual behaviour. In this respect, the fire design of steel structures takes particularly advantage of an accurate FE structural modelling that can considerably increase their economical convenience by reproducing beneficial mechanisms that can be established during the fire such as: catenary action of restrained beams [1,2], membrane action of steel-concrete composite slabs [3,4]. Many researchers have therefore contributed to introduce numerical models able to predict the behaviour of structures subjected to fire. For instance, in recent years the Fire Engineering group in Nanyang Technological University developed the tool FEMFAN [5]; while Lien et al. [6] proposed a Vector Form Intrinsic Finite Element (VFIFE), for the nonlinear study of steel structures under the effect of high temperatures. The common purpose relies on the development of increasingly efficient computational tools able to predict the complexity of the physical thermomechanical phenomena. In this respect, other specifically-conceived FE software for the analysis of structures subjected to high temperature have spread and commercialized over the years such as SAFIR, developed at the University of Liege (Belgium) [7], VULCAN developed at the University of Sheffield (UK) [8, 9] and ADAPTIC developed at Imperial College (UK)[10]. In addition, multipurpose software such as ABAQUS [11], ANSYS [12], DIANA [13] have widened their library of thermomechanical elements to expand the treatment of these problems in the engineering practice.

It is well known that steel structures are sensitive to buckling phenomena. In particular, members that can be modelled as monodimensional elements, like columns, that are subjected to compressive stresses generally exhibit bifurcation buckling. Moreover, imperfections, both mechanical and geometrical, influence the behaviour of compression steel members. On these premises, buckling curves for design purposes were obtained and included in the Eurocodes [14, 15]. In this context, commercial FE codes commonly need to explicitly model these imperfections, though sometimes approximated via equivalent horizontal forces, in order to capture instability of an axially compressed element. For example, if for a single element the introduction of global geometrical imperfections with sinusoidal shape and amplitude in the order of $h/1000$, where h is the column length, is not particularly problematic; it is surely less straightforward when we have to deal with structural systems composed of several members. In fact, the buckling modes may not be easy to identify; thus, a linear elastic buckling analysis may be required a priori and FE codes used in structural fire engineering typically do not have this capability, e.g. SAFIR. In addition, the geometry of the FE model becomes more complicated to implement if the geometrical imperfections are explicitly accounted for and the choice of their magnitude represents another issue. In case of a fire, the buckling modes may change over time owing to degradation of material mechanical properties and the consequent variation of the relative stiffness between adjacent members. Thus, load redistribution can also occur. On these premises, this work aims to overcome the aforementioned issues by developing a 2D beam finite element that implements a branch-switching procedure able to capture at each converged solution possible elastic-plastic flexural instability at high temperature without introducing initial geometrical imperfections. Branch-switching procedures have been successfully implemented in beam FE at ambient temperature [16, 17]. However, there is a lack of works regarding the development of such techniques in thermomechanical finite elements. Thus, the paper is mainly devoted to close this gap and intends to highlight the practical implications by comparing, for example, the obtained results with the EN1993-1-2 [15] buckling curve.

In the design practice, low computational demand is sought and beam FEs are typically employed to model columns and beams unless local instabilities are foreseen. In addition, nonlinear analyses require iterative procedures to converge to an equilibrated solution. Thus, in a nonlinear FE formulation a good choice of the displacement predictor can entail faster convergence. In this respect, the paper presents an optimisation of standard convergence procedure, based on an improved displacement predictor at the beginning of each time step.

The article is articulated as follows: Section 2 describes in detail the co-rotational framework and the Bernoulli and Timoshenko local formulations; Section 3 provides insight into the integration of the constitutive material law at high temperature; Section 4 describes the improved displacement predictor and presents the development of branch-switching procedures; Section 5 shows the numerical examples aimed at validating the conceived beam finite element against experimental and simulated data

with ABAQUS and SAFIR; Section 6 describes the branch-switching capabilities on numerical examples and the practical implications; Section 7 draws the conclusions and future perspectives.

2 CO-ROTATIONAL FORMULATION

The idea of the co-rotational method is to decompose the motion of the element into rigid body and deformational part. During the rigid body motion, a local coordinates system, fixed to the element, moves and rotates with it. The deformational part is measured in this local system. The internal force vector and tangent stiffness matrix are first calculated with reference to the local system and then transformed with regard to the global one by using the transformation matrices relating local and global nodal quantities. The main advantage of the method is that with an appropriate choice of the element length, the local deformations are small. Consequently, existing linear elements or elements with a low order of nonlinearity can be used as local formulations.

2.1 Co-rotational framework

The co-rotational basic formulation for a two dimensional beam element is hereinafter presented. The description follows what introduced in [18] and subsequently reported in [17].

Since the co-rotational theory is based on the use of two different reference systems, it is essential to define a relation between the local and global expressions of the internal force vector and tangent stiffness matrix. Fig. 1 shows the kinematics quantities that are involved in the element motion according to the co-rotational formulation.

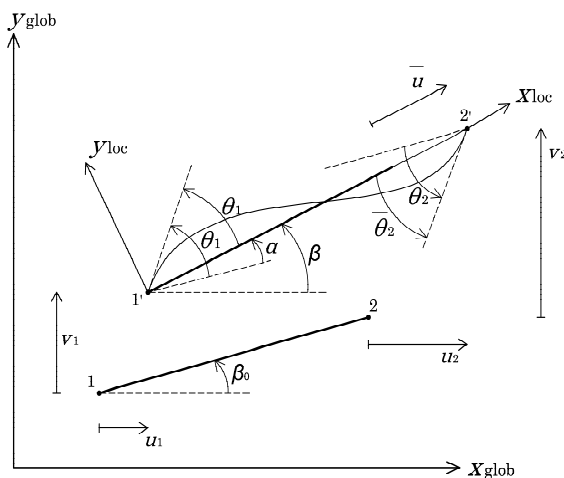


Fig. 1 2D co-rotational formulation

As shown in Fig.1 the co-rotational beam is represented by a two-node element whose

nodes 1 and 2 coordinates referred to the global fixed reference system $(x_{\text{glob}}, y_{\text{glob}})$ are respectively (x_1, y_1) and (x_2, y_2) . A second moving local reference system $(x_{\text{loc}}, y_{\text{loc}})$ is then introduced. Different vectors for global \mathbf{q}_{glob} and local displacement \mathbf{q}_{loc} are respectively defined:

$$\mathbf{q}_{\text{glob}} = [u_1 \quad v_1 \quad \theta_1 \quad u_2 \quad v_2 \quad \theta_2]^T \quad (1)$$

$$\mathbf{q}_{\text{loc}} = [\bar{u} \quad \bar{\theta}_1 \quad \bar{\theta}_2]^T \quad (2)$$

The components of \mathbf{q}_{loc} are obtained according to:

$$\bar{u} = l_n - l_0 \quad (3)$$

$$\bar{\theta}_1 = \theta_1 - \alpha \quad (4)$$

$$\bar{\theta}_2 = \theta_2 - \alpha \quad (5)$$

Where l_0, l_n represent the initial and the current length of the element, respectively, while α is the rigid angle of rotation. All the new quantities can be then computed as:

$$l_0 = \left[(x_2 - x_1)^2 + (y_2 - y_1)^2 \right]^{1/2} \quad (6)$$

$$l_n = \left[(x_2 + u_2 - x_1 - u_1)^2 + (y_2 + v_2 - y_1 - v_1)^2 \right]^{1/2} \quad (7)$$

$$\sin \alpha = c_0 s - s_0 c \quad (8)$$

$$\cos \alpha = c_0 c + s_0 s \quad (9)$$

with:

$$c_0 = \cos \beta_0 = \frac{1}{l_0} (x_2 - x_1) \quad (10) \quad c = \cos \beta = \frac{1}{l_n} (x_2 + u_2 - x_1 - u_1) \quad (11)$$

$$s_0 = \sin \beta_0 = \frac{1}{l_0} (y_2 - y_1) \quad (12) \quad s = \sin \beta = \frac{1}{l_n} (y_2 + v_2 - y_1 - v_1) \quad (13)$$

The correlation between virtual local and global displacements is reported in Eq. (14).

$$\delta \mathbf{q}_{\text{loc}} = \mathbf{B} \delta \mathbf{q}_{\text{glob}} \quad (14)$$

in which the transformation matrix \mathbf{B} is function of the element current length l_n and angle β :

$$\mathbf{B} = \begin{bmatrix} -c & -s & 0 & c & s & 0 \\ -s/l_n & c/l_n & 1 & s/l_n & -c/l_n & 0 \\ -s/l_n & c/l_n & 0 & s/l_n & -c/l_n & 1 \end{bmatrix} \quad (15)$$

After having introduced the relation between the local and the global virtual displacements through the definition of the transformation \mathbf{B} matrix, it is then possible to obtain the correlation between the local value of the internal forces \mathbf{f}_{loc} and local tangent stiffness matrix \mathbf{K}_{loc} and the corresponding global quantities, \mathbf{f}_{glob} and \mathbf{K}_{glob} . By exploiting the virtual work principle in both local and global reference systems and by using Eq. (14), the relation between \mathbf{f}_{loc} and \mathbf{f}_{glob} leads:

$$\mathbf{f}_{\text{glob}} = \mathbf{B}^T \mathbf{f}_{\text{loc}} \quad (16)$$

where the internal local forces that defines \mathbf{f}_{loc} are:

$$\mathbf{f}_{\text{loc}} = [N \quad M_1 \quad M_2]^T \quad (17)$$

Subsequently, the relation between global and local expression of the tangent stiffness matrix \mathbf{K}_{glob} and \mathbf{K}_{loc} is derived by differentiating Eq. (16) and it yields

$$\mathbf{K}_{\text{glob}} = \mathbf{B}^T \mathbf{K}_{\text{loc}} \mathbf{B} + \frac{\mathbf{z} \mathbf{z}^T}{l_n} N + \frac{I}{l_n^2} (\mathbf{r} \mathbf{z}^T + \mathbf{z} \mathbf{r}^T) \cdot (M_1 + M_2) \quad (18)$$

in which \mathbf{r} and \mathbf{z} terms Eqs. (19)-(20) are respectively:

$$\mathbf{r} = [-c \quad -s \quad 0 \quad c \quad s \quad 0]^T \quad (19)$$

$$\mathbf{z} = [s \quad -c \quad 0 \quad -s \quad c \quad 0]^T \quad (20)$$

The local force vector \mathbf{f}_{loc} and local tangent stiffness matrix \mathbf{K}_{loc} depend on the specific definition introduced for the local formulation.

2.2 Local formulation

In the previous section the relation between local and global quantities of the force vector and the tangent stiffness matrix were derived. The following step consists in the definition of the local quantities based on the specific choice of the local formulation. As previously mentioned, one of the main advantages of the co-rotational approach is the possibility to adopt different formulations of the local deformations. In this way, it is possible to derive finite elements with different characteristics. On these premises, three different local formulations were then derived:

1. A local Bernoulli beam theory where the strain field is purely linear.

2. A local shallow arch Bernoulli beam theory that includes a low-order nonlinearity in the strain field.
3. A local Timoshenko beam element that takes into account the shear deformation.

2.2.1 Local linear Bernoulli (LLB) element

This formulation is based on the classical Bernoulli beam theory. The expression for the axial and transversal displacement are respectively:

$$u = \frac{x}{L} \bar{u} \quad (21)$$

$$v = x \left(1 - \frac{x}{L} \right)^2 \bar{\theta}_1 + \frac{x^2}{L} \left(\frac{x}{L} - 1 \right) \bar{\theta}_2 \quad (22)$$

According to Bernoulli beam theory the local strain is given by:

$$\varepsilon = \frac{\partial u}{\partial x} - \frac{\partial^2 v}{\partial x^2} y = \frac{\bar{u}}{L} + y \left[\left(\frac{4}{L} - 6 \frac{x}{L^2} \right) \bar{\theta}_1 + \left(\frac{2}{L} - 6 \frac{x}{L^2} \right) \bar{\theta}_2 \right] \quad (23)$$

It is then possible to differentiate the strain.

$$\delta \varepsilon = \frac{\delta \bar{u}}{L} + y \left(\frac{4}{L} - 6 \frac{x}{L^2} \right) \delta \bar{\theta}_1 + y \left(\frac{2}{L} - 6 \frac{x}{L^2} \right) \delta \bar{\theta}_2 = \mathbf{A} \delta \mathbf{q}_{\mathbf{loc}} \quad (24)$$

The internal forces are then computed by introducing the principle of virtual work.

$$V = \delta \mathbf{q}_{\mathbf{loc}}^T \mathbf{f}_{\mathbf{loc}} = \int_V \delta \varepsilon^T \sigma dV \quad (25)$$

That finally leads to:

$$\mathbf{f}_{\mathbf{loc}} = \int_V \mathbf{A}^T \sigma dV \quad (26)$$

The local tangent stiffness matrix is then computed by differentiation of Eq. (26).

$$\mathbf{K}_{\mathbf{loc}} = \int_V \mathbf{A}^T E_n \mathbf{A} dV \quad (27)$$

In Eq. (27) E_n is the tangent modulus that is derived by the integration of the material constitutive law.

2.2.2 Local shallow arch Bernoulli (LSAB) element

The second element employs the same assumptions of the local linear Bernoulli element but with a different definition of the local strain. This element uses an average measure for the axial strain in order to avoid membrane locking, but with a nonlinear definition of the local strain.

$$\begin{aligned}\varepsilon &= \frac{1}{L} \int \left[\frac{\partial u}{\partial x} + \frac{1}{2} \left(\frac{\partial v}{\partial x} \right)^2 \right] dx - \frac{\partial^2 v}{\partial x^2} y = \\ &= \frac{\bar{u}}{L} + \frac{1}{15} \bar{\theta}_1^2 - \frac{1}{30} \bar{\theta}_1 \bar{\theta}_2 + \frac{1}{15} \bar{\theta}_2^2 + y \left[\left(\frac{4}{L} - 6 \frac{x}{L^2} \right) \bar{\theta}_1 + \left(\frac{2}{L} - 6 \frac{x}{L^2} \right) \bar{\theta}_2 \right]\end{aligned}\quad (28)$$

By now differentiating the strain:

$$\begin{aligned}\delta\varepsilon &= \frac{\delta\bar{u}}{L} + \frac{2}{15} \bar{\theta}_1 \delta\bar{\theta}_1 - \frac{1}{30} \bar{\theta}_1 \delta\bar{\theta}_2 - \frac{1}{30} \bar{\theta}_2 \delta\bar{\theta}_1 + \frac{2}{15} \bar{\theta}_2 \delta\bar{\theta}_2 + \dots \\ &\dots + y \left[\left(\frac{4}{L} - 6 \frac{x}{L^2} \right) \delta\bar{\theta}_1 + \left(\frac{2}{L} - 6 \frac{x}{L^2} \right) \delta\bar{\theta}_2 \right] = \mathbf{A} \delta\mathbf{q}_{\text{loc}}\end{aligned}\quad (29)$$

By using the virtual work as in Section 2.2.1, it is obtained:

$$\mathbf{f}_{\text{loc}} = \int_V \mathbf{A}^T \sigma \, dV \quad (30)$$

The derivation of the local quantities for the shallow arch local element follows what already described in the previous paragraph 2.2.1 for the local linear Bernoulli element.

The local tangent stiffness matrix is again computed by differentiation of Eq. (30):

$$\delta\mathbf{f}_{\text{loc}} = \int_V \mathbf{A}^T \delta\sigma \, dV + \int_V \delta \left(\mathbf{A}^T \sigma \right) dV \quad (31)$$

By taking into account that $\delta\sigma = E_n \delta\varepsilon$ the previous equation can be reformulated as:

$$\delta\mathbf{f}_{\text{loc}} = \int_V \mathbf{A}^T E_n \mathbf{A} \delta\mathbf{q}_{\text{loc}} \, dV + \int_V \mathbf{L} \sigma \delta\mathbf{q}_{\text{loc}} \, dV \quad (32)$$

with the substantial difference that, due to a different definition of the local strain, the \mathbf{L} matrix has now to be introduced. It gives:

$$\mathbf{K}_{\text{loc}} = \int_V \mathbf{A}^T E_n \mathbf{A} \, dV + \int_V \mathbf{L} \sigma \, dV \quad (33)$$

with:

$$\mathbf{L} = \begin{bmatrix} 0 & 0 & 0 \\ 0 & 2/15 & -1/30 \\ 0 & -1/30 & 2/15 \end{bmatrix} \quad (34)$$

2.2.3 Local linear Timoshenko (LLT) element

The third formulation is based on Timoshenko beam theory in which the effect of shear deformation γ is included. Linear interpolations are used for all quantities. Since the transversal displacements are zeros at the nodes, this implies that v is zero along the element.

$$u = \frac{x}{L} \bar{u} \quad (35)$$

$$v = 0 \quad (36)$$

$$\theta = \left(1 - \frac{x}{L}\right) \bar{\theta}_1 + \frac{x}{L} \bar{\theta}_2 \quad (37)$$

The local strain and shear deformation are defined as:

$$\varepsilon = \frac{\partial u}{\partial x} - \frac{\partial \theta}{\partial x} y \quad (38)$$

$$\gamma = \frac{\partial v}{\partial x} - \theta \quad (39)$$

In order to avoid shear locking, one Gauss point located in the midpoint of the length is used.

Differentiation of Eqs. (38)-(39) gives:

$$\begin{Bmatrix} \delta \varepsilon \\ \delta \gamma \end{Bmatrix} = \mathbf{A} \delta \mathbf{q}_{\text{loc}} \quad (40)$$

with:

$$\mathbf{A} = \begin{bmatrix} 1/L & y/L & -y/L \\ 0 & -1/2 & -1/2 \end{bmatrix} \quad (41)$$

By using the same procedure as for the LLB element, the local quantities read:

$$\mathbf{f}_{\text{loc}} = \int_V \mathbf{A}^T \begin{Bmatrix} \sigma \\ \tau \end{Bmatrix} dV \quad (42)$$

$$\mathbf{K}_{\text{loc}} = \int_V \mathbf{A}^T \mathbf{C}_n \mathbf{A} dV \quad (43)$$

Where the tangent operator \mathbf{C}_n is defined by:

$$\begin{Bmatrix} \delta\sigma \\ \delta\tau \end{Bmatrix} = \mathbf{C}_n \begin{Bmatrix} \delta\varepsilon \\ \delta\gamma \end{Bmatrix} \quad (44)$$

2.2.4 Constitutive material laws

Both Bernoulli local formulations rely on uniaxial constitutive material laws. Typical stress-strain relationships assumed in the design of steel structures are: elastic-perfectly plastic behaviour, elastic-plastic behaviour with isotropic or kinematic hardening. In this respect, the integration of the material constitutive law to obtain the local force vector and the tangent stiffness matrix is performed by means of the classical numerical integration according to Gauss quadrature. For a uniaxial constitutive material law no iterations are needed at the Gauss point level and the element was developed to allow the user to select from two up to five Gauss integration points along the element length and up to fifteen points at the cross-sectional level. This allows taking into account the plasticity diffusion with a different order of precision. Conversely, for the Timoshenko formulation a yield surface has to be defined. The Von Mises criterion is a typical choice for carbon steel with elastic-perfectly plastic behaviour or with an elastic-plastic behaviour with isotropic/kinematic hardening. Iteration at the Gauss point level can be avoided by using a forward-Euler scheme. However, an implicit scheme was preferred and the backward-Euler scheme strategy [18] was implemented because it generates a consistent tangent operator which maintains the quadratic convergence of the Newton-Raphson method used to attain equilibrium at the structure level. The scheme was applied using plane stress conditions with zero transversal normal stresses and associative plasticity typical of metallic materials.

In Section 3, the effect of the temperature on the integration of the material constitutive laws is described in depth.

3 THE THERMOMECHANICAL PROBLEM AND THE BEHAVIOUR OF STEEL AT HIGH TEMPERATURE

In the previous paragraph, the co-rotational beam formulation was introduced in order to describe the principles of beam kinematics and the derivation of the local and the global expressions of the internal force vector and the stiffness tangent matrix. Under this form, the finite element is potentially able to perform nonlinear analysis by taking into account geometrical and material nonlinearity at ambient temperature. The purpose is now to extend the field of application of the finite element by introducing the effects of temperature for the numerical analysis of steel structures.

3.1 Thermomechanical capabilities

The thermo-structure interaction problem is described by the coupling between the mechanical behaviour and the heat transfer problem. In general, these two phenomena are fully coupled: that is the solution of the temperature field depends on the displacement field and vice versa [19]. In the context of structural fire engineering, the structural response can be considered in most cases with good approximation as static even though dynamic effects may occur near the collapse. The most obvious coupling is related to the effect of the temperature field in the cross section on the displacement field, e.g. thermal expansion. Nevertheless, coupling in the opposite way may also occur. In fact, the thermal loads, i.e. temperatures and heat fluxes, can depend on the displacement field. For instance, this situation can arise when a beam undergoes large displacements in a compartment where the temperature is not uniform owing to a localised fire. Thus, the change of the beam position in the compartment can vary its thermal exposure and consequently the temperature field in the cross section. However, this coupling phenomenon is commonly discarded in structural fire design. Moreover, the heat generation due to strain rate, which is important for micro-scale applications, represents another term that couples the two phenomena but it is negligible for large-scale problems. On these premises, the heat transfer analysis becomes decoupled from the mechanical response and it can be computed first. As a result, the thermo-structure problem is solved sequentially. In this framework, the developed beam FE is able to analyse the nonlinear static mechanical response based on a predetermined temperature field, that can vary with time, in the beam cross-section.

3.2 Integration of the steel constitutive law at high temperature

With reference to the uniaxial material constitutive law that describes the behaviour of steel at high temperature, the total strain can be decomposed in:

$$\varepsilon_{tot}(\sigma, T, t) = \varepsilon_{\sigma}(\sigma, T) + \varepsilon_{th}(T) \quad (45)$$

Where in Eq. (45) ε_{tot} represents the total strain that is obtained as the sum of the stress-related strain ε_{σ} and the thermal strain ε_{th} . In general, a term that describes explicitly the creep strain ε_{cr} can be also added. However, we considered that the effect of creep strain was implicitly included in the stress-strain relation as for the EN1993-1-2 [20].

After defining the strain quantities, it is then possible to specify the integration scheme that allows to compute at each new step and for each Gauss integration point the updated value of stress and tangent modulus that allow to derive the new expression of the local internal force vector and the local tangent stiffness matrix. The procedure depends on the specific adopted local formulation. In the case of Local linear Bernoulli element and Shallow arch Bernoulli element the integration of constitutive law was performed on a uniaxial law; for the Local Linear Timoshenko element the material

integration is defined under plane stress conditions by considering a Von Mises yield surface. The proposed models are based on the assumption of isotropic hardening.

For the Bernoulli beam based element the integration of material law is performed on a uniaxial law as depicted in Fig. 2.

Under the effect of temperature the axial strain increment is given by:

$$\Delta \varepsilon = \Delta \varepsilon_{\sigma} + \Delta \varepsilon_{th} \tag{46}$$

Where $\Delta \varepsilon_{\sigma}$ is the strain increment induced by stress while $\Delta \varepsilon_{th}$ is the thermal strain increment that could be expressed as:

$$\Delta \varepsilon_{th} = \alpha_{th} \Delta T = \alpha_{th} (T_{n+1} - T_n) \tag{47}$$

In Eq. (47), α_{th} represents the thermal expansion coefficient, T_n and T_{n+1} respectively the temperature at step n and n+1.

With reference again to Fig. 2, when a thermal increment ΔT is introduced from a converged solution at temperature T_n point (A), the updating procedure that allows to compute the new values of stress and tangent modulus $E_n = d\sigma/d\varepsilon$ at temperature T_{n+1} follows the curve A-B-C. The A-B curve represents the unloading until point B with residual strain ε_{pl} , that is assumed as a reference point in order to process a new loading at temperature T_{n+1} (B-C curve), this choice is set due to the assumption that the plastic strain is not affected by a temperature variation [21]. A similar procedure is also reported in [6]. Point C represents the update value of stress that is obtained at temperature T_{n+1} .

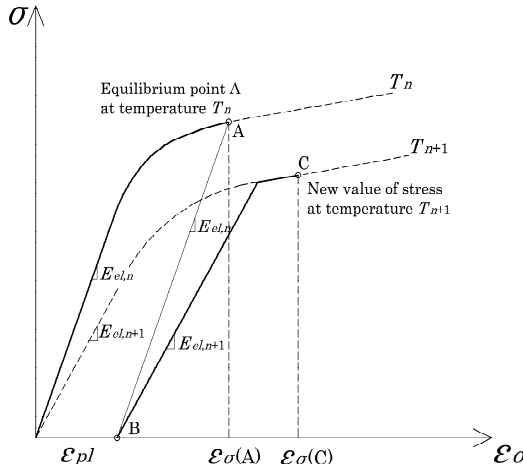


Fig. 2 Integration of material uniaxial constitutive law at high temperature

The plastic rate equations for the Timoshenko beam have to be reformulated because two stresses (σ, τ) and two strains (ε, γ) have to be computed. The general procedure follows the idea exposed for the uniaxial law, but now introducing a planar Von Mises yield function (with $\sigma_y=0$) that referred to temperature T_n is given by:

$$f_n = \sqrt{\left(\sigma_x^2 + 3\tau_{xy}^2\right)} - \sigma_0 \left(\varepsilon_{pl}, T_n\right) \quad (48)$$

where:

$$\sigma_0 = \sigma_{yield} \left(T_n\right) + H \left(T_n\right) \varepsilon_{pl} \quad (49)$$

The term H in Eq. (49) represents the hardening parameter that is function of current temperature and depends on the specific uniaxial stress-strain law that represents material behaviour.

With reference to Fig. 3, the point A on yield surface at temperature T_n represents the equilibrium point of a specific integration point of the structure. The knowledge of elastic properties at temperature T_n allows the unloading until point B characterised by plastic strain ε_{pl} . When an increment of temperature is performed from temperature T_n to temperature T_{n+1} a new yield surface is computed by maintaining also in this case the assumption of plastic strain unaffected by temperature changes. From point B a new loading is performed by now taking into account the updated material properties at temperature T_{n+1} and the effect of thermal dilatation that is here taken into account only for the ε component of strain due to the hydrostatic character of thermal deformation [22]. A new point C is then defined, this could lie inside the yield surface at temperature T_{n+1} or outside; in the second case a backward Euler scheme was adopted to bring back the point on the new computed surface. This procedure allows the generation of a consistent tangent operator which permits to maintain the quadratic convergence of the Newton-Raphson method introduced at the structural level.

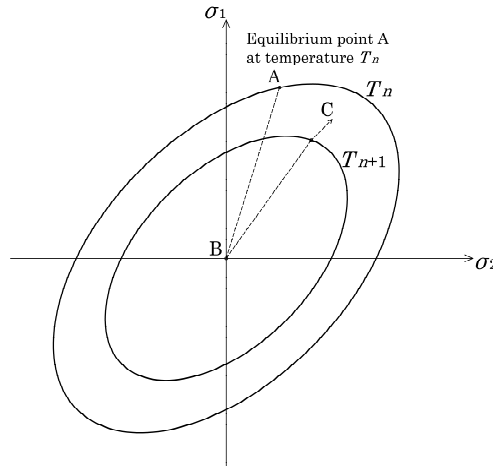


Fig. 3 Integration of material plane stress constitutive law at high temperature. The

yield surface is plotted in the plane of principal stresses

4 PATH FOLLOWING PROCEDURES

The computational analysis of nonlinear structures requires the solution of large systems of nonlinear algebraic equations in order to compute the equilibrium path of the system. At each step, the equilibrium equations are solved by using Newton-Raphson iterations preceded by a predictor [23]. In this context, the purpose of this section is to address two specific issues. The first one is related to the choice of an efficient predictor. The second one is related to the computation of post-buckling paths on the perfect structure, i.e. without introducing imperfections. For that, specific procedures have to be introduced in order to first detect the bifurcation point and then to perform the branch-switching to the secondary path. In commercial FE software this problem is overcome by introducing small geometrical imperfections or alternatively small loads at some specific points. However, with such a method, the instability phenomena cannot be exactly described and the choice of the nature and the amplitude of the imperfections is not always an easy task.

4.1 Displacement predictor

In this section, two displacement predictors are described to increase the efficiency of the structural nonlinear analysis. In fact, in a displacement-based FE code a good displacement predictor can dramatically reduce the number of iterations to achieve convergence. Thus, the objective here is to ensure an improvement in terms of computational cost of the solution through modification of the displacement estimate with which the Newton-Raphson iteration scheme starts at each time step.

As shown in [21] and in Eq. (50) – Predictor 1 - , the Newton-Raphson scheme starts from the solution computed at the last converged equilibrium point, namely the value of the displacement at free DOF nodes.

$$\mathbf{u}_{n+1} = \mathbf{u}_n \quad (50)$$

A first estimate of the solution is computed by means of this trial displacement solution and the norm of the residual, that represents the difference between internal computed forces and external applied loads, is calculated. The norm of the residual is then compared with the tolerance, whose value is selected small enough (e.g. 10^{-4}) to achieve reliable solution. If the check is not satisfied, a corrector Newton-Raphson procedure is implemented in order to obtain the new equilibrium point.

The importance of the displacement predictor is not secondary because an inefficient choice can negatively affect the computational demand. The use of an improved predictor - Predictor 2 - is here proposed and it is based on the simple but reasonable idea that when high nonlinear analyses are performed, the knowledge of the history

pattern of the previously converged solutions is meaningful to estimate the trial equilibrium point. On these premises, Predictor 2 is a linear function of \mathbf{u}_n and \mathbf{u}_{n-1} , as shown in Eq. (51) and Fig. 4

$$\mathbf{u}_{n+1} = \mathbf{u}_n + \frac{t_{n+1} - t_n}{t_n - t_{n-1}} (\mathbf{u}_n - \mathbf{u}_{n-1}) \quad (51)$$

where not only the last converged solution \mathbf{u}_n but also the second last equilibrium point \mathbf{u}_{n-1} is exploited to provide a more realistic value of the trial displacement solution \mathbf{u}_{n+1} .

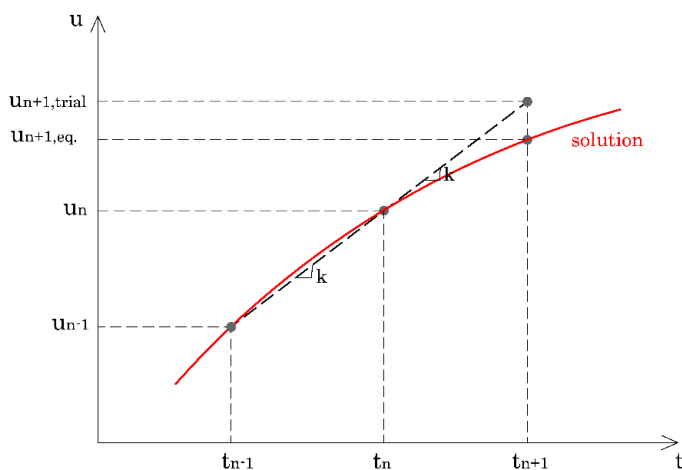


Fig. 4 Scheme of the proposed displacement predictor

The efficiency of the two predictors was numerically tested on two different case studies characterised by a different level of nonlinearity. In both cases, Predictor 2 allowed reducing the computational time with a drastic reduction of the number of iterations that are necessary to achieve convergence.

The results of the simulations are reported in Table 1 and Table 2. The first example is based on a simple supported beam with concentrated load at midspan whose full description can be found in Section 5.1. In this case, the effect of the geometrical nonlinearity was significant because the vertical deflection was approximately equal to $\frac{1}{2}$ of the beam initial span. The use of Predictor 2 implies a reduction of the number of required iterations to achieve the new converged solution of about 60%.

In the second case study (see Section 5.2), the effect of nonlinearity is less evident and the advantage obtained with Predictor 2 is once again significant. In sum, the displacement predictor based on the linear combination of the two previous converged solutions showed better performance in terms of computational demand.

Table 1 Comparison of the efficiency of the two analysed displacement predictors as a function of the number of iterations required to achieve convergence (Case Study 1 - Section 5.1)

No. finite elements	Total number of iterations inside Newton-Raphson corrector procedure		
	Predictor 1	Predictor 2	% Reduction number of iterations
6	10393	4043	61.1
8	10499	4600	56.2
10	10490	4532	56.8
100	10752	5260	51.1

Table 2 Comparison of the efficiency of the two analysed displacement predictors as a function of the number of iterations required to achieve convergence (Case Study 2 - Section 5.2)

No. finite elements	Total number of iterations inside Newton-Raphson corrector procedure		
	Predictor 1	Predictor 2	% Reduction number of iterations
30	3229	1750	45.8
48	3235	1750	45.9
60	3247	1758	45.9

4.2 Branch-switching procedure

The procedure that has been implemented in order to study instability problems of steel compressed members is herein described. This methodology is capable of detecting the presence of critical points along the fundamental equilibrium path and to perform a branch-switching to the secondary path without defining initial geometrical imperfections. This procedure was presented for elastoplastic instability problem in [24] and is now widen to study the instability of compressed structural elements exposed to fire. The idea of the method, initially introduced by Petryk [16], is that along a stable deformation path, the displacements \mathbf{u} correspond to an absolute minimum of the functional J defined by:

$$J = \frac{1}{2} \mathbf{u}^T \mathbf{K} \mathbf{u} - \mathbf{u}^T \mathbf{f}_{\text{ex}} \quad (52)$$

Where \mathbf{K} is the global stiffness matrix and \mathbf{f}_{ex} the vector of the external loads. The critical point is detected by computing the lowest eigenvalues of \mathbf{K} calculated at each converged solution. If one or more negative eigenvalues are present in the diagonal matrix, then it means that the equilibrium point is unstable and that a bifurcation point has been passed. Classical one side bisections can be introduced in order to identify the exact position of the critical point by simply reducing the step size.

Once the critical point is obtained, the first equilibrium point on the secondary path is computed by minimizing J . In order to ensure that the minimisation procedure does not end to the fundamental path, a new predictor $\mathbf{u}_{n+1,\text{BS}}$ is constructed by adding a small perturbation vector to the predictor presented in Eq. (51). In principle, any random perturbation vector can be taken. However, since an eigenvalue analysis has been already performed to determine the bifurcation point, it is judicious to take the eigenvector \mathbf{v} associated to the lowest negative eigenvalue of \mathbf{K} . This gives:

$$\mathbf{u}_{n+1,\text{BS}} = \mathbf{u}_n + \Delta + \frac{\|\Delta\|}{100} \frac{\mathbf{v}}{\|\mathbf{v}\|} \quad (53)$$

with:

$$\Delta = \frac{t_{n+1} - t_n}{t_n - t_{n-1}} (\mathbf{u}_n - \mathbf{u}_{n-1}) \quad (54)$$

The minimization procedure consists in solving at each iteration the nonlinear system:

$$\left(\mathbf{K}^i + \mu \mathbf{I} \right) \Delta \mathbf{u} = -\mathbf{r}^i \quad (55)$$

where \mathbf{I} is the identity matrix, \mathbf{r} is the residual vector while μ is a coefficient that as proposed in [25] can be set equal to either $1.1 \lambda_{\min}$, where λ_{\min} is the lowest eigenvalue of \mathbf{K} , or to 0 if \mathbf{K} is positive definite. At the end of each iteration the displacement is updated by means of:

$$\mathbf{u}^{i+1} = \mathbf{u}^i + \Delta \mathbf{u} \quad (56)$$

The successive equilibrium points on the secondary path are then computed by using Predictor 2 Eq. (51) and classical Newton-Raphson iterations.

5 VALIDATION OF THE BEAM FE

Different meaningful case studies were used to validate the proposed beam FE, as reported in [26, 27, 28, 29, 30]. Case studies 1 and 2 were exploited to assess the capabilities of the beam FE and its different local formulations to capture highly nonlinear problems in steel members caused by thermal exposure. Moreover, in order

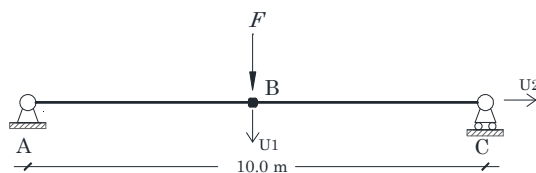
to investigate the potential practical implications of the element, comparison with experimental data [20] is thoroughly described in Case studies 3-5. In all analyses, the maximum strain was limited to 15%, which corresponds to moderate strain.

Table 3 Analysed case studies

	Case study	Analysed problem
1	Simple supported beam	-Comparison between LLB, LSAB and LLT element formulation -Test on displacement predictor -Evaluation of high geometrical nonlinearity -Comparison with ABAQUS [11]
2	L frame	-Introduction of EN1993-1-2 constitutive law for carbon steel at high temperature -Test on displacement predictor -Comparison with SAFIR [7]
3	Rubert Schaumann experimental tests [20] (Simple supported beam)	-Validation against experimental test, example 1 -Comparison with ABAQUS [11]
4	Rubert Schaumann experimental tests [20] (EHR frame)	-Validation against experimental test, example 2
5	Rubert Schaumann experimental tests [20] (EGR frame)	-Validation against experimental test, example 3

5.1 Case study 1: Simple supported beam

The first case study is representative of a simple supported beam with a concentrated load at midspan. The geometry, applied load, cross section and material properties at ambient temperature are reported in Fig. 6a. The ratio between the bending moment M_{ed} at midspan and the plastic moment M_{pl} of the cross section is 0.57. The aim is to highlight the capabilities of the element and its local formulations to capture significant nonlinearities.



Material data at ambient temperature:

$$E = 210\,000 \text{ MPa}$$

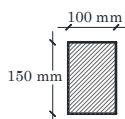
$$E_t = E/100$$

$$f_y = 235 \text{ MPa}$$

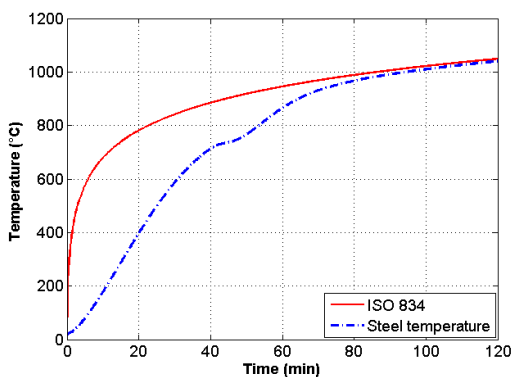
Applied load:

$$F = 30 \text{ kN}$$

$$Med/Mpl = 0.57$$



(a)



(b)

Fig.6 Case study 1: a) geometry and data; b) evolution in time of the temperature in the cross section owing to exposure to the ISO 834 standard heating curve

As illustrated in Fig. 6b, the thermal action on the beams is represented by the ISO 834 standard heating curve. Since the element is not endowed with full thermomechanical capabilities, as described in Section 3, the cross-section temperature distribution, that is assumed to be uniform in the beam, was computed according to the mass lumped concept provided in EN1993-1-2 [15] by considering the section exposed on all sides. The structure was also studied, under the same assumptions, by means of the commercial software ABAQUS [11] using the Bernoulli B23 and the Timoshenko B21 thermomechanical beam elements. In this way, it was possible to meaningfully compare the Bernoulli (Local Linear and Local Shallow Arch) and Timoshenko formulations implemented in the developed FE.

A bilinear material constitutive law with hardening tangent modulus equal to $E_t = E/100$ was used to represent the steel material constitutive law. The degradation of the steel mechanical properties at elevated temperature followed the recommendations given in EN1993-1-2 [15]. A constant thermal expansion coefficient $\alpha_{th} = 1.2 \cdot 10^{-5} \text{ } ^\circ\text{C}^{-1}$ was used.

Fig. 7a and Fig. 7b illustrate the evolution in time of the midspan vertical displacement and of the axial displacement of the node at the roller computed with the LSAB formulation. Twenty LSAB finite elements with two Gauss integration points along the beam length and fifteen in the cross-section height were used. The outcomes showed the ability of the developed finite element to treat problems characterised by high nonlinearities and thermal effects. In particular, the case study highlighted well the geometrical nonlinearity with the final midspan vertical displacement that is in the order of 50% of the initial beam span length. Moreover, good agreement with the predictions of ABAQUS multipurpose software are shown.

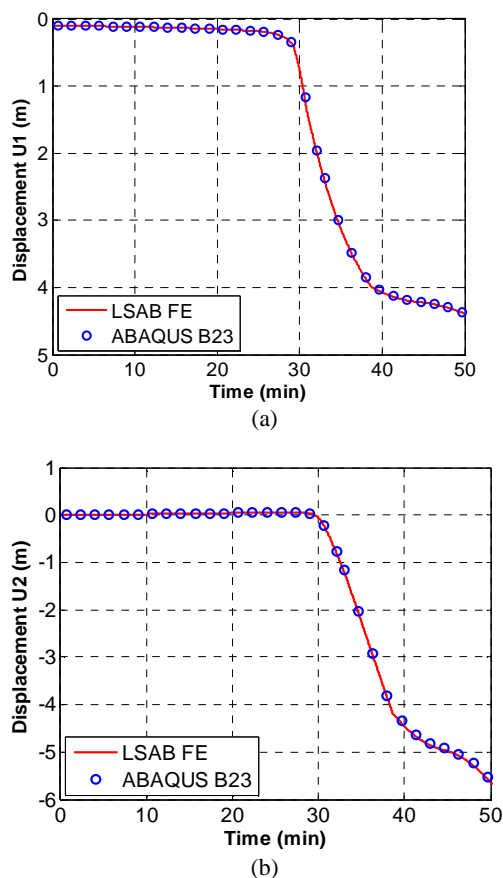


Fig.7 Case study 1 - Comparison between LSAB and ABAQUS B23: a) midspan vertical displacement; b) roller horizontal displacement

Fig. 8a reports the comparison between the LSAB and the LLT elements with the ABAQUS B21 element. Both models used 20 finite elements with fifteen integration points in the cross-section. Fig. 8 shows very good agreement with the results in terms of both vertical displacement and stresses. Indeed, the high slenderness of the beam

implies that the shear deformations are negligible. Thus, the LLT and LSAB solutions are comparable. The values of stress depicted in Fig. 8b were taken at the extreme integration Gauss points of the midspan cross-section.

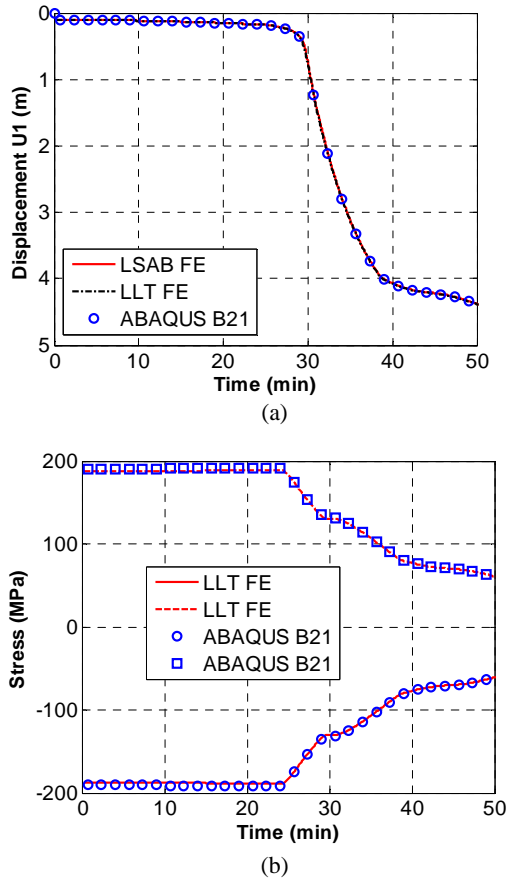


Fig.8 Case study 1: a) comparison between LSAB, LLT and ABAQUS B21 elements referred to vertical midspan displacement; b) values of stress measured at the extreme cross-section integration points for LLT beam element and ABAQUS B21 element

Now, the advantages to take into account low-order nonlinearity in the local strain formulation are investigated. In this respect, Fig. 9 shows the convergence to the reference solution between the LLB and the LSAB elements by changing the number of FE used to discretize the beam: 6 and 10 FE. In particular, the reference solution was computed according to the LSAB formulation with 100 FE, two integration points along the FE length and fifteen Gauss points in the cross section. The results, which are all referred to the midspan vertical displacement, were obtained under the same assumptions. No significant differences were observed between the two formulations

in the initial phase of the fire, whilst greater variations were exhibited when the level of geometrical nonlinearity increased. In addition, from Fig. 9 it is possible to observe that the LSAB model with 10 FE was already able to attain the reference solution whereas by employing the LLB formulation the convergence was slower. The results highlighted that the low-order nonlinear local strain definition introduced in the LSAB formulation provided a more efficient form of the finite element. In fact, this allowed obtaining good predictions with a lower number of finite elements and consequently reducing the computational time of the simulation.

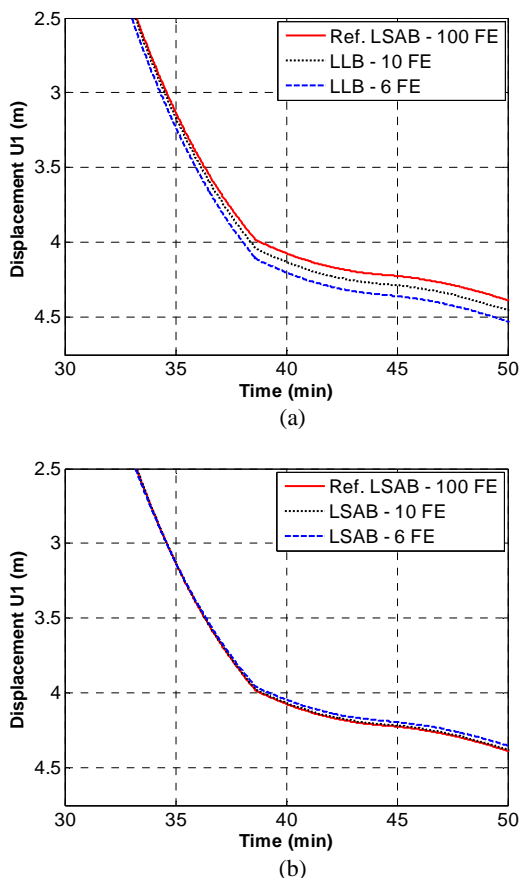


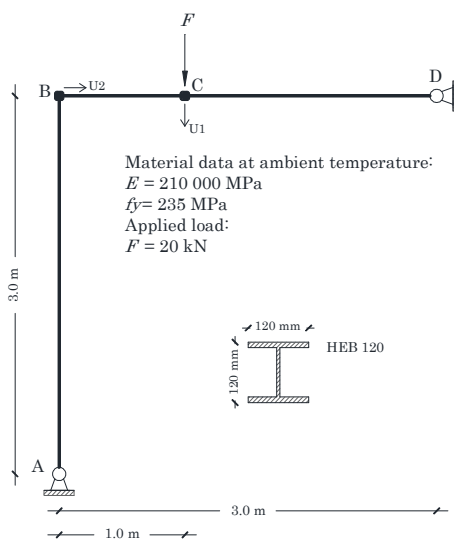
Fig.9 Case Study 1 - Comparison between LLB and LSAB beam element formulation: a) midspan vertical displacement using 6 and 10 LLB FE; b) midspan vertical displacement using 6 and 10 LSAB FE

5.2 Case study 2: L Frame

The aim of Case study 2 is to model a structural frame with steel material properties given in EN1993-1-2 [15] and a realistic member cross-section profile. The model consists of a double hinged, L-shape steel frame whose structural members are made

of an S235 HEB 120 profile. The dimension of the frame and the data are reported in Fig. 10a. A concentrated load force was applied to the beam and was kept constant during the simulation whilst the temperature in the cross section of both the beam and the column was varied according to the evolution in time shown in Fig. 10b. In this respect, the element cross-section temperature was computed with reference to the ISO 834 heating curve applied to all sides. The temperature distribution was assumed uniform in the cross section.

The computer program SAFIR [7] was used for the validation. It was specifically conceived for the numerical analysis of structures in fire. Its beam element is a fibre-based Bernoulli element. A fibre formulation was used because SAFIR is able to also solve the heat transfer problem in a sequential way. In order to have a consistent comparison, the same uniform temperature evolution (see Fig. 10b) was imposed to the SAFIR beam element cross-section that was composed of an adequate number of fibres. 60 LSAB FEs with fifteen Gauss integration points in the cross section and two integration points along the FE length were used to model the L-frame. The stress-strain relation of carbon steel at elevated temperature and the relative reduction factors of mechanical properties as well as the steel relative elongation provided by EN1993-1-2 [15] were employed in the analysis, as illustrated in Fig. 11.



(a)

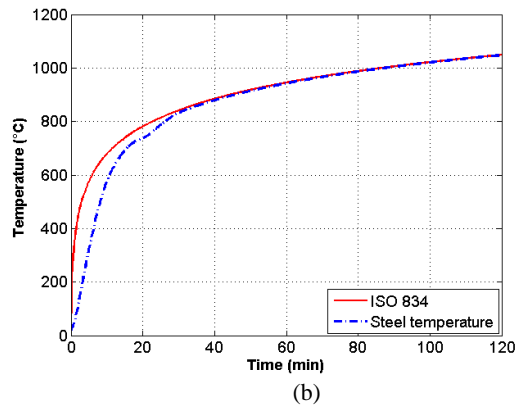


Fig.10 Case study 2: a) geometry and data; b) evolution in time of the cross-section temperature under the ISO 834 standard heating curve

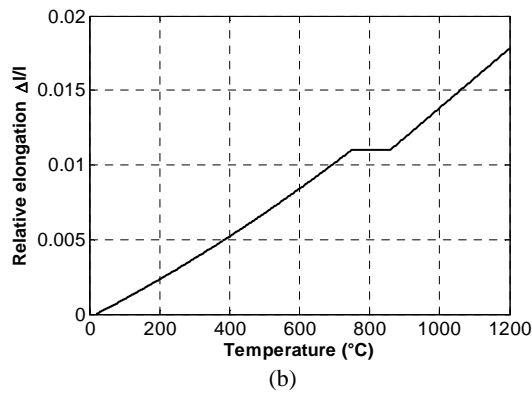
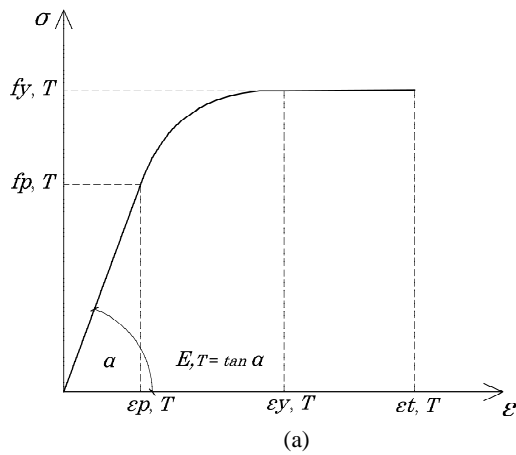


Fig. 11. Material properties of carbon steel at elevated temperature: a) stress-strain relation b) relative thermal elongation [15]

Fig. 12 shows the results of the analysis in term of vertical displacement of point C and horizontal displacement of point B. Very good agreement is exhibited between the two models that provided the same time of collapse. Thus, the outcomes reveal that the proposed FE is promising in modelling of steel structures in fire.

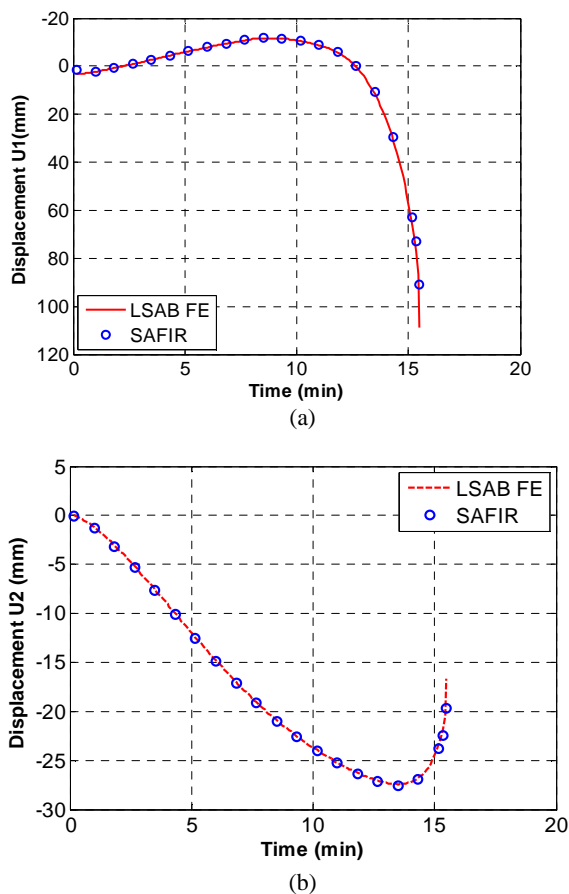


Fig. 12 Case study 2 – Comparison with SAFIR: a) vertical displacement at C; b) horizontal displacement at B

5.3 Validation against experimental data

A series of comparisons against experimental tests is hereinafter described to show how the developed FE is able to predict then real behaviour of steel structures exposed to fire. In particular, the tests conducted by Rubert and Schaumann [20] were exploited. They have been used as validation benchmark by several other researchers [6,26,27,28,29,30]. All transient-state tests are referred to two-dimensional steel frames under the combined action of mechanical and thermal loads.

5.3.1 Simple supported beam

The first test consists of a simple supported beam with concentrated load at midspan subjected to a ramp increase of temperature [20]. The specimen geometry and the steel material properties at ambient temperature are reported in Fig. 13a.

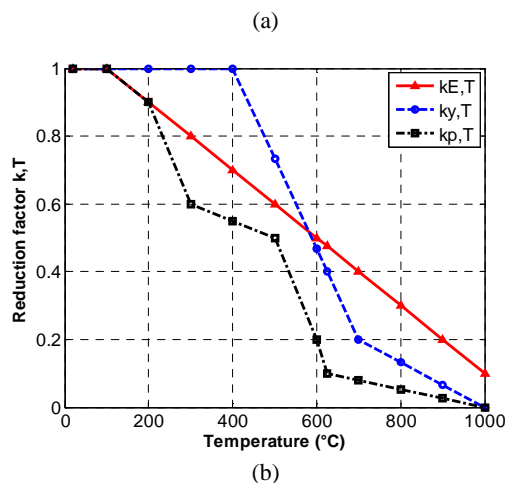
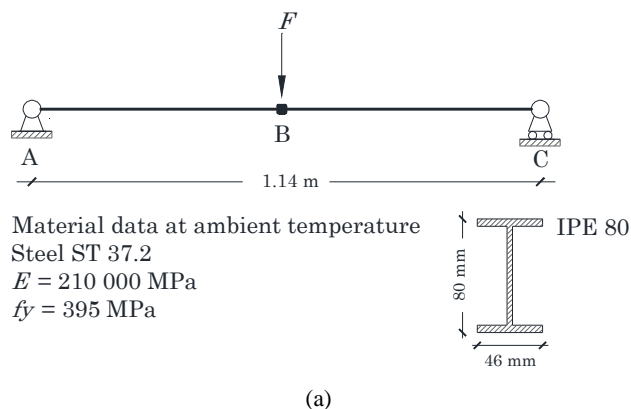


Fig. 13 Rubert and Schaumann test on simple supported beam: a) specimen set-up b) Rubert – Schaumann reduction factors for steel at high temperature [20]

The load was assumed to be constant in time and it was selected based on two different utilization factors $F/F_u = 0.2$ and 0.5 – which represent the ratio of the actual load to the ultimate load bearing capacity at ambient temperature. The heating rate steel temperature in the cross section was imposed equal to 2.67 °C/min according to the authors' recommendations. This value was approximated to be uniform throughout the beam length and the cross-section height as suggested by the measures performed during the tests via electronic temperature control system.

The EN 1993-1-2 temperature dependent stress-strain relationship [15] was used to integrate the material properties whereas the degradation of the initial modulus of elasticity E , the proportional limit f_p and the yield point f_y were assumed in accordance with the authors' guidance, as illustrated in Fig. 13b. It allowed, for this particular case, to obtain better results in the validation process.

Twenty LSAB finite elements with two Gauss integration points along the beam length and fifteen in the cross-section height were used.

The results of the numerical calibration are finally reported in Fig. 14a and Fig. 14b for the two utilization factors F/F_u . Very good results were obtained by comparing the numerical results obtained with LSAB FE and experimental tests as well as with the ABAQUS B23 element.

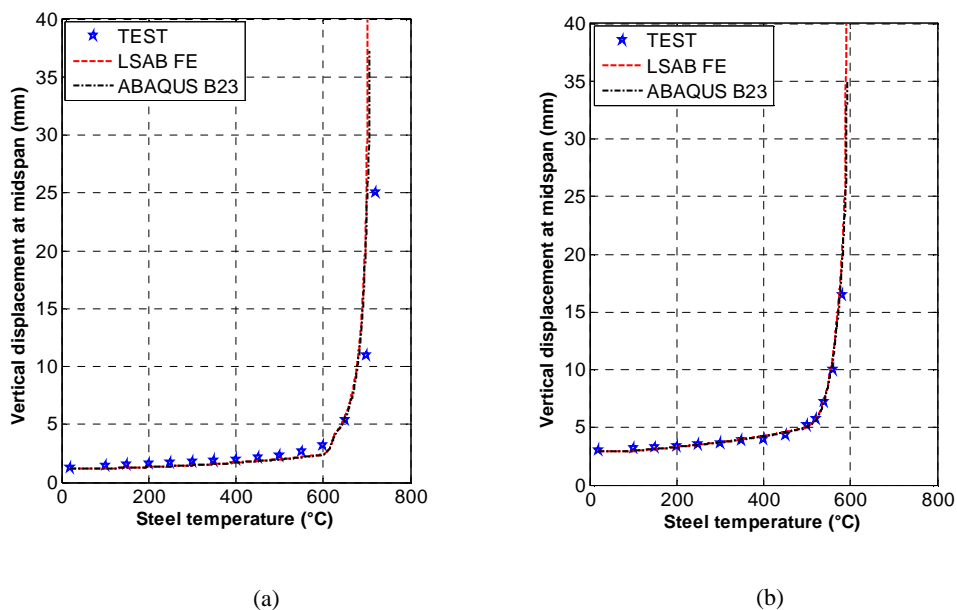


Fig. 14 Comparison of Rubert and Schaumann simple supported beam tests with finite element predictions: a) $F/F_u=0.20$ b) $F/F_u=0.50$

5.3.2 EHR frame

The second experimental test, referred as EHR series [20], was an L frame composed of IPE80 profiles and exposed to the ISO 834 standard heating curve, as shown in Fig. 15. The steel mechanical properties used in the numerical simulation are the same as the ones described in Section 5.3.1. Forty LSAB finite elements with two Gauss integration points along the finite element length and fifteen in the cross-section height were employed.

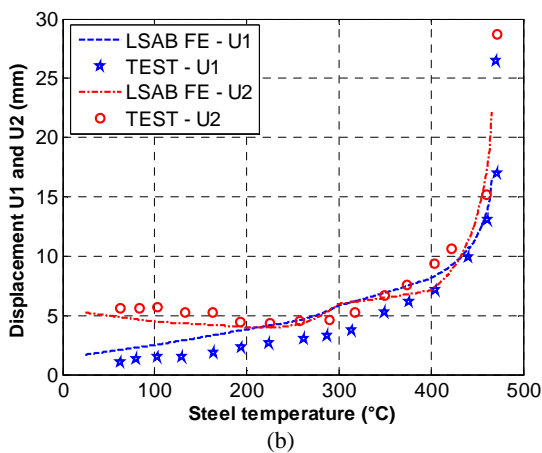
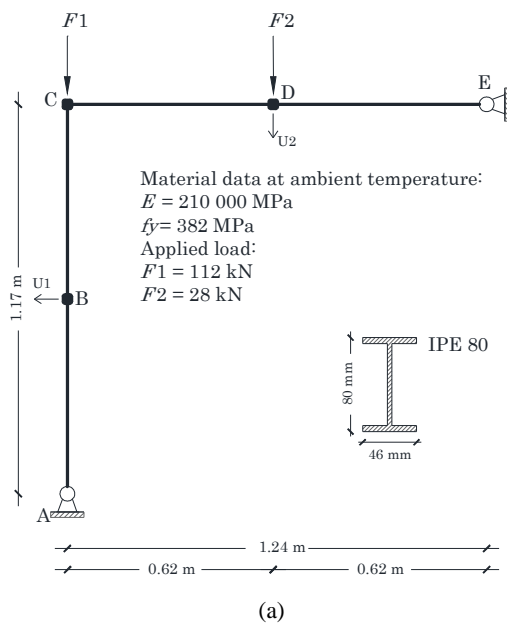


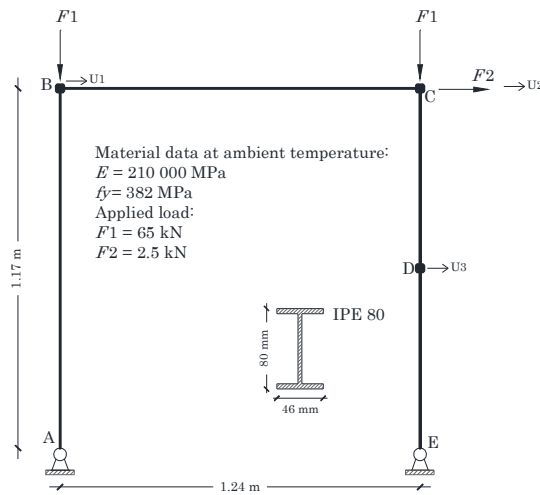
Fig. 15 Comparison of Rubert Schaumann EHR test with finite element predictions: a) geometry of the EHR frame b) evolution of U1 and U2 displacements as a function of the steel temperature

Also for this case study, the results reported in Fig 15b showed reasonably good agreement with the experimental evidences. In particular, the critical temperature obtained through the numerical simulation was close to that observed experimentally: $T_{num}=466^{\circ}\text{C}$ vs. $T_{test}=475^{\circ}\text{C}$, which entailed an error of less than 2%. The value of the critical temperature was estimated in correspondence to asymptote that intervened at the end of the test and of the numerical simulation.

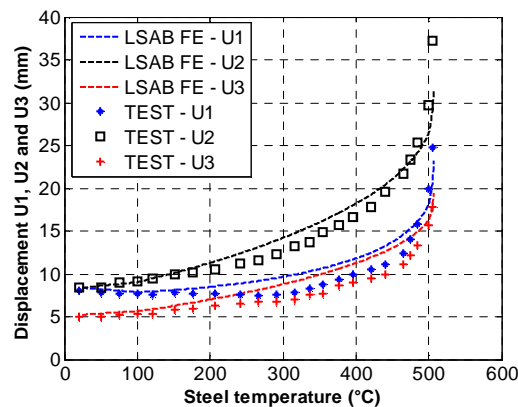
5.3.3 EGR frame

A third experimental test with a new geometrical and load configuration was finally investigated [20]. The same assumptions for the steel material properties reported in sections 5.3.1 and 5.3.2 were made. The geometry of the steel frame with the applied loads and the problem data are reported in Fig. 16a. Sixty LSAB finite elements with two Gauss integration points along the finite element length and fifteen in the cross-section height were introduced.

The value of displacements observed experimentally at node B, C and D were compared with the numerical results and both the displacement evolution and the critical temperature were well predicted by the LSAB FE.



(a)



(b)

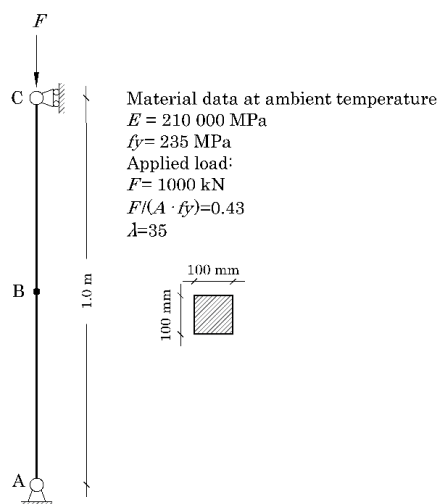
Fig. 16 Comparison of Rubert and Schaumann tests with finite element predictions: a) EGR frame; b) comparison of U1 U2 and U3 displacements at B

The validation process of the proposed beam FE against both available commercial software and experimental data showed good and promising outcomes. The mechanical response has been always predicted with good accuracy. The introduction of a low-order nonlinearity in the local formulation of the LSAB is beneficial for achieving convergence with a lower number of elements and consequently with lower computational demand.

6 INSTABILITY ANALYSIS OF STEEL STRUCTURES EXPOSED TO FIRE

6.1 Case Study 1: Axially loaded column

The capabilities of the branch-switching procedure described in Section 4.2 to analyse instability problems of steel structures exposed to fire were initially proved by investigating a simple case study of flexural buckling of a compressed column whose geometry, cross section, slenderness λ and material steel property at ambient temperature are reported in Fig. 17a. The simulation was performed with twenty LSAB finite elements, fifteen Gauss integration points in the cross section and two integration points along the finite element length. In order to check the accuracy of the analysis, a comparison with an equivalent ABAQUS model was made. The evolution in time of the steel temperature, which is uniform in the cross section, is reported in Fig. 17b and it is based on the standard heating curve exposure. The steel stress-strain relation as well as the reduction factors of the mechanical properties were assumed according to the EN1993-1-2 [15].



(a)

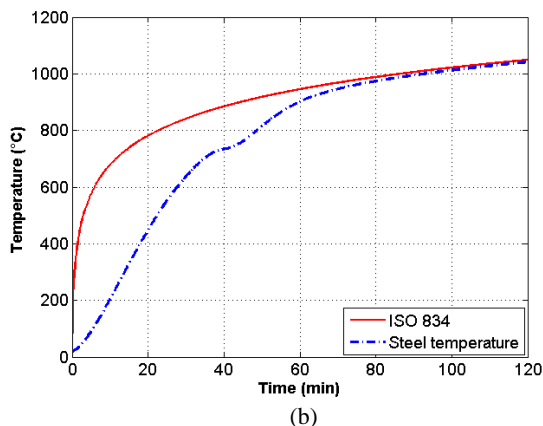


Fig.17 Compressed column subjected to instability: a) geometry b) cross-section temperature under the ISO 834 standard heating curve

The analysis showed that the section exhibited first plastic strains at $t = 17$ min and 48s that corresponded to a steel temperature of 397.4 °C. At this step, the value of the proportional limit f_p is below 100 MPa, which is the applied compressive stress. Moreover, the value of the tangent modulus reduced progressively owing to the combined effect of strain and temperature increase. The critical point was identified at $t = 24.0$ min with steel temperature equal to 533.7 °C. For this value of temperature, the tangent modulus E_n is 12180 MPa, which is very closed the theoretical buckling value computed according to the Euler critical load that reads:

$$E_{cr} = \frac{Fl^2}{\pi^2 I} \cong 12159 \text{ MPa} \quad (57)$$

After this point, the new solution was obtained by using the minimization procedure described in Section 4.2 and the secondary equilibrium path was then followed. The results of the analysis are shown in Fig. 18 and Fig. 19, where the critical load and the point of branch switching are clearly identified. Thus, the secondary equilibrium path was well captured and followed. This suggests that the implementation of the branch-switching procedure to study the behaviour of structural elements subjected to elevated temperature has been successful. Then, the same case study was finally performed with the procedure that is commonly used in commercial finite element software, which consists in introducing an arbitrary lateral force or, alternatively, in modifying the geometry of the problem by means of an initial geometrical imperfection. As a result, a lateral force was introduced at the midspan node B and its initial value was chosen adequately small - $1/1000 F$ or $1/2000 F$ -. An analogous analysis with an equivalent ABAQUS model of the column composed of 20 B23 elements was also carried out.

The comparison of the two procedures highlighted some advantages that are intrinsic of the implemented path-following technique. Firstly, the solution obtained with ABAQUS software exhibited an initial transversal displacement for the effect of the lateral force necessary to force instability, which was not present in the ideal case where the perfect column was only subjected to the compression load. During the analysis, the transversal displacement increased for the combined effects of plasticity and of thermal action that progressively reduced the mechanical properties. Conversely, by employing the branch-switching procedure the column exhibited only axial displacements until the critical point that marked bifurcation to the secondary equilibrium path. Fig. 18 and Fig. 19 also show that the solution obtained with branch switching procedure represents an asymptotic solution of the analyses with lateral forces whose presence is necessary only to force instability.

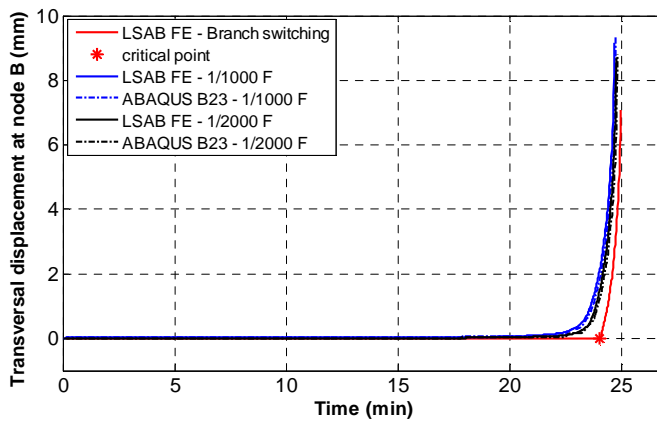


Fig.18 Compressed column: transversal displacement at node B

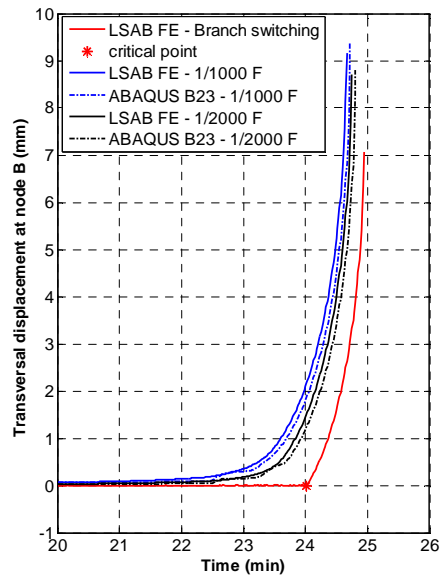


Fig.19 Compressed column: enlargement of transversal displacement at node B between 20-26 min

6.2 Case Study 2: Axially loaded portal frame

The second case study is based on a portal frame whose columns are loaded with identical vertical concentrated load. The geometry, cross section and material properties at ambient temperature are reported in Fig. 20a, whereas in Fig. 20b the evolution in time of the temperature in the cross section under the ISO 834 standard heating curve is illustrated.

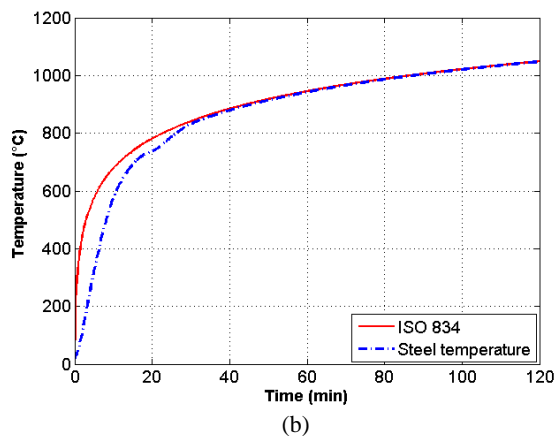
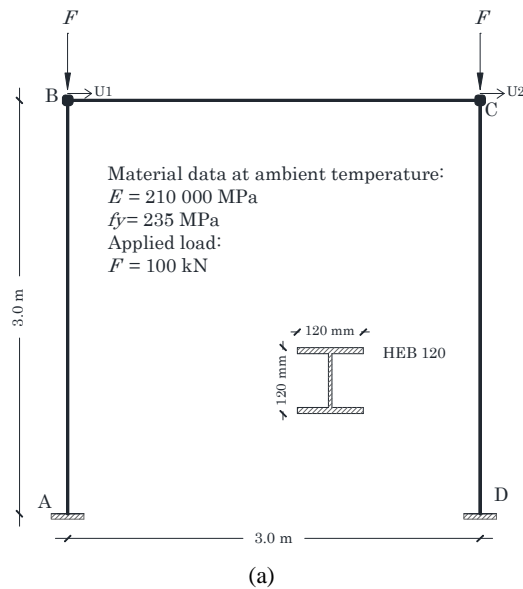
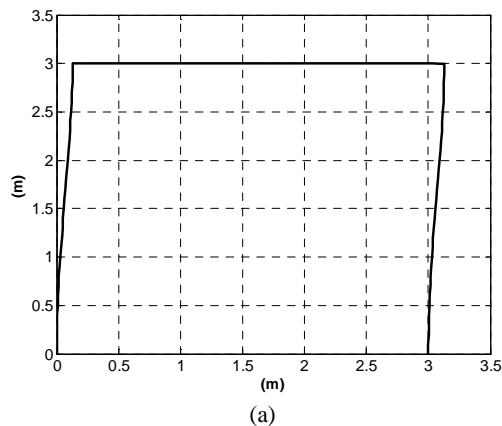


Fig.20 Portal frame: a) geometry; b) cross-section temperature under ISO 834 standard heating curve

The model was made of a fine mesh based on ninety LSAB FE, fifteen gauss integration points in the cross section and two integration points along the element length. With fifteen Gauss points the full cross-section plasticization could be captured. The comparison of results was performed by means of an equivalent ABAQUS model composed of B23 finite element that included horizontal forces of magnitude $1/500 F$ and $1/1000 F$, respectively, applied rightward at node B. In both models, the steel material properties are those given in EN1993-1-2 [15].

The analysis showed that the critical bifurcation point was reached after 13 min and 54s that corresponded to a value of steel temperature equal to 673.3 °C. At this time step, a negative eigenvalue was found in the diagonal of the eigenvalue matrix related to the stiffness matrix of the structure obtained at the last equilibrium point. The branch-switching procedure then proceeded by introducing a perturbation vector that contained the eigenvector associated with the most negative eigenvalue of the stiffness matrix \mathbf{K} whose shape is depicted in Fig. 21a.

Unlike the case of the axially compressed column in which the displacement up to the critical point is limited to the axial component, here the effect of thermal dilatation produced the deformed shape represented in Fig. 21b. The modified displacement predictor, based on branch switching, acted on this deformed configuration by introducing a perturbation that successively produced the collapse of the structure due to instability. As a result, this procedure has the major advantage to detect possible bifurcation points of a structural system that is subjected to both mechanical and thermal loads. In fact, since the thermal loads typically vary with time also the buckling modes do, because of the thermal effect on the structure, e.g. thermal expansion, possible load redistribution, loss of stiffness etc. Thus, for a generic thermal exposure, the buckling mode shapes at ambient temperature are different from those at elevated temperature and it can be extremely difficult to foresee them a priori. A linear buckling analysis performed at ambient temperature to identify the initial imperfections to be introduced into the model could be even misleading. Conversely, the proposed FE has shown the ability to overcome this issue. In Fig. 22 the results in terms of displacement evolution is shown. It is possible to observe that the branch-switching procedure predicted the bifurcation point and the elastic-plastic instability failure mode owing to thermal exposure without the need to explicitly model the initial imperfections. Fig. 22 also includes the comparison with the ABAQUS model and the LSAB FE model with initial horizontal forces. As expected, the branch switching occurred suddenly, whereas when horizontal forces were applied the instability intervened with smoother transition.



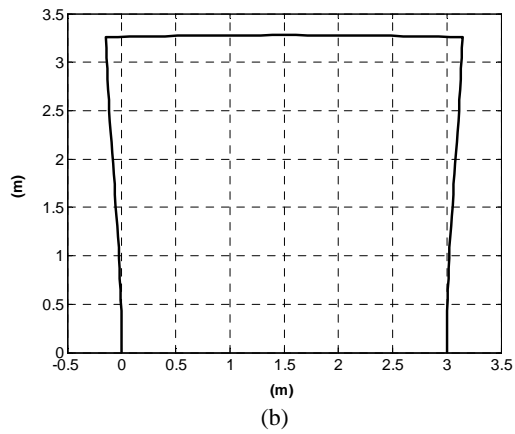
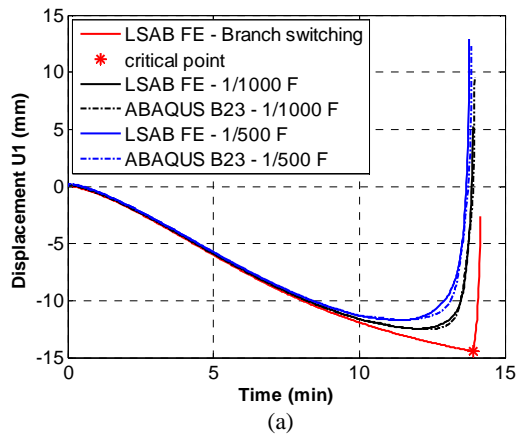


Fig. 21 Portal frame: a) eigenvector shape associated to the minimum eigenvalue registered at the critical point; b) deformed shape at critical point (scale 10x)



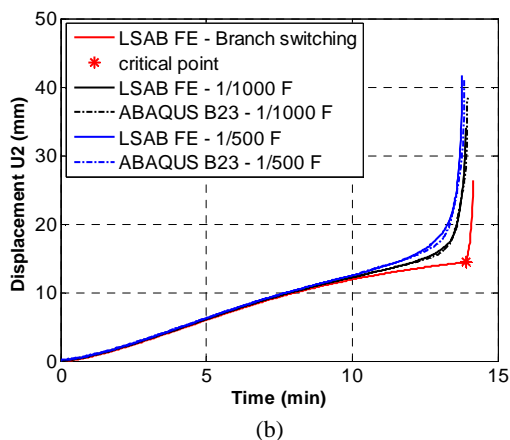


Fig. 22 Instability analysis of a heated portal frame: a) U1 displacement; b) U2 displacement

6.3 Parametric analysis and comparison with the buckling curve of EN1993-1-2

In Section 6.1 and 6.2, it was shown that the implementation of the branch-switching procedure in the proposed FE was fulfilled for analysing instability of steel structural systems exposed to fire without including initial geometrical imperfections. In Section 5.3 it was shown that the developed FE is able to well reproduce experimental outcomes, here, further practical implications of the procedure will be emphasised. In fact, the advantage to avoid the explicit modelling of the geometrical imperfections is clear: no need to assume the shape and the amplitude of the imperfections that also implies a reduced model complexity. However, this benefit becomes fully effective if it can be applied in practice to simulate instability problems of real steel structural members. On these premises, the capabilities of the branch-switching procedure of predicting the flexural buckling curve provided in EN1993-1-2 [15] relatively to the behaviour of Class 1, 2 or 3 compression steel members in fire are investigated. The EN1993-1-2 buckling curve accounts for geometrical ($h/1000$ where h is the member height) and mechanical imperfections (residual stresses) [31] and it provides the reduction factor for flexural buckling in fire condition χ_{fi} as a function of the relative slenderness at high temperature λ_{fi} . Therefore, the idea is to reproduce the EN1993-1-2 flexural buckling curve by means of a parametric analysis by employing the proposed FE applied to compression steel members. As a result, a pinned-pinned HEB100 profile was selected and loaded with a constant axial compression load N equal to 116.6 kN which corresponds to $N/A f_y = 0.20$, where A is the area of the cross section. The steel grade was an S235 that implied a Class 1 cross-section classification in fire conditions [15]. The EN1993-1-2 material properties of carbon steel [15] were used. A uniform and linearly increasing temperature characterised by heating rate of 2.67 °C/min was

assigned to the cross section. Then, several analyses with varying member length from 0.5 m to 6 m were carried out to cover a wide range of relative slenderness in fire condition. At the end of each analysis, which corresponded to member failure, the steel temperature T_{cr} was recorded and the flexural buckling reduction factor was computed according to Eq. (58)

$$\chi_{fi} = \frac{N}{k_{y,T} f_y A} \quad (58)$$

Where N is the applied load, $k_{y,T}$ is the reduction factor of the effective yield strength at the critical temperature T_{cr} , f_y is the yield strength at ambient temperature and A is the cross-section area. The comparison with the EN1993-1-2 buckling curve is shown in Fig. 23 and it suggests that the FE with branch-switching capabilities is indeed promising in predicting the buckling strength at elevated temperature of steel compressed H elements. This valuable characteristic enhances the applicability domain of the proposed FE to the design practice that could rely on models without geometrical imperfections to simulate the buckling behaviour of steel structures at elevated temperature.

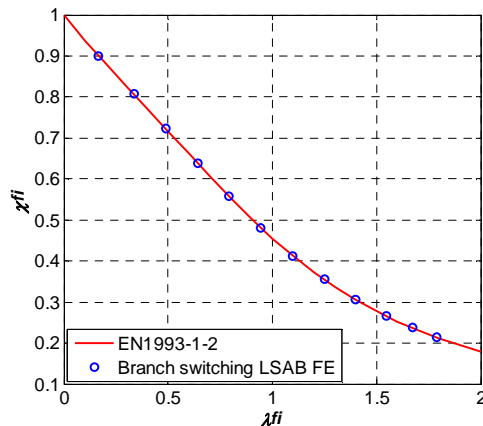


Fig. 23 Comparison between the buckling curve of EN1993-1-2 and buckling reduction factors obtained with the proposed FE

7 CONCLUSIONS

The paper described the development of a co-rotational two-dimensional beam element to study the behaviour of steel structures exposed to fire and in particular instability problems in the elastic-plastic range. Different local formulations were implemented. Validation against experimental data and numerical simulations carried out with commercial software, such as ABAQUS and SAFIR, was performed and showed good agreement. Moreover, an improved displacement predictor based on the linear

combination of the two previous converged solutions was proposed. It allowed faster convergence with a significant decrease in the number of iterations - up to about 60% - with respect to a displacement predictor based on the previous converged solution only.

A branch-switching procedure capable of analysing instability problems in elastic-plasticity of steel structures by detecting bifurcation points of secondary equilibrium paths without explicitly including initial geometrical imperfections was successfully implemented. This entails a benefit in terms of practical implications in the context of structural fire FE modelling. First, since there is no need to explicitly introduce the geometrical imperfections to detect critical points, the geometry of the structural model is less complex. In addition, no assumptions on the amplitude of the imperfections have to be made. Then, critical bifurcation points that depend on the actual distribution of mechanical loads and temperatures in the elements at each converged solution can be identified. This implies a major advantage for the analysis of steel structures in fire for which, in general, the buckling mode shapes vary with time and consequently any introduced imperfections based on buckling analysis at ambient temperature may not be representative of the actual behaviour at elevated temperature. Furthermore, the proposed FE element was able to reproduce the flexural buckling curve of EN1993-1-2 for H steel compressed elements without including imperfections. This characteristic suggests that the FE can predict the buckling strength of real steel members in compression, which is an important added value for design applications.

Future works will be addressed to extend this procedure to develop 3D beam elements and shell elements with thermomechanical capabilities.

References

- [1] Liu T.C.H., Fahad M.K., Davies J.M., *Experimental investigation of behaviour of axially restrained steel beams in fire*, Journal of Constructional Steel Research (2002); 58: 1211-1230
- [2] Yin Y.Z., Wang Y.C., *A numerical study of large deflection behaviour of restrained steel beams at elevated temperatures*, Journal of Constructional Steel Research (2004); 60: 1029-1047
- [3] Bailey C.G., *Membrane action of slab/beam composite floor systems in fire*, Engineering Structures (2004); 26: 1691-1703
- [4] Li Guo-Qiang, Guo Shi-Xiong, Zhou Hao-Sheng, *Modeling of membrane action in floor slabs subjected to fire*, Engineering Structures (2007); 29: 880-887
- [5] Tan K.H., Ting S.K., Huang Z.F., *Visco-elasto-plastic analysis of steel frames in fire*, Journal of Structural Engineering ASCE (2002);128(1): 105-114

-
- [6] Lien K.H., Chiou Y.J., Wang R.Z., Hsiao P.A., *Vector Form Intrinsic Finite Element analysis of nonlinear behavior of steel structures exposed to fire*, Engineering Structures (2010); 32: 80-92
- [7] Franssen J.-M., *SAFIR: A Thermal/Structural Program for Modeling Structures Under Fire*, Engineering Journal (2005); 42(3): 143-150
- [8] Najjar S.R., Burgess I.W., *A nonlinear analysis for three dimensional steel frames in fire conditions*, Engineering Structures (1996); 18: 77-89
- [9] Bailey C.G., *Development of computer software to simulate the structure behaviour of steel-framed buildings in fire*, Computers and Structures (1998); 67: 421-438
- [10] Izzudin B.A., *ADAPTIC User Manual – Revision 1.4e*, Department of Civil and Environmental Engineering Imperial College London, 2012
- [11] ABAQUS Version 6.14, *Finite element analysis software*, Dassault Systèmes, 2014
- [12] ANSYS Version 17.0, *Finite element analysis software*, ANSYS, Inc., 2016
- [13] DIANA Version 10.1, *Finite element analysis software*, DIANA FEA BV, 2016
- [14] European Committee for Standardisation, *Eurocode 3 Design of steel structures - Part 1-1. General rules and rules for buildings*
- [15] European Committee for Standardisation, *Eurocode 3 Design of steel structures - Part 1-2. General rules Structural fire design*
- [16] Petryk H., Thermann K., *On discretized plasticity problems with bifurcation*, International Journal of Solids Structures (1992); 29(6): 745-765
- [17] Battini J.M., *Co-rotational beam elements in instability problems*, PhD thesis (2002), Department of Structural Engineering KTH, Stockholm, Sweden
- [18] Crisfield M.A., *Non-linear Finite Element Analysis of Solids and Structures, Volume 1: Essentials*, Wiley, Chichester, England
- [19] Tondini N., Morbioli A., Vassart O., Lechéne S., Franssen J.-M., *An integrated modelling strategy between a CFD and an FE software: methodology and application*, Journal of Structural Fire Engineering (2016), 7(3)
- [20] Rubert A., Schaumann P., *Structural Steel and Plane Frame Assemblies under Fire Actions*, Fire Safety Journal (1986); 10: 173-184
- [21] Franssen J.M., *The Unloading of Building Materials Submitted to Fire*, Fire Safety Journal (1990): 213-227
- [22] Franssen J.M., *Contributions a la modelisation des incendies et de leurs effets sur les batiments*, Chercheur Qualifié du F.N.R.S, Université de Liege, Faculté des Sciences Appliquées
- [23] Cardona A., Huespe A., *Evaluation of simple bifurcation points and post-critical path in large finite rotation problems*, Computer Methods in Applied Mechanics and Engineering (1999); 175: 137-156

-
- [24] Battini J-M., Pacoste C., *Plastic instability of beam structures using corotational elements*, Computer Methods in Applied Mechanics and Engineering (2002); 191: 5811-5831.
- [25] Fletcher R., *Practical Methods of Optimization*, Wiley (1987), second edition.
- [26] Jiang J., Usmani A., *Modeling of steel frame structures in fire using OpenSees*, Computer and Structures (2013); 118: 90-99
- [27] Ali H.M., Senseny P.E., Alpert R.L., *Lateral displacement and collapse of single-story steel frames in uncontrolled fires*, Engineering Structures (2004); 26: 593-607
- [28] Sun R., Huang Z., Burgess I.W., *Progressive collapse analysis of steel structures under fire conditions*, Engineering Structures (2012); 34: 400-413
- [29] Khorasani N.E., Garlock M.E.M., Quiel E., *Modeling steel structures in OpenSees: Enhancements for fire and multi-hazard probabilistic analyses*, Computer and Structures (2015); 157: 218-231
- [30] Izzudin B.A., Song L., Elnashai A.S., Dowling P.J., *An integrated adaptive environment for fire and explosion analysis of steel frames – Part II: verification and application*, Journal of Constructional Steel Research (2000); 53(1): 87-111
- [31] Franssen J-M., Schleich J-B, Cajot L-G., *A simple model for the Fire Resistance of Axially-loaded Members according to Eurocode 3*, Journal of Constructional Steel Research (1995), 53: 49-69

Conclusions

The aim of this thesis was to analyse and develop problems concerning the use of finite elements for the analysis of issues characterised by high plasticity, geometrical and material nonlinearity, large displacements and rotations; all combined with the effect of temperature on the material mechanical properties. Three different topics were introduced. Each of them numerically investigated the behavior of steel (or steel-concrete) structures that were analysed at ambient temperature (Topic 1) and then studied under the effects of temperature (Topic 2). The knowledge gained in the first two Topics, was then exploited to develop a thermomechanical finite element for the analysis of steel structures at ambient and elevated temperature (Topic 3). In particular, branch-switching analyses were implemented to study instability problems without the need including geometrical imperfections.

A summary of the results obtained for each Topic is herein reported.

-Numerical analysis of cold formed steel profiles subjected to monotonic bending moment (Topic 1)

An experimental-numerical study on cold-formed laterally-restrained steel rectangular hollow flanges beams was performed in order to investigate the flexural capacity of innovative (for cross-section design) steel elements. A numerical model was derived by introducing the real measured dimension of the beam specimens and the material properties obtained by a campaign of tensile tests extracted from different section regions. The latter includes the flexural residual stresses. Based on the material properties and test typology (monotonic) an identification of constitutive law, hardening law and yield surface was performed to correctly capture the development of the plasticity. This is fundamental in order to model the local buckling phenomena that affects the compressed parts of the cross section. This profiles are in fact thin-walled cross section profiles that lie in Eurocode Class 4. Local geometrical imperfections were introduced based on the lowest local buckling mode shape. Several numerical tests performed with different values of local imperfections amplitude demonstrated a sensitivity of the model mainly in terms of variation of the ultimate load, with a reduction of ultimate load that that is generally connected to an increase in imperfection amplitude. Calibration of the numerical model provided good agreement with experimental tests in terms of ultimate bending moment, ultimate displacement, mode of failure.

The initial elastic stiffness was well reproduced in RHFB-300 beams where as the FE

was not capable of detecting some minor plasticization occurred early in the RHFB-240 specimen tests owing to local imperfections and local effects. Parametric analyses performed on the numerical calibrated model, showed that both EN1993 and DSM tend to be conservative in predicting the section bending capacity of steel beam profiles. Nevertheless, the exploitation of such profiles can be attractive for structural applications as secondary beams in small framed houses because of favourable flexural performance/weight ratio.

-Coupling methodology between a CFD and an FE software for the study of structures at high temperatures (Topic 2)

This work introduced the effects of elevated temperatures, high geometrical nonlinearities and large displacements by means of a numerical study performed on a steel-concrete open car park subjected to localized fires of burning vehicles. The work focused in an integrated modelling strategy between a CFD software and an FE software that has been recently applied to FDS and SAFIR. Although it implies some simplifications, the proposed weak coupling approach is more desirable for practical applications with respect to a full coupling approach because it can cover a wide number of likely-to-occur scenarios in compartment fires by being at the same time less computational demanding and handier to use. The potential benefit of the integrated methodology was shown when applied to a steel-concrete composite open car park and then compared with the simplified Hasemi model. In fact, the fire performance analysis of the open car park highlighted that the FDS–SAFIR methodology allows overcoming shortcomings of simplified models by performing the thermal analysis in the structural elements based on more advanced modelling of the fire development, provided that a careful assessment of all assumptions can be performed. Conversely, the Hasemi model revealed to be more conservative in terms of thermal action.

-Development of a co-rotational beam element for the study of steel structures subjected to fire loadings (Topic 3)

This work finally exploits the expertise obtained in the previous works, described in Topic 1 and Topic 2, by developing a co-rotational two-dimensional beam element to study the behaviour of steel structures exposed to fire and in particular instability problems in the elastic-plastic range. Different local formulations were implemented (Local linear Bernoulli, Local Shallow Arch Bernoulli and Local Linear Timoshenko). Each of them allows to introduce a finite element with particular potentialities (introduction of shear effects, reduction of the number of finite elements etc.). Validation against experimental data and numerical simulations made with commercial software likes ABAQUS and SAFIR, was performed and showed good agreement. Moreover, an improved displacement predictor based on the linear combination of the two previous converged solutions was tested. It allowed faster convergence by

significantly reducing the computational time required for analysis.

Branch-switching procedures capable of analysing instability problems in elastic-plasticity of steel structures by detecting bifurcation points of secondary equilibrium paths without explicitly including initial geometrical imperfections were successfully implemented. This entails a significant benefit in terms of practical implications in the context of structural fire FE modelling. First, since there is no need to explicitly introduce the geometrical imperfections to detect critical points, the geometry of the structural model is less complex. No assumptions on the amplitude of the imperfections have to be made. Then, critical bifurcation points that depend on the actual distribution of mechanical loads and temperatures in the elements at each converged solution can be identified. This entails a major advantage for the analysis of steel structures in fire for which, in general, the buckling mode shapes vary with time and consequently any introduced imperfections based on buckling analysis at ambient temperature may not be representative of the actual behaviour at elevated temperature. Furthermore, the proposed FE element was able to reproduce the flexural buckling curve of EN1993-1-2 for H steel compressed elements without including imperfections. This characteristic suggests that the FE can predict the buckling strength of real steel members in compression, which is an important added value for design applications.

Future research

The work presented in this thesis can be extended by widening the capabilities of the finite element presented in Topic 3. A three dimensional formulation can be introduced based on co-rotational kinematic approach. The 3D beam model should introduce thermal effects and branch-switching procedure in order to take into account torsional and flexural-torsional instabilities for compressed members or lateral torsional buckling for beams that are subjected to high temperatures. An equivalent procedure could be employed in the development of a shell element with thermomechanical capabilities.

This thesis work aims to successively analyze and develop "ex novo" problems concerning the use of finite elements for the analysis of issues characterized by high plasticity, geometrical and material nonlinearity, large displacements and rotations; all combined with the effect of temperature on the material mechanical properties. The ultimate objective of the work is the analysis and development of nonlinear Finite Elements devoted to the modelling of steel structures at ambient and elevated temperature.

Three different experiences will be analyzed in this elaborate; each of them characterized by specific issues that may be involved in the analysis via finite element method of steel structures at ambient and elevated temperature. At the same time innovative aspects that are related, for example, to the particular typology of the analyzed case study (first case) or in the methodology used in the treatment of the problem (second and third case) are investigated. The thesis structure chronologically retraces this path and the results and the experience gained from each of them were exploited to ultimately implement a thermomechanical finite element that is expression of all the tackled problems. The thesis consists of a collection of three papers that have published or submitted on each of the investigated topics.

Andrea Morbioli is a doctoral student in civil, environmental and mechanical engineering at the University of Trento, Italy. His research is mainly focused on the risk analysis of steel structures subjected to exceptional fire loadings, with particular attention to fire safety engineering. He spent part of his doctoral research on the development of thermomechanical finite elements for the study of instability problems of structures involved in fire.